

# POLITECNICO DI TORINO

DEPARTMENT OF CONTROL AND COMPUTER ENGINEERING

Master degree course in Mechatronic Engineering

Master Degree Thesis

## **Modeling and simulation of the electro-thermal behavior of a Lithium-ions battery with concurrent electrical and mechanical load**



Supervisor  
Prof.ssa Silvia Bodoardo

Company Supervisor  
Dott. Mag. Luigi Aiello

Candidate  
Claudio Lerario  
ID Number: 267203

Academic Year 2020/2021



# *Table of contents*

1. Literature review on Lithium-ion batteries and modelling strategies .....	1
1.1 Working principle of a lithium-ion cell .....	1
1.1.1 Electrical parameters of a Lithium-ion cell.....	2
1.1.2 Internal resistance of a battery: a physical perspective.....	3
1.1.3 Battery internal impedance .....	5
1.2 Batteries form factors .....	7
1.3 Effects of external mechanical loading on Lithium-Ion cells.....	8
1.3.1 Separator pores closure: effects on cell capacity .....	8
1.3.2 Separator pores closure: effects on internal impedance.....	10
1.3.3 Estimation of charge transfer resistance for a deformed separator.....	12
1.3.4 Soft short circuit and separator piercing .....	13
1.4 Modelling strategies for Lithium-ion batteries .....	15
1.4.1 Empirical models .....	17
1.4.2 Multiphysics models .....	18
1.4.3 Electrochemical models .....	19
2. From the experimental investigation to the modelling strategy .....	22
2.1 The cell under test.....	22
2.2 Test setup and methodology .....	24
2.3 Loading conditions and results from experimental investigation.....	26
2.4 Modelling strategy to reproduce test conditions.....	28
2.5 State of art of 1D circuit model .....	29
2.5.1 Lumped parameters evaluation .....	30
2.5.2 1D simulation of 20-30% SoC electrical cycling.....	33
3. Model set-up with deformed geometry .....	35
3.1 STAR CCM+ environment for Finite Element Method analysis .....	35

3.2 Workflow of model realization.....	35
3.3 Deformed geometry realization and import.....	36
3.4 Regions and interface definition.....	43
3.5 Physics continua definition.....	45
3.6 User field function definition for equivalent circuit modelling.....	48
3.7 Encountered divergence problem during simulation.....	52
3.7.1 Strategy for the identification of the cause of the divergence.....	55
3.7.2 Local imbalance of model variables at divergence and corrections .....	55
3.7.2 Simplification of solving conditions .....	58
3.7.3 Realization of alternative deformed geometries .....	60
4. Analysis of test data and simulation.....	63
4.1 Analysis of results from experimental investigation .....	63
4.2 Simulation of electrical cycling .....	66
4.2.1 1C rate simulation matching experimental data.....	67
4.2.2 Global internal resistance variation.....	68
4.2.3 Local internal resistance variation .....	69
4.2.4 Simulation results for different C-rates.....	74
4.2.5 Effects of local resistance variation .....	75
4.3 Temperature results .....	78
5. Conclusions .....	79
6. References .....	81

## ***List of Figures***

Figure 1.1 - Charging/discharging process [5].....	2
Figure 1.2 - OCV VS SoC curve [web].....	3
Figure 1.3 - Battery circuit with internal resistance [6] .....	4
Figure 1.4 - Randle's internal impedance equivalent circuit [7].....	5
Figure 1.5 - Impedance contributions [7].....	6
Figure 1.6 - EDL schematic representation [web] .....	6
Figure 1.7 - Prismatic and cylindrical cell structure [web] .....	7
Figure 1.8 - Pouch cell internal arrangement and picture .....	8
Figure 1.9 - Separator pores before and after compression [9] .....	9
Figure 1.10 - Effects of compressive loads on discharged capacity [9].....	10
Figure 1.11 - EIS impedance plots in different compressive loads conditions [10] .....	11
Figure 1.12 - Schematic representation of porous separator compression [12] .....	12
Figure 1.13 - Irregularity of electrodes surfaces [web] .....	13
Figure 1.14 - Short circuit voltage curve (a), with detail of soft short circuit (b) [13] .....	14
Figure 1.15 - Modelling phases map [11] .....	15
Figure 1.16 - Modelling strategies for Lithium-ion batteries [13] .....	16
Figure 1.17 - Example of RC-R 1D equivalent circuit.....	17
Figure 1.18 - Temperature scene from a FEM simulation on cylindrical cell [16].....	18
Figure 1.19 - Modelling phases for a mechanical-electro-thermal model [17].....	19
Figure 1.20 - P2D model schematic structure [14].....	20
Figure 2.1 - Pouch cell employed in tests .....	22
Figure 2.2 - Cell internal layer arrangement [19].....	23
Figure 2.3 - Impactor design .....	24
Figure 2.4 - Test bench set up with lower insulating layer .....	24
Figure 2.5 – Complete test bench set up .....	25
Figure 2.6 - Cell after mechanical deformation.....	26
Figure 2.7 - Cycling 1C 20-30% pristine Vs deformed cell voltage curves .....	27
Figure 2.8 - Cycling 2C 20-30% pristine Vs deformed cell voltage curves .....	27

Figure 2.9 - Cycling 3C 20-30% pristine Vs deformed cell voltage curves .....	28
Figure 2.10 - Modelling strategy chart.....	29
Figure 2.11 - Weilin Luo's equivalent circuit model.....	29
Figure 2.12 - OCV curve with respect to discharged capacity.....	30
Figure 2.13 - Ohmic resistance evaluation.....	31
Figure 2.14 - Interval resistance VS discharged capacity curve .....	31
Figure 2.15 - Python cycle defining current profile for electrical cycling .....	33
Figure 2.16 - Electrical cycling curves and relationship with OCV curve.....	34
Figure 3.1 - Example of .inp file .....	36
Figure 3.2 - Impactor technical representation.....	36
Figure 3.3 - Non-smooth transition profile.....	37
Figure 3.4 - Gaussian function .....	37
Figure 3.5 - Mismatch between semicircular profile and Gaussian profile .....	38
Figure 3.6 - Definition of a set of points on circular profile .....	38
Figure 3.7 - Code for definition of sigma variation law.....	39
Figure 3.8 - Polynomial sigma function plot.....	39
Figure 3.9 - Fitting between obtained profile and impactor profile .....	39
Figure 3.10 - Vector mapping for deformed and pristine nodes positions.....	40
Figure 3.11 - Python code for nodes displacement application.....	41
Figure 3.12 - Identification criterion for nodes in deformed area .....	42
Figure 3.13 - Section view of the obtained deformation.....	42
Figure 3.14 - Deformed geometry and deformation area detailed view.....	43
Figure 3.15 - Interfaces between regions detail .....	44
Figure 3.16 - Interfaces between tabs layers .....	44
Figure 3.17 - StarCCM+ interface panel for models selection.....	45
Figure 3.18 - Correspondence between layer arrangement and equivalent circuit .....	48
Figure 3.19 - OCV-VS-SoC interpolation function in StarCCM+.....	49
Figure 3.20 - Polarization resistance curve during discharge (a) with transient detail (b). 51	
Figure 3.21 - $R_{int}$ -VS-SoC interpolation function in StarCCM+.....	51
Figure 3.22 - Pristine mesh initial conditions for discharge process.....	52

Figure 3.23 - Residual plot in convergence conditions .....	53
Figure 3.24 - Deformed mesh initial conditions for discharge process.....	53
Figure 3.25 - Residuals plots in divergence conditions.....	54
Figure 3.26 - Strategy for the identification of divergence cause .....	55
Figure 3.27 - SoC local imbalance in deformed area .....	56
Figure 3.28 - ECD local imbalance in deformed area .....	56
Figure 3.29 - Sigma function correction graph .....	57
Figure 3.30 - Section view of deformed geometry with rigid nodes displacement.....	60
Figure 3.31 - Skewness angle representation.....	61
Figure 3.32 - Section view of deformed geometry with 0.5mm strain allocation.....	62
Figure 4.1 - Detail of 1C cycling 20-30% for V <sub>pp</sub> evaluation.....	63
Figure 4.2 - Detail of 2C cycling 20-30% for V <sub>pp</sub> evaluation.....	65
Figure 4.3 - Detail of 3C cycling 20-30% for V <sub>pp</sub> evaluation.....	65
Figure 4.4 - Electrical cycling simulation strategy.....	66
Figure 4.5 - Comparison between 1C pristine simulated and real measurement voltage curves.....	67
Figure 4.6 - Internal resistance curve with offset application during cycling.....	68
Figure 4.7 - Comparison between 1C simulated cycling in pristine and global resistance modification condition .....	69
Figure 4.8 - Correspondence between single element and equivalent circuit .....	70
Figure 4.9 - Cell subdivision between deformed and pristine areas.....	70
Figure 4.10 - Electrical conductivity local definition scene.....	72
Figure 4.11 - Electrical conductivity function plot during cycling .....	73
Figure 4.12 - Comparison between 1C simulated cycling in pristine and local resistance modification condition .....	73
Figure 4.13 - Comparison between 2C simulated cycling in pristine and local resistance modification condition .....	74
Figure 4.14 - Comparison between 3C simulated cycling in pristine and local resistance modification condition .....	75
Figure 4.15 - ECD distribution for pristine condition simulation .....	75

Figure 4.16 - ECD distribution for impacted condition simulation .....	76
Figure 4.17 - ECD integral comparison non-deformed area (1C-rate) .....	76
Figure 4.18 - SoC scene during electrical cycling (1C) .....	77
Figure 4.19 - Temperature scene during electrical cycling (1C).....	78

## ***List of Tables***

Table 1- Layer thicknesses [19] .....	23
Table 2 - Testing conditions table .....	26
Table 3 - Stress-strain evaluation for layer thicknesses .....	40
Table 4 - Materials physical properties .....	47
Table 5 - Model simplification simulation part 1 .....	58
Table 6 - Model simplification simulation part 2.....	59
Table 7 - Experimental data voltage variation .....	66



## *Abstract*

Electric mobility represents one of the most challenging themes of modern-days. The possibility of a detachment from the dependance on fossil fuels, could represent a strong tool to fight the always increasing global warming trend due to CO<sub>2</sub> emissions. The main obstacles to a wide spread of EVs are surely represented by the constant comparisons with their equivalent traditional vehicles in terms of performances, autonomy and safety. Regarding safety, many researches has been conducted in the last years, in order to highlight the critical elements of battery systems that could lead to dangerous situations. Many studies have been conducted on thermal runaway conditions, so, in severe mechanical loading on battery cells, but really few researches tried to understand the effects of a non-disruptive mechanical load on a cell.

This work of thesis, developed at Vehicle Safety Institute of Graz, takes part to the project Safe Batteries. The main target of the study is the evaluation of the electro-thermal effects of a mechanical non-disruptive indentation on a cell leading to a permanent deformation. Starting from an experimental investigation, in which the same loading conditions were applied to a pristine and a deformed cell, it was possible to compare the output results, in order to evaluate the effects on internal impedance caused by the application of an impactor. On these basis, a FEM model was set up in order to perform simulations able to describe the local imbalance of internal parameters created by the inducted deformation.



## ***Introduction***

One of the most important long-term objectives of the modern society is the achievement of a competitive low carbon economy. This mission is mainly based on enabling environmentally sustainable investments, particularly in terms of decreasing energy consumption in buildings, transition to electric vehicles, and developing smart electricity networks, while promoting renewable energy use in order to reduce greenhouse gas emissions by at least 80% by 2050 compared to 1990 levels [1]. Since, transport is one of the main sector responsible for CO<sub>2</sub> emissions, diffusion of Electric Vehicles (EVs) could allow immense reduction. Considering the European Union territory, road vehicle transport constitutes 30% of total emissions [2]. These impressive data arouse the necessity of a turnaround in the approach to the concept of mobility. The current strong dependence on fossil fuels is one of the most important issues when talking about future mobility. Electricity as an energy vector for vehicle propulsion offers the possibility to substitute oil with a wide diversity of primary energy sources [3]. This could ensure security of energy supply and a broad use of renewable and carbon-free energy sources. The shifting to a complete electric mobility opened a wide research on energy storage systems.

Lithium-ion batteries actually represent the most employed storage devices in EVs. These are able to provide one of the best energy-to-weight ratios, exhibit no memory effect, and experience low self-discharge when not in use. These beneficial properties, as well as decreasing costs, definitely define Li-ion batteries as the leading candidate for the next generation of automotive vehicles. [4]. Scientific research on Li-ion batteries focused on two main aspects in the last years: performance optimization and safety. Both areas of study require tools for the evaluation and analysis of the design parameters of a cell. For this reason, experimental investigations and tests are conducted on a wide range of regular working and abuse conditions, in order to better understand the aspects to be optimized and the risks associated to a certain load conditions. A trial-and-error determination of battery design parameters and operating conditions is inefficient, which has motivated the use of battery models to numerically optimize battery designs [4]. This work of thesis takes part to the “SafeBattery” project, funded by VSI and industrial partners (AVL, Audi, Bosch, Daimler, Kreisler, Porsche, SFL), with the main objective of understanding which are the hazards of Li-ion batteries under various mechanical load conditions.

In particular, the treated case of study regarded the evaluation of the electro-thermal effects of a non-disruptive deformation on a pouch cell, in other words the battery is subjected to a mechanical indentation through the application of an impactor, then different electrical loads are applied to evaluate the differences between the behavior of the pristine battery and the deformed one. This experimental investigation represents the basis of this work of thesis, in which a modelling strategy was defined in order to reproduce and simulate the testing condition with the target of the identification of local variation of internal parameters of the cell.

In the first chapter, a literature review was conducted on two main arguments. The first part starts from the basic working principle of a Lithium-ion cell and continues with a research on the effects of mechanical loading on the internal parameters, while the second part provides an overview of modelling approaches for batteries, from the simplest ones like 1D equivalent circuits, to the more complex electrochemical models.

First part of chapter two presents the setup and results of the experimental investigations, then, in the second part, the modelling strategy is defined and a previously realized 1D model is employed to obtain a preliminary simulation of voltage curve for the same loading conditions of real tests.

In chapter three the steps for the realization of a FEM model are presented, starting from the definition of a deformed mesh geometry for simulation. Due to the impossibility of conducting a mechanical simulation, the geometry was obtained through a mathematical manipulation of the nodes of a regular mesh. Simulations conducted with this geometry encountered divergence problems during simulations, that have been widely investigated and reported in the last part of the chapter. For this reason, the next steps have been conducted acting local modifications of internal parameters on a regular mesh geometry. Fourth chapter provides an analysis of the results coming from tests, and the implementation of a local internal resistance variation in the model on the basis of observed electrical behaviors. Output curves coming from simulation are compared with real data, and, in chapter five, conclusions and final consideration are exposed.

# ***CHAPTER 1***

## ***1. Literature review on Lithium-ion batteries and modelling strategies***

### ***1.1 Working principle of a lithium-ion cell***

Batteries are subdivided in two main categories: primary and secondary batteries. Primary batteries cannot be recharged because of the irreversibility of the chemical reaction that takes place, so, once used must be discharged. Secondary batteries, instead can be recharged and used multiple times exploiting the reversibility of the reaction; Li-Ion batteries belong to this category.

In this kind of battery system, the aim is to generate electrical energy by converting chemical energy via redox reactions at the electrodes. In particular Li-ion cells employ lithium intercalation between the positive and the negative electrodes i.e. as a battery is charged and discharged the lithium ions move back and forth between the cathode and the anode; because of this they are named as “Rocking-chair” batteries.

The cell structure is composed of a defined set of layers: the two electrodes and the separator. Each electrode is constituted by two layers of active material with a current collector in the middle of them.

- Negative electrode active material: usually made of a carbonaceous material, like graphite. Its structure results very suitable for Li-ions allocation.
- Positive electrode active material: generally, a metal oxide with a much more complex composition with respect to the negative electrode.
- Current collectors: electronic conductors that take no part in the chemical reaction, used to drive current when charging or discharging the battery.
- Separator: permeable membrane that physically isolates the positive and negative electrodes. It is an ionic conductor but an electronic insulator. Its function is to prevent internal short circuiting between the two electrodes, which would cause the cell to rapidly self-discharge and become useless.
- Electrolyte: a ionic conductor that provides the medium for internal ionic charge transfer

between the electrodes. The electrolyte most often comprises a liquid solvent containing dissolved chemicals (the solute) that provide this ionic conductivity [5].

During the charging process electrons migrate from the positive electrode material to the negative one through an external conductor. The global neutrality of the charge is granted by the consequent Li-ions de-intercalation from the positive electrode through the electrolyte into the negative electrode. When the battery is discharging electrons move from the negative to the positive electrode, and for the same principle Li-ions move back to the positive electrode with an intercalation process as showed in Figure (1.1).

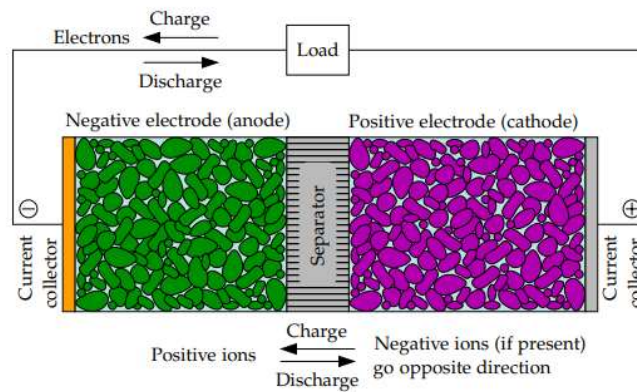
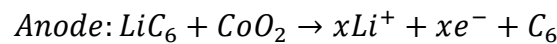
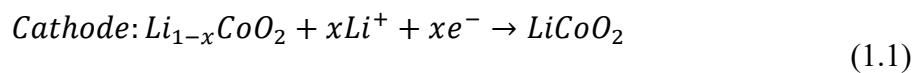


Figure 1.1 - Charging/discharging process [5]

Considering the discharging phenomenon, it is possible to associate the positive electrode to the cathode and the negative electrode to the anode, observing the following REDOX reaction.



### 1.1.1 Electrical parameters of a Lithium-ion cell

Considering a generic Lithium-ion cell, it is possible to identify a set of parameters in order to describe the main characteristic of the cell itself.

- Cell capacity: nominal charge capacity specifies the quantity of charge, in ampere-hours (Ah) or milliampere-hours (mAh), that a cell is rated to hold. [5]
- Cut-off voltage: voltage at which a battery is considered fully discharged, beyond which further discharge could cause harm. [5]
- C-rate: is a measure of the rate at which a battery is being charged or discharged. It is defined as the current through the battery divided by the theoretical current draw under

which the battery would deliver its nominal rated capacity in one hour.

For example, considering a battery with normal capacity of 40 Ah, a discharge rate of 2C corresponds to a current value of 80 A that would completely discharge the cell in half an hour.

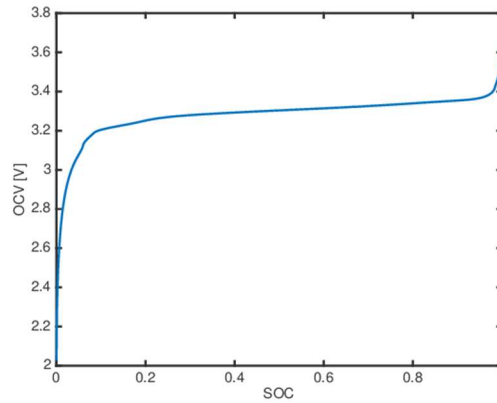


*Figure 1.2 - OCV VS SoC curve [web]*

- Open circuit voltage (OCV): voltage value measured between the battery tabs in absence of current. This value is SoC dependent, with a non-linear relationship between the two parameters. Experimentally, this curve can be evaluated applying a very low charging/discharging current ( $C/40$ ). The purpose of the slow rate is to minimize the excitation of the dynamic parts of the cell model, granting a condition really close to the equilibrium state [5].

The curve in Figure (1.2) shows the trend of the measured voltage with respect to the State of Charge, with the maximum and minimum values of voltage just equal to the cut-off voltages.

### ***1.1.2 Internal resistance of a battery: a physical perspective***

The standard representation of a battery comprises a source of electromotive force in series with an internal resistance [6]. The battery has a tendency to maintain electric potential difference across its terminals equal to its chemical potential, and in an open circuit, when no current flows, this voltage is the just explained OCV. However, in a closed circuit, a drop in electric potential across the battery terminals is inevitable for a steady flow of electric current throughout the circuit, because the chemical reactions driving the electric current within the battery can proceed only if the electric potential at its terminals differs from the chemical potential [6].

It is shown that for small voltage changes, the current passing through the battery is linearly

proportional to the change in potential from the open-circuit value giving rise to a semblance of an internal resistance in series with the external resistance. It follows that a battery has to have an internal resistance in order to function as a power source [6].

Naming  $\varepsilon$ , the chemical potential, which is the line integral of the force per unit charge due to chemical reactions (from the negative electrode to the positive electrode), the force generated on a charge by this value of potential can be written as:

$$F_C = e * \frac{\varepsilon}{d} \quad (1.2)$$

Where  $e$  is the value of the charge and  $d$  is the distance between the electrodes.

Considering a simple circuit in which the terminals of a battery are connected with a well-known load resistance  $R_e$  (Figure 1.3), this connection determines a perturbation in the value of the electrochemical potential, determining a force applied on the charge:

$$F_E = e * \frac{-V}{d} \quad (1.3)$$

The net force applied on a charge results:

$$F = e * \frac{\varepsilon - V}{d} \quad (1.4)$$

In this closed circuit the electric current flowing within the battery is due to the chemical reactions, which will take place only if the voltage across the battery  $V$  is different from the chemical potential  $\varepsilon$ . From this assumption the value of internal resistance can be written as:

$$R_i = \frac{\varepsilon - V}{I} \quad (1.5)$$

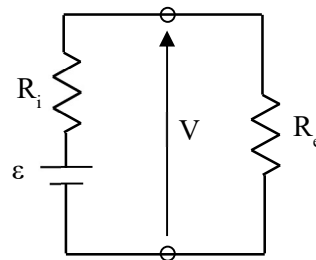


*Figure 1.3 - Battery circuit with internal resistance [6]*

The actual value of the internal resistance of a cell may depend upon a combination of various factors. If the effective cross-section areas of the electrodes are large, more current may flow through the battery even for the same  $\varepsilon$ - $V$  change, implying a lower  $R_i$  value. Similarly, a larger separation between the electrodes (higher  $d$ ) would imply a smaller push

on the charges even for the same  $\varepsilon$ -V change, resulting in a smaller current and implying a higher  $R_i$  value. The nature of the constituents (electrodes and the electrolyte) of a battery also matter as a better conducting electrolyte means a higher current for the same  $\varepsilon$ -V and thereby a smaller internal resistance [6].

### 1.1.3 Battery internal impedance

On the basis of the just explained analysis of the internal resistance of the battery, this internal parameter can be furtherly extended to a more precise set of impedance contributions able to reproduce and model the electrochemical phenomena inside the cell. Referring to Randles' model for impedance evaluation [7], this can be represented through three main contributions: ohmic resistance, activation polarization and concentration polarization. In terms of equivalent circuit, Figure (1.4) shows how these different efforts can be modeled.

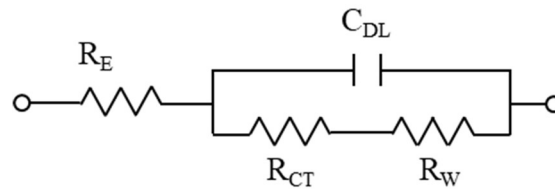


*Figure 1.4 - Randle's internal impedance equivalent circuit [7]*

- **$R_E$** : ohmic resistance of the cell, consists of the electrode, the electrolyte and the separator's physical resistances inside the battery.  $R_E$  has an initial value in the beginning of the discharge. Furthermore, we postulate that as discharge progresses the heat generated by the reactions and the current flow causes the internal temperature to go up, effectively increasing the resistivity of the electrode material, thus increasing this contribution as observable in Figure (1.5).
- **$R_{CT}$** : charge transfer resistance of the cell; it represents the characteristics of the charge transfer process, describes the status of the activation polarization. In the early and middle stage of the discharge cycle, the cell reactants are enough and the electrochemical reactions take place normally, so,  $R_{CT}$  maintains a small value. In the late stage of the discharge cycle, the reactions cause the cell reactants to be used up rapidly near the end of the discharge resulting in a sharp increase in  $R_{CT}$  as observable in Figure (1.5).
- **$R_W$** : concentration polarization resistance of the cell, also called Warburg impedance. This contribution represents the characteristics of the diffusion process. In the early stage of the discharge cycle, lithium ions are eager to be extracted from the negative electrode.

Therefore,  $R_w$  is small in the early stage of the discharge cycle and increases gradually until the diffusion process reaches a certain balance as observable in Figure (1.5).

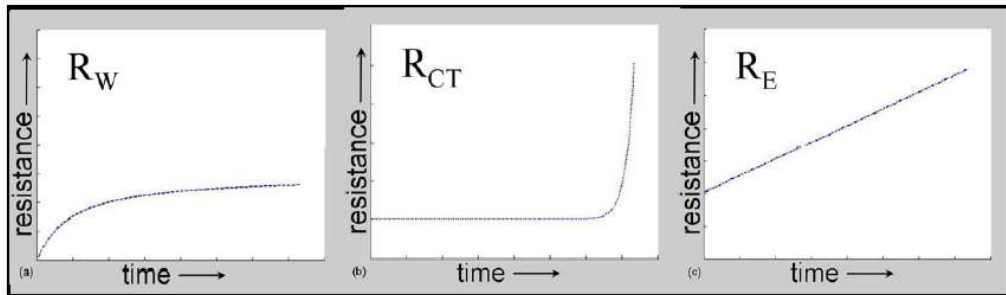


Figure 1.5 - Impedance contributions [7]

-  $C_{DL}$ : double layer capacitance formed due to battery's internal structure.

This capacitive contribution models the electrical double layer phenomenon (EDL). The existence of a potential difference between two different conducting phases is the cause of the formation of this double layer configuration at the phase boundary [8]. Two parallel charges with opposite signs lay on the contact surfaces between phases, determining a capacitive effect (Figure (1.6)).

The first layer, for example considering the anode electrode surface, could be considered as a positive distribution of charges at the beginning of a discharging phase, while the second layer could be formed by free ions attracted from the surface via Coulomb force.

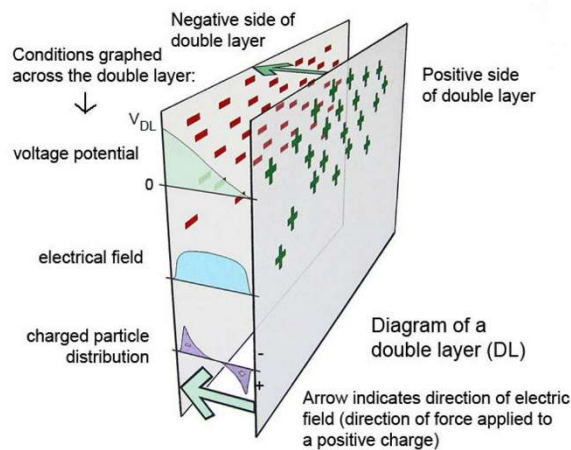


Figure 1.6 - EDL schematic representation [web]

The distance between layers results really small, in the order of molecular distances determining a really high contribution in terms of capacitance [8].

## 1.2 Batteries form factors

Depending on the application and the requirements of the system, different kinds of battery cells can be chosen. This differentiation regards essentially the way in which the internal layers of the battery are arranged and packed, although the electrodes structure remains the same.

The three main configurations are:

- Cylindrical cells: electrodes and separator are rolled up and packed into a cylinder-shaped metallic can. Their main advantage is mechanical stability. The round shape of the battery distributes the internal pressure from side reactions over the cell circumference almost evenly. This allows the cell to tolerate a higher level of internal pressure without deformation (Figure (1.7)).

- Prismatic cells: the electrodes are either stacked or in the form of a flattened spiral. They are usually designed to have a very thin profile in order to facilitate the realization of compact battery packs. The prismatic can allows not to leave empty spaces in adjacent placements, but determines non uniform internal stress, in particular in proximity of the edges of the housing (Figure (1.7)).

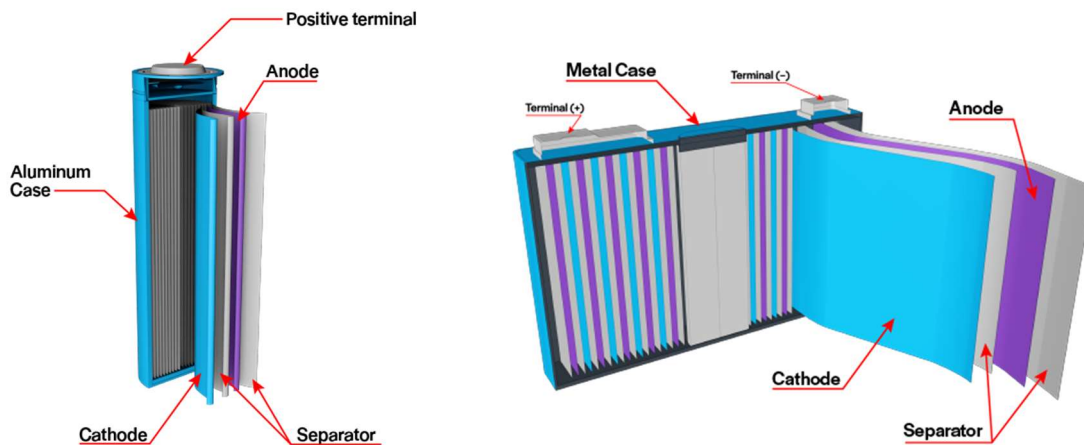
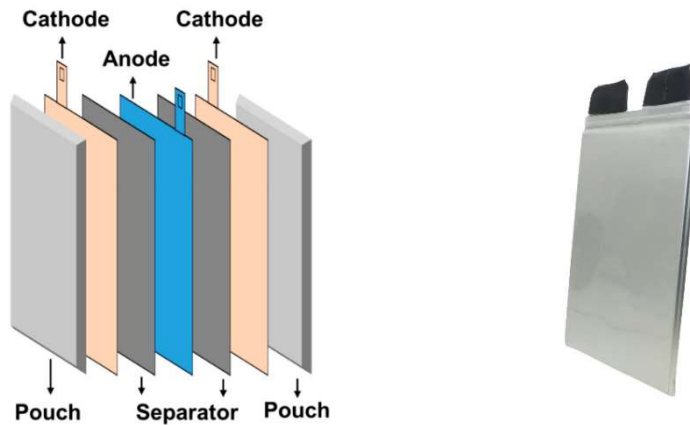


Figure 1.7 - Prismatic and cylindrical cell structure [web]

- Pouch cells: the layers of electrodes are stacked alternatively with the separator sheets obtaining a flat rectangular cell, packed in a thin flexible metal foil. Pouch cells represent the best solution in terms of packaging efficiency due to the low impact of the housing volume. The drawback is the necessity to enclose the set of cells in a rigid structure in order

to avoid damages due to the flexibility of the cells. (Figure (1.8))



*Figure 1.8 - Pouch cell internal arrangement and picture*

### ***1.3 Effects of external mechanical loading on Lithium-Ion cells***

When a battery cell is subjected to a mechanical load, the structural modification inducted in the layers by the deformation could lead to anomalies in the electrochemical processes, for example during electrical cycling. Due to the great differences in the mechanical properties of the materials composing the cell, it is necessary to evaluate which element is majorly affected by the external load and to understand the inducted phenomena.

#### ***1.3.1 Separator pores closure: effects on cell capacity***

Standard polymer separators are composed of polyethylene and polypropylene layers with a yield strength of approximately 10–40 MPa [9], which is significantly lower than the yield strength of the metal current collectors or the ceramic electrode materials. In particular, considering a mechanical load applied to a pouch cell, due to the flexible aluminum-laminate foil pouches, stresses applied externally to the package are accommodated by the battery stack. The strain allocation is so expected to be more severe for the separator layers, that due to their porous nature can lose some of their properties.

Researches reveal that applying a uniform pressure on a pouch cell, the phenomenon of the viscoelastic creep strongly affects the separator layers in terms of porosity [9].

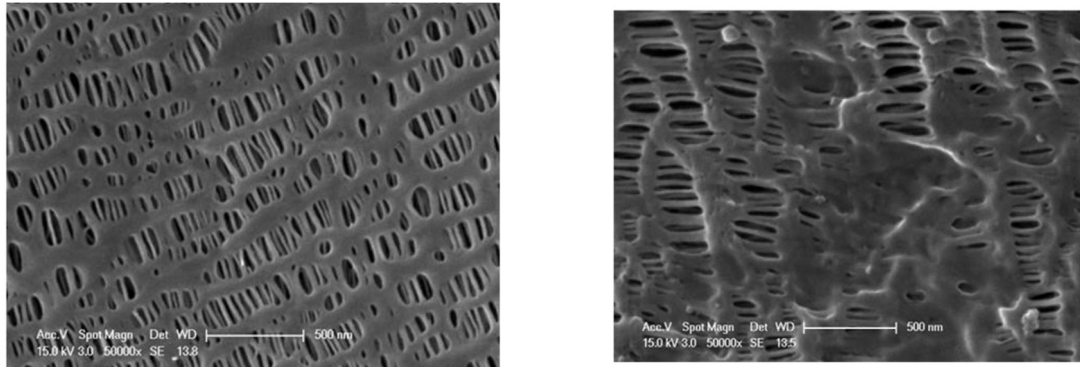


*Figure 1.9 - Separator pores before and after compression [9]*

In absence of applied pressure the structure of the separator is characterized by a large number of slit-like pores on the order of 100 nm in the long dimension and 30–40 nm in the short direction [9]. As the applied stress increases, there is a noticeable decrease in the number of pores as smaller pores close and larger pores shrink. Finally, the 30 MPa separator has a pore area fraction half that of the unstressed sample as showed in Figure (1.9). This decrease in pore volume impedes ion transport and manifests itself as an increase in the internal resistance of the membrane or conversely as a decrease in conductivity.

To further relate the decreases in pore volume and conductivity to battery capacity, the following graph (Figure (1.10)) compares the discharge curves for cells composed of unstressed electrodes with stressed separators. While stressed separators maintain the characteristic cell discharge shape, there is a marked capacity fade and reduction in discharge time as the stress increases. The cell capacity decreases with increasing stress and corresponding total separator strain, with the 30 MPa sample losing more than 70% of its capacity due to the transport limitations [9].

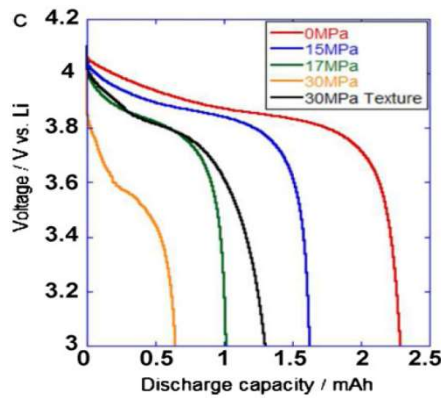


Figure 1.10 - Effects of compressive loads on discharged capacity [9]

The observed capacity losses occur as pore closure decreases the number and size of pathways for ions to shuttle between the electrodes during charging and discharging. This limits the ability of ions to reach reaction sites at a given charge/discharge rate and thus limits the amount of energy that is stored/used.

### 1.3.2 Separator pores closure: effects on internal impedance

The effects of compressive loads on the cell capacity can be related to variations in terms of internal impedance of the cell. A research conducted by Anup Baraia et al. [10] demonstrated that significant effects in the resistive behavior of the battery cell can arise with pressure load applications. In particular, an investigation conducted on pouch cells showed interesting results considering two different load conditions: 5 psi and 15 psi pressures [10].

The graphs in Figure (1.11) represent the result of an Electrochemical Impedance Spectroscopy conducted on the cells. EI is usually measured by applying an AC potential to an electrochemical cell and then measuring the current through the cell. Assume that we apply a sinusoidal potential excitation, the response to this potential is an AC current signal [11]. The amplitude of the excitations is really small, in order to obtain a pseudo-linear response; this concept grants a current response that has the same frequency of the voltage input, but with a phase shifting. The analysis of this phase contribution allows the evaluation of the internal impedance.

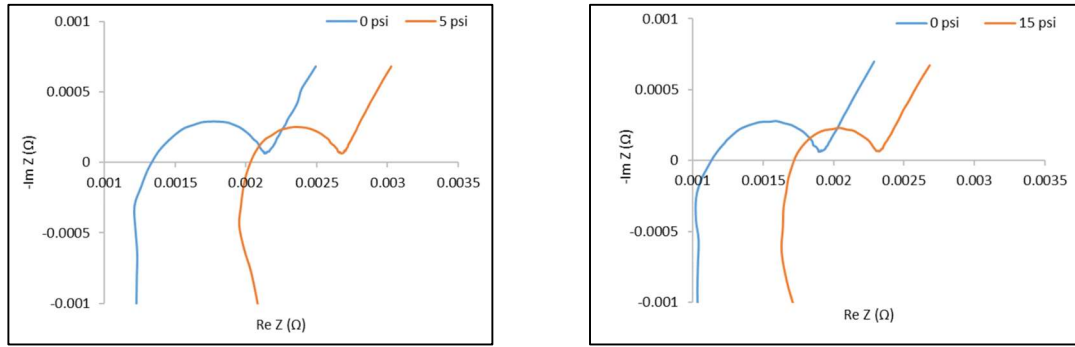


*Figure 1.11 - EIS impedance plots in different compressive loads conditions [10]*

Each curve contains three essential information, characterizing different aspects of the impedance:

- shifting of the curve on the real axis: represents the Ohmic contribution of the impedance;
- amplitude of the semicircular path: contains information about the capacitive behavior of the cell;
- slope of the Warburg tail: defines the solid-state diffusion dynamics.

Considering the two different load conditions, it is evident how the Ohmic contribution increases of a significant value [10], while a more complex behavior can be observed for the capacitive contributions in the restriction of the semicircular interval. On a physical point of view, these variations were justified by two main phenomena. The separator pores closure was identified as the main cause of the charge transfer resistance increase, but in part contrasted by an effect improving the performance of the cell, the electrodes wettability.

Wettability by the electrolyte is claimed to be one of the challenges in the development of high-performance lithium-ion batteries. Non-uniform wetting leads to inhomogeneous distribution of current density and unstable formation of solid electrolyte interface. The pressure application facilitates a uniform distribution of the electrolyte on the surface of the electrodes, leading, also, to an increase of the double layer capacitance [10].

### 1.3.3 Estimation of charge transfer resistance for a deformed separator

In order to interpret the experimentally observed impedance changes associated with separator strain, the resistance of a strained separator, can be modeled by modifying the basic resistance equation to account for separator porosity and tortuosity [12] as shown in Equation (1.6).

$$R = \rho_e \frac{\tau l}{\phi A} \quad (1.6)$$

where R is the resistance associated with ion transport through the separator,  $\rho_e$  is the resistivity of the electrolyte,  $\tau$  is the separator tortuosity, l is the separator thickness,  $\phi$  is the separator porosity and A is the area of the electrodes.

Considering a loading condition as showed in Figure (1.12), it is possible to define a thickness deformation coefficient  $\epsilon$  [10] [12] in Equation (1.7) and a consequent law for the conservation of volume after the deformation in Equation (1.8). In this equation, the porosity coefficient is treated as the fraction of section area of the separator occupied by the pores.

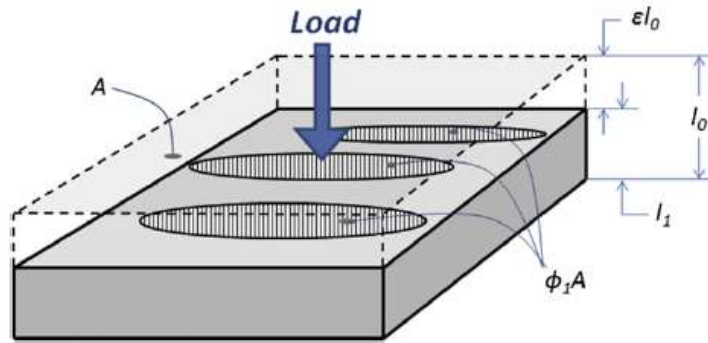


Figure 1.12 - Schematic representation of porous separator compression [12]

$$l_1 = l_0(1 - \epsilon) \quad (1.7)$$

$$V_1 = A(1 - \phi_1)l_1 = V_0 = A(1 - \phi_0)l_0 \quad (1.8)$$

It is easy to derive the porosity of the new configuration with respect to the original one as a function of the deformation function in Equation (1.9). In a similar way the value of the new tortuosity value can be defined in Equation (1.10).

$$\phi_1 = \phi_0 \frac{(1 - \epsilon/\phi_0)}{1 - \epsilon} \quad (1.9)$$

$$\tau = \Phi^{1-\alpha} , \tau_1 = \tau_0 \frac{(1 - \varepsilon/\Phi_0)^{1-\alpha}}{1 - \varepsilon} \quad (1.10)$$

The increase of porosity would determine a reduction of the resistance, while the increase a tortuosity an opposite effect. For this reason, combining Equation (1.8) with the expressions of the tortuosity and porosity variation it is possible to obtain an equation able to estimate the ion transfer resistance variation [12] .

$$\Delta R = R_0 \left( \frac{(1 - \varepsilon)^{\alpha+1}}{\left(1 - \frac{\varepsilon}{\Phi_0}\right)^\alpha} - 1 \right) \quad (1.11)$$

Knowing the initial values of resistance ( $R_0$ ), porosity ( $\phi_0$ ) and the value of the Bruggeman exponent ( $\alpha$ ) the new resistance value is only dependant on the deformation coefficient [12].

### 1.3.4 Soft short circuit and separator piercing

Besides the charge transfer resistive effects due to separator compression, another phenomenon that could occur for high strain of separator layers is the separator piercing. The contact surface between electrodes and separator is usually not smooth, so that, in case of a complete reduction of the effective separator thickness, for example in an indentation test, a friction could be inducted between the two electrodes.

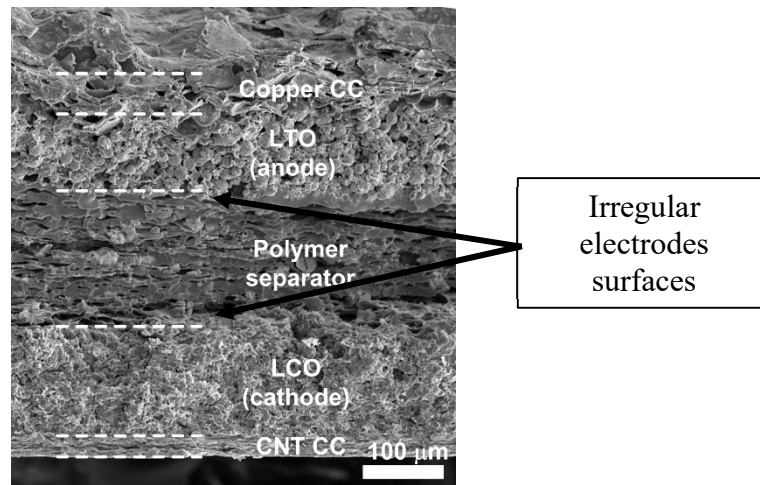


Figure 1.13 - Irregularity of electrodes surfaces [web]

When a sharp edge deforms the separator layer, even not leading to rupture, the extreme thinning leads to the formation of a transparent section that could be crossed by the

extremities of the electrodes. The contact between electrodes would instantly determine an internal short circuit.

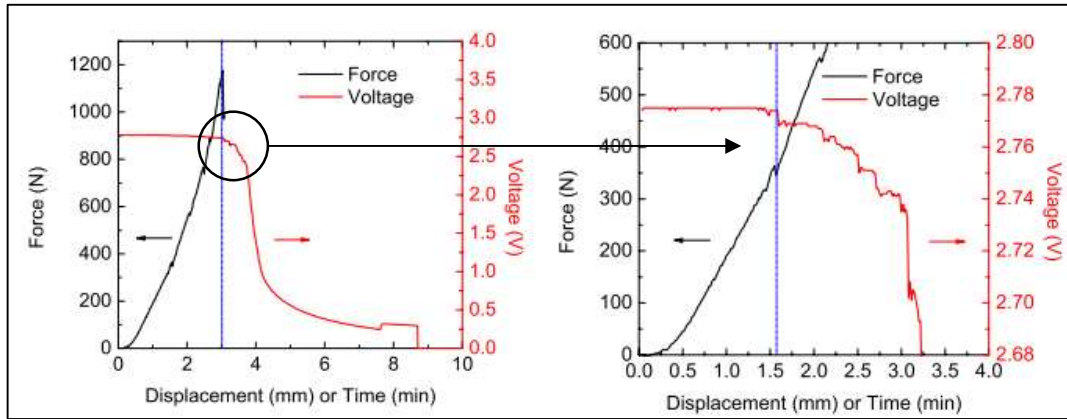


Figure 1.14 - Short circuit voltage curve (a), with detail of soft short circuit (b) [13]

The graphs in Figure (1.14) show the behaviour of the electric potential inside the cell during a test in which the mechanical load is applied locally through a hemispherical impactor. The increase of the displacement inside the cell determines a short circuit [13].

Internal short circuit is inducted in a cell when the electrodes are in contact, the consequence is a drop voltage in the cell. Depending on the entity of the drop it is possible to distinguish two kinds of short circuits.

**Hard short circuit:** solid connection between electrodes causes extremely high current flow and complete discharge, resulting in permanent damage to the cell. The cell voltage collapses to 0 V, and the cell effectively acts as a resistor in the overall circuit. [5]

**Soft short circuit:** is caused by small localized contact between electrodes. It may be self-correcting due to melting of the small regions in contact caused by the high current flow, acting as a local fuse, and interrupting the short-circuit current. A cell with a soft short is still operational, but has a high self-discharge rate. [5]

In Figure (1.14-b) the transient of the drop voltage is highlighted, and, as observable, the voltage drop is not immediate until reaching a displacement of 3 mm. The small and gradual drop starting from a displacement of 1.5 mm to 3 mm could be considered a soft short circuit before the hard one.

Further investigations on the separator failure mode lead to the definition of different failure conditions depending on the conditions of rupture of the layer.

## 1.4 Modelling strategies for Lithium-ion batteries

When dealing with complex systems like batteries, a modelling strategy usually represents a strong resource for better understanding of the phenomena that happen inside the system itself. The modelling phase is only a part of a bigger process that aims to the optimization and comprehension of undesired behaviours. Generally speaking, the phases of this process can be represented in a graph as in Figure (1.15).

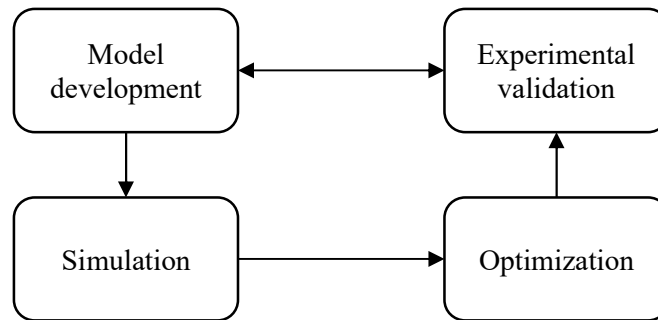


*Figure 1.15 - Modelling phases map [11]*

An important task is to experimentally validate the chosen model to ensure that the model predicts the experimental data to the required precision with a reasonable confidence. This task is typically performed in part for experiments designed to evaluate the descriptions of physicochemical phenomena in the model whose validity is less well established. However, in a materials system such as a lithium-ion battery, most variables in the system are not directly measurable during charge-discharge cycles, and hence are not available for comparison to the corresponding variables in the model to fully verify the accuracy of all of the physicochemical assumptions made in the derivation of the model [4]. Also, model parameters that cannot be directly measured experimentally typically have to be obtained by comparing the experimental data with the model predictions. A trial-and-error determination of battery design parameters and operating conditions is inefficient, which has motivated the use of battery models to numerically optimize battery designs. This numerical optimization can be made more efficient by use of reformulated or reduced order models. Simulation time plays a role in determining the use of these models in various applications, and high simulation times have limited the application of battery optimization based on physics-based models [4]. Efficient way of simulating battery models is an active area of research and many researchers have published various mathematical techniques and

methods to simulate physics-based battery models faster.

Modelling strategy for batteries can be regrouped in three big categories: empirical models, multiphysics models and electrochemical-based models [14]. Each of these categories includes different modelling approaches that allow to reach different results. The following chart sums up the main modelling strategies (Figure (1.16)).

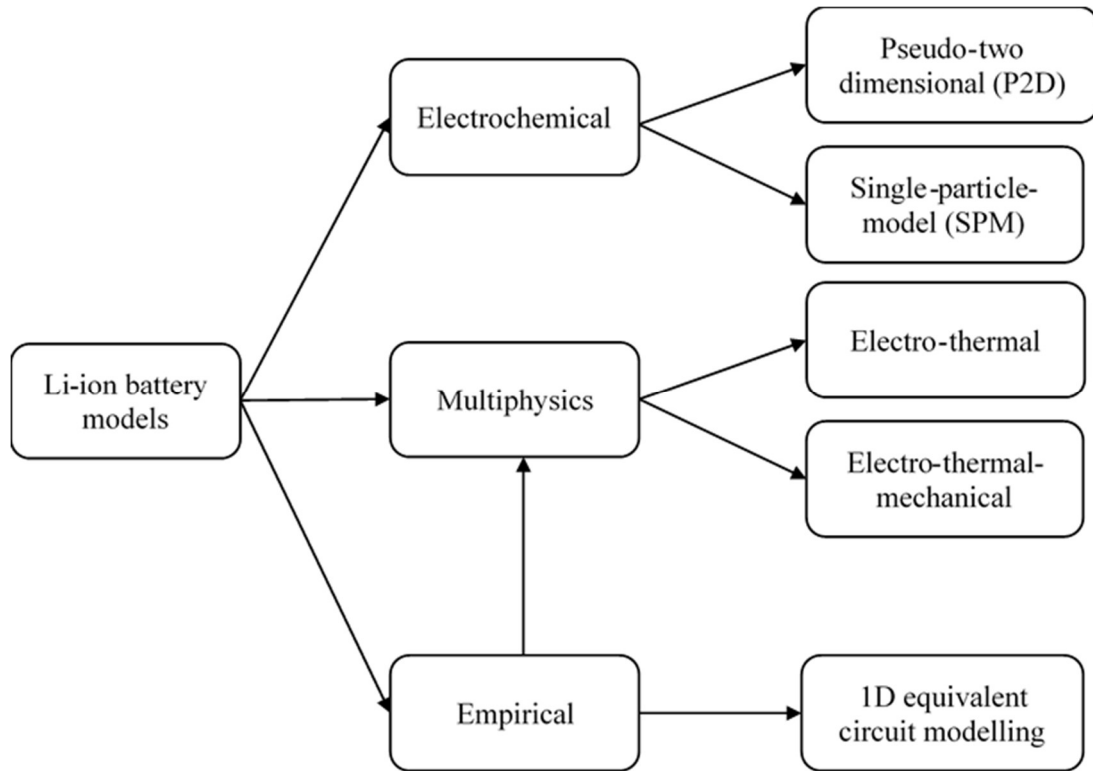


*Figure 1.16 - Modelling strategies for Lithium-ion batteries [13]*

### 1.4.1 Empirical models

The empirical model characteristic is the employment of past experimental data in order to predict the future behaviour of the battery, not keeping in account physicochemical principles.

An example of empirical approach to modelling batteries is the 1D equivalent circuit modelling. It represents a battery performance model used to simulate the dynamic characteristics of a Li-ion battery using resistance, capacitance, voltage source, and other circuit components to form a circuit [15].

The accuracy of the results is strictly related to the complexity of the circuit, in terms of electric components as well as to the precision of the numeric input parameters ruling the components.

As an example, the equivalent circuit employed in the battery analysis of this work of thesis is showed in Figure (1.17).

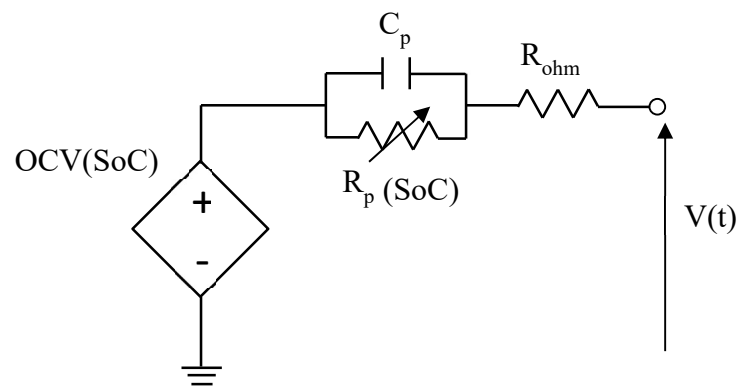


Figure 1.17 - Example of RC-R 1D equivalent circuit

This RC circuit is able to reproduce the electrical behaviour of the battery during charging and discharging cycle, and provide as a result the voltage curve.

The lumped parameters that rule the circuit are not all constant in time, in fact, the controlled generator models the Open Circuit Voltage Curve as a function of the State of charge, as well as the polarization resistance resistor models the variation of the internal resistance through the charge/discharge process. This aspect makes the model empiric, because the law of variation of these parameters must be deduced from previous experimental data (charging/discharging curves).

The description and characterization of the lumped parameters employed in this work will be explained in the next chapters.

Although the dependence from previous data could be a limit for this kind of models, they represent a starting point for the development of models of greater complexity like FEM Multiphysics models.

### 1.4.2 Multiphysics models

One of the most important aspects in the analysis of Lithium-ion cells is surely the heat generation and distribution, especially in high power/energy application such as in hybrid/electric vehicles [4]. This aspect arises the necessity of coupling the electrical modelling side to a thermal analysis. Electro-thermal models aim to link the electrical and thermal behaviour of a cell in order to obtain a integrated model, with mutual dependence of the involved parameters.

An example of this dependence is that the temperature distribution on the battery surfaces is related to the current distribution into the battery itself. For this reason, an averaged analysis of the thermal behaviour of a cell cannot be considered exact. The discretization of the battery in small systems can be the solution to this critical point. Finite element models allow to evaluate more accurately distributions of both electrical and thermal quantities in the analysed system. FEM modelling results particularly efficient for the observation of thermal gradients inside the cells, and so for the temperature distribution estimation [16]. An example of the results achievable with this modelling strategy is showed in Figure (1.18).

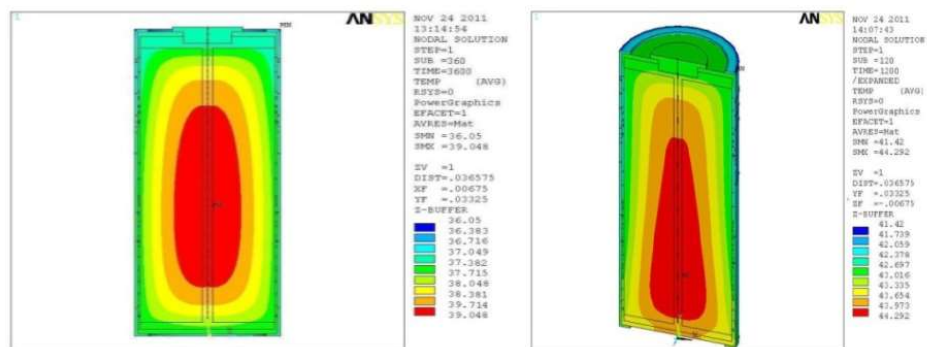


Figure 1.18 - Temperature scene from a FEM simulation on cylindrical cell [16]

In this case of study, simulations were conducted on a cylindrical cell, revealing interesting local temperature distributions and revealing correlations with the working conditions in terms of applied currents.

The increasing interest in the study of mechanical abuse conditions on batteries led to the necessity of a further coupling of electro-thermal models with mechanical simulations. In

literature few examples of this studies are present, and usually follow a one-way coupling approach, and no information from the electrical or thermal simulations is returned back to the mechanical solver (Figure (1.19)). The limitation of this approach is that the mechanical deformation resulting from changes to the material properties (e.g., melting of different cell components) is not captured in modelling the thermal/electrical propagation [17].

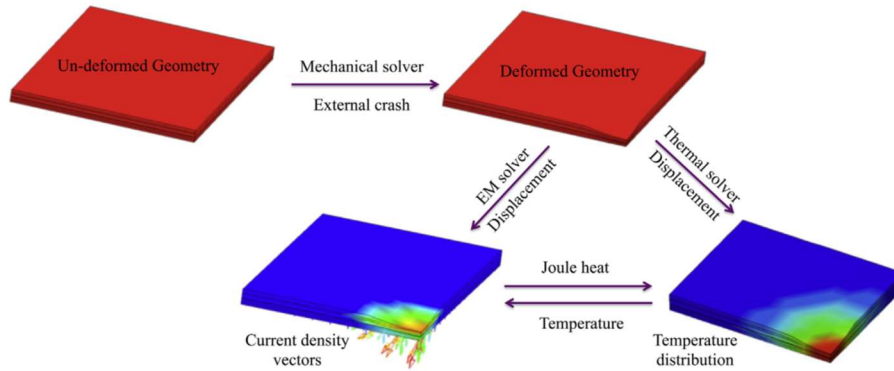


Figure 1.19 - Modelling phases for a mechanical-electro-thermal model [17]

### 1.4.3 Electrochemical models

A first-principle based model [15] differs from an empirical model for the total absence of experimental data in the model development process. In other words, this class of models does not require parameters tuning, basing on real results coming from any kind of practical investigation.

Electrochemical models belong to this class and represent the most complex approach to battery modelling. These are able to reproduce the physicochemical phenomena that take place inside the cell including kinetics and transport dynamics in order to produce extremely accurate predictions. In a full electrochemical model, the main equations to be solved regard diffusion in solid particles. Results determine the lithium concentration in the electrode particles and provides information on the level of lithium available for producing an electrical charge. In other words, it provides information to users about the remaining level of electrical energy in the battery [17]. The most spread and used electrochemical models are Pseudo Two Dimensional (P2D) and Single Particle Model (SPM).

P2D models are based on the theory of porous electrodes [4]; this feature increases the interfacial area between the solid and the electrolyte solution and, as a result, it dampens the negative effects of the slow electrochemical reactions. The electrodes are considered as a

porous matrix and their behavior is modeled with spherical particles surrounded by the electrolyte (Figure (1.20)). The intercalation and the de-intercalation processes of the Li-ions are performed through the surface area of these particles [14].

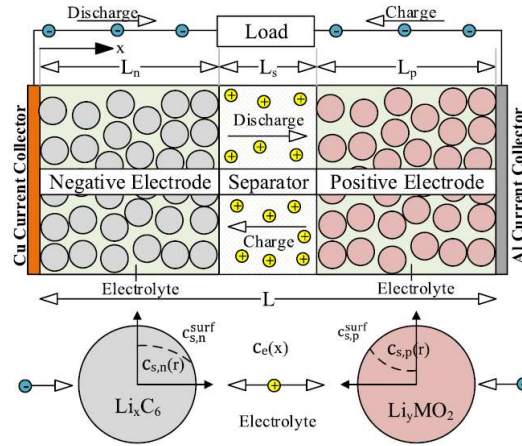


Figure 1.20 - P2D model schematic structure [14]

The governing equations for this kind of models can be summed up in the following points:

- the solid-state Li-ions concentration in the electrodes is derived from Fick's law of diffusion for spherical particles;
- the liquid-phase Li-ions concentration in the electrolyte and in the separator is based on the conservation of Li-ions;
- the solid-state potential in the electrodes is derived from Ohm's law;
- the liquid-phase potential in the electrolyte and in the separator is calculated using Kirchhoff's and Ohm's laws;
- the pore wall flux of Li-ions in the electrodes is described by the Butler-Volmer kinetics equation.

The complexity of the solution research for such a wide range of phenomena kept in account leads to the necessity of the implementation of these models in FEM or FVM, obtaining really accurate results, at the cost of a great computational effort.

For this reason, a simplification of this approach can be identified in the Single Particle Model. SPM incorporates the effects of transport phenomena in a simple manner. A model of diffusion and intercalation within a single electrode particle, which was expanded to a sandwich by considering the anode and cathode each as a single particle with the same

surface area as the electrode.

In this model, diffusion and intercalation are considered within the particle, but the concentration and potential effects in the solution phase between the particles are neglected. Due to these simplifications, this model can be quickly simulated, but is only valid for limited conditions [14].

## ***CHAPTER 2***

### ***2. From the experimental investigation to the modelling strategy***

#### ***2.1 The cell under test***

The experimental investigation was conducted on a Li-ion pouch cells extracted from a battery pack of 24 battery modules, each of which containing 8 pouch cells (Figure (2.1)). The capacity of a single cell is 41Ah with cut-off voltage limits of 2.5 V and 4.2 V.



*Figure 2.1 - Pouch cell employed in tests*

From a purely geometrical point of view the surface dimensions of the pouch cell are 0,22 m x 0,2 m with a thickness of approximately 8mm.

Further information about the cell internal arrangement come from a microscopical analysis conducted by the institute on one of these cells.

Results coming from the scanning electrode microscope (SEM), revealed the precise distribution of layers inside the cell and their geometrical properties. An EDEX Super Octane energy-dispersive X-ray spectroscopy device was used, instead, to investigate the chemical composition of each part of the cell [19].

From this chemical analysis, a high carbon (C) content, allowing the classification of the anode active material as graphite, while for the cathode active material, chemical elements identified by using EDXS were manganese (Mn), cobalt (Co), nickel (Ni), oxygen (O), and carbon (C). This led to the conclusion of a  $\text{LiNiMnCoO}_2$  (NMC) cathode chemistry [19].

Regarding the SEM results, a precise definition of layer thicknesses and distribution was obtained. The cell is made of 22 anode layers, 21 cathode layers and 44 separator foils.

Layer thicknesses can be evaluated in Figure (2.2), where, starting from the left, in sequence there are: a separator layer, the cathode electrode, formed by the Aluminium current collector (CC) and the Graphite coating (AM), then, another separator layer and the anode electrode, composed by the Copper current collector (CC) and the NMC coating (AM) [19].

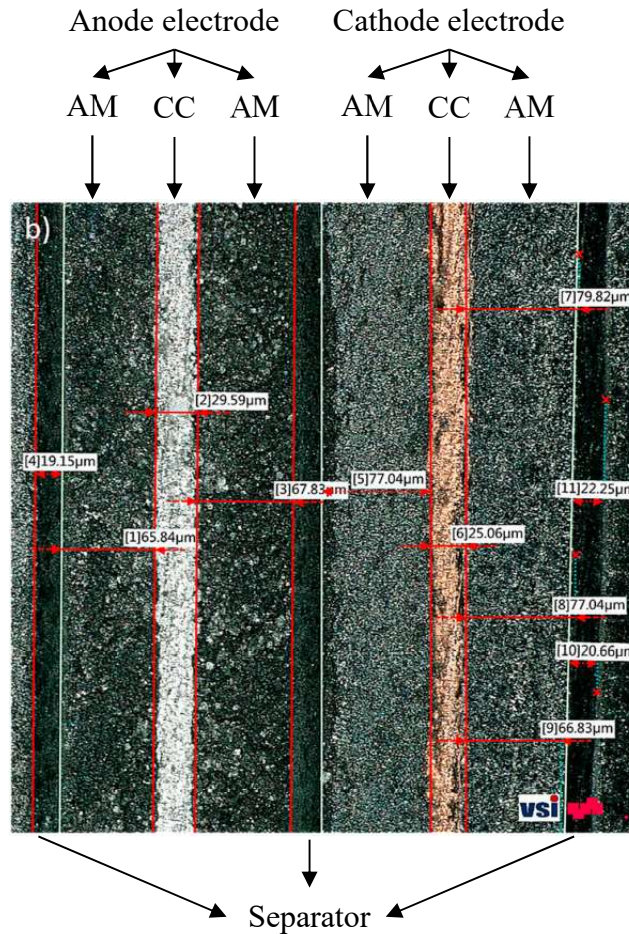


Figure 2.2 - Cell internal layer arrangement [19]

The values of layer thicknesses are summed up in Table (2.1).

Component	Thickness (µm)	Component	Thickness (µm)	Component	Thickness (µm)
<b>Anode</b>	140	<b>Cathode</b>	170	<b>Separator</b>	20
Anode CC	10	Cathode CC	20	<b>Pouch</b>	190
Anode AM	65	Cathode AM	75		

Table 1- Layer thicknesses [19]

## 2.2 Test setup and methodology

The target of the experimental investigation was to evaluate the effects of a local, non-disruptive deformation performed on the just described cell, when the cell is subjected to different kinds of electrical loading conditions.

Regarding the mechanical loading condition necessary to deform the cell in a non-severe way, from preliminary studies, the choice of a hemispherical impactor resulted the easiest and safest way to achieve the result (Figure (2.3)). Tests revealed as the pouch cell was able to allocate up to 3mm of displacement before entering a hard-short circuit condition, so, this threshold was used to design a proper impacting element.

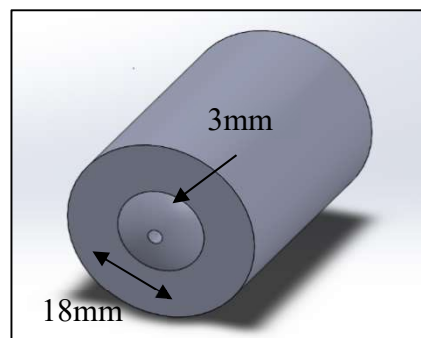


Figure 2.3 - Impactor design

In order to properly apply the impacting element, a “sandwich” configuration of metal plates and insulating layers was employed to enclose the cell and grant a precise realization of the dent.

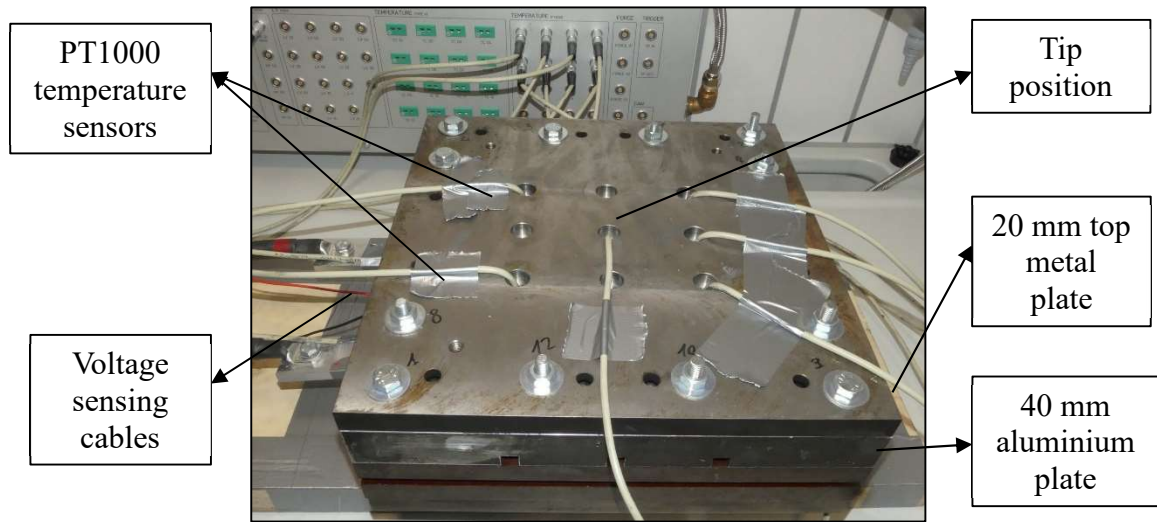


Figure 2.4 - Test bench set up with lower insulating layer

The pouch cell is positioned on a Pertinax layer (Figure (2.4)), an electrical insulator, for safety reasons, in order to avoid the direct contact with the underlying metal plate. Two

aluminum pliers are connected to the battery tabs to provide current, then the upper part of the testing structure can be mounted.

The tip was designed to be allocated through a drilled aluminum plate in order to be compressed between the upper metal plate and the cell. The whole sandwich was then locked with 12 M8 bolts tightened with a torque wrench at 3Nm torque (Figure (2.5)).



*Figure 2.5 – Complete test bench set up*

During tests, voltage and temperature are measured: voltage is measured through two crocodile clips clamped at anode and cathode tabs, while temperature is measured in different points employing PT1000 Platinum sensors. One of these is positioned exactly in the center of the impactor, in contact with the cell, through a hole in the impactor itself.

Data coming from measurements are collected by the battery tester with a sampling frequency of 2000 Hz.

When test is completed, removing the insulating sheets and metal plates, the effect of the impact is immediately evident (Figure (2.6)).



*Figure 2.6 - Cell after mechanical deformation*

### **2.3 Loading conditions and results from experimental investigation**

The evaluation of the effects of the deformation was possible repeating the same test both on the pristine and the deformed cell. In order to grant the correctness of the results, each test was conducted on three cells, before and after the deformation. Electrical loading condition can be identified by two aspects: range of SoC under investigation, C-rate of the charge/discharge.

On the basis of these main aspects tests are summed up in Table (2.2):

C-rate	SoC-Range	N. cycles	Target
1C-2C-3C	0→90%	1	Voltage relaxation effects
	20→30%	5	Variation of internal resistance

*Table 2 - Testing conditions table*

The most important results in terms of modelling regarded the 20-30% SoC cycling, while the other testing condition will not be analyzed in this work of thesis.

The choice of this SoC range for cycling was based on the high values of internal resistance of the cell at low state of charge, between 20 and 30%, in order to enhance eventual variation of the resistance itself due to deformation.

Tests revealed interesting results in terms of internal resistance variation, comparing voltage curves in pristine and deformed conditions.

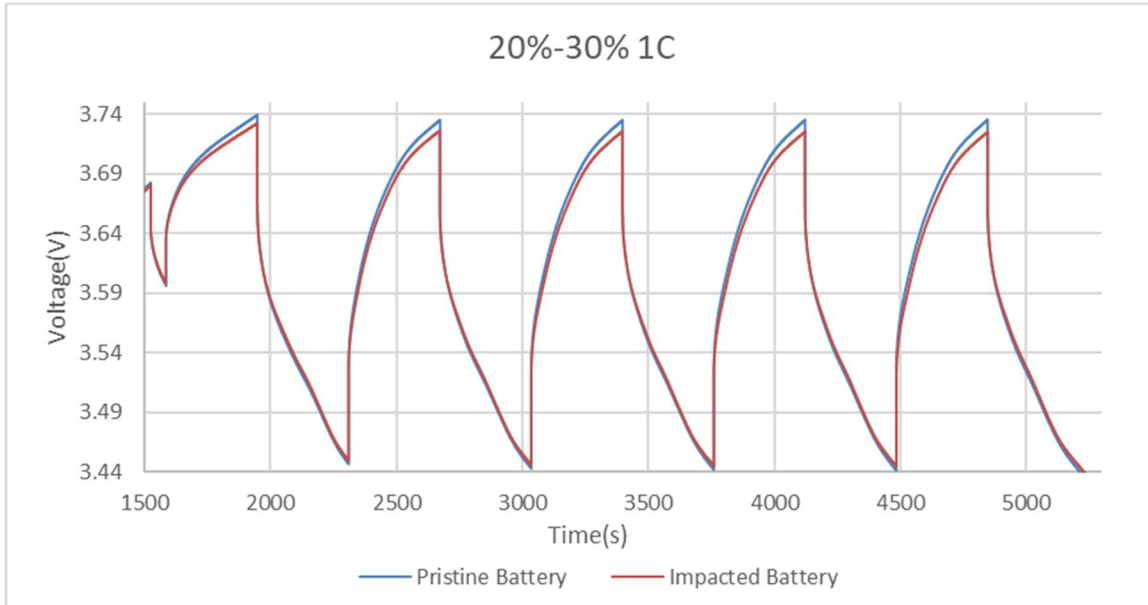


*Figure 2.7 - Cycling 1C 20%-30% pristine Vs deformed cell voltage curves*

The above graph (Figure (2.7)) shows the trend of measured terminal voltage comparing the curve before and after the deformation for 1C rate (40A).

The electrical cycle can be summed up by the following sequence.

1. Time: 1520 battery is charged up to 20% SoC at 1C rate
2. Time: 1520-1580 battery is resting with no current application
3. Time: 1580-1940 battery is discharged at 1C rate
4. Time: 1940-2300 battery is charged at 1C rate

Then the charge/discharge cycle is repeated for a total of 5 cycles.

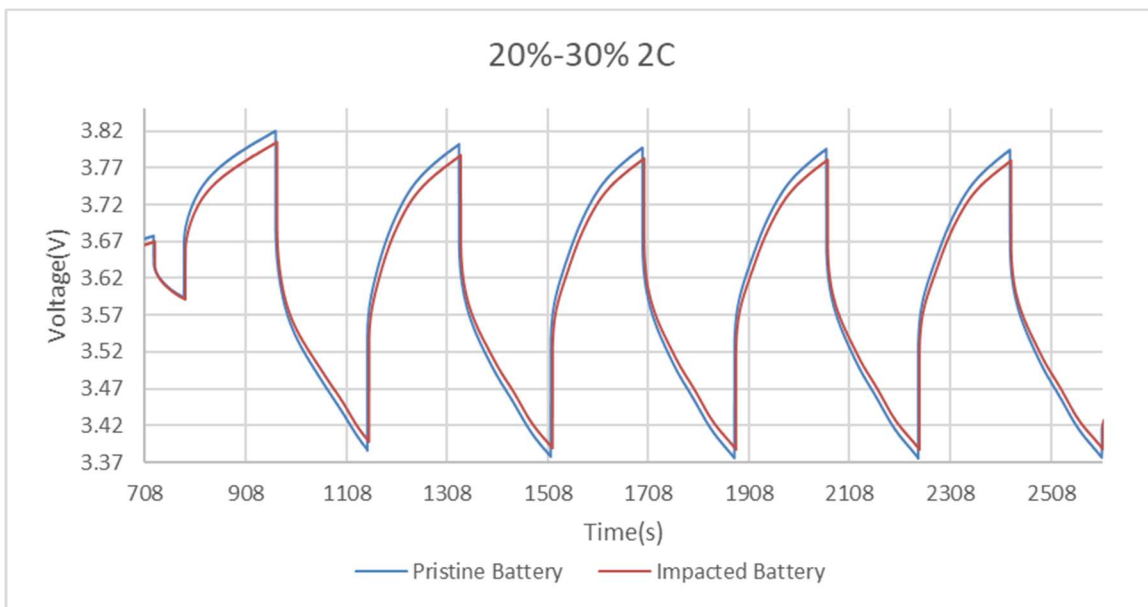


*Figure 2.8 - Cycling 2C 20%-30% pristine Vs deformed cell voltage curves*

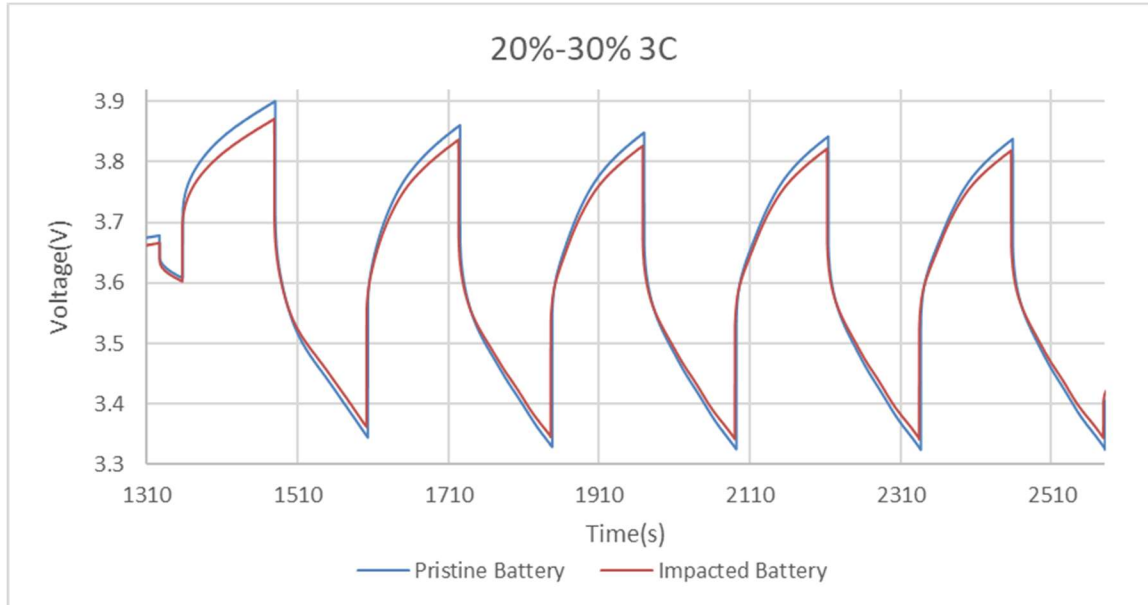


*Figure 2.9 - Cycling 3C 20%-30% pristine Vs deformed cell voltage curves*

The same cycle was repeated also for 2C-rate (80A) (Figure (2.8)) and 3C-rate (120A) (Figure (2.9)), with these values of current employed only in steps 3 and 4, for the 5 cycles. A preliminary observation of the obtained data highlighted variations in terms of peak to peak voltage during the cycling phase in all C-rate conditions.

In particular, the voltage curve of the damaged battery is always enclosed between the maximum and minimum values of the pristine battery voltage curve. This means that the voltage excursion is reduced of a certain effort depending on SoC, due to an internal resistance reduction. The evaluation of the effort of this variation will be conducted in the next sections. Temperature measurement did not report significant differences comparing pristine and deformed cell.

## ***2.4 Modelling strategy to reproduce test conditions***

Once obtained results from experimental investigation, it was necessary to define a modelling strategy to reproduce the observed phenomena in a simulation environment.

The target of modelling is to provide a reproduction of the real system, but with the advantage of having full control of the internal parameters ruling the physics of the phenomenon. In this case of study, in particular, the aim is to understand how the internal resistance of the cell could vary due to a non-disruptive localized deformation. The localization of the damage, moreover, can lead to the analysis of the local variation of the parameter in the damaged area.

The steps followed for the model set-up are summed up in Figure (2.10).

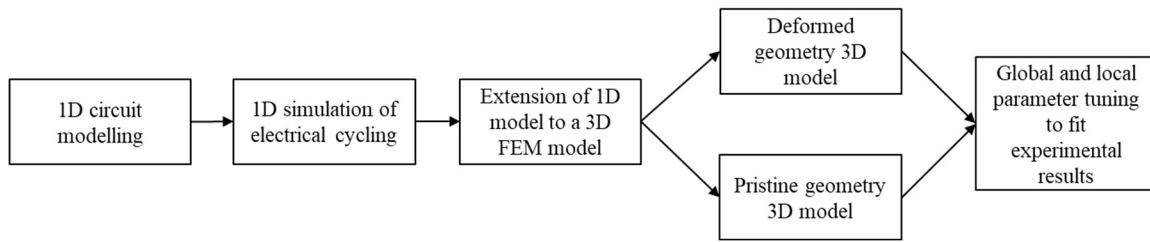


Figure 2.10 - Modelling strategy chart

The starting point is represented by the 1D equivalent circuit model. In this work of thesis, the employed 1D strategy refers to a previous work, in which the evaluation of the internal parameters of the battery cell was carried out.

### 2.5 State of art of 1D circuit model

As anticipated in section 1.4.1, an equivalent circuit model, constitutes a lumped parameter representation of a battery cell. Different circuit configurations are available in literature, and in the current analysis Weilin Luo's equivalent circuit is employed and represented in Figure (2.11).

This circuit models the battery with 3 main electrical components:

- OCV voltage controlled generator, as a function of SoC,
- a RC polarization couple, representing the part of internal resistance dependent on SoC
- a pure ohmic resistance not dependent on SoC

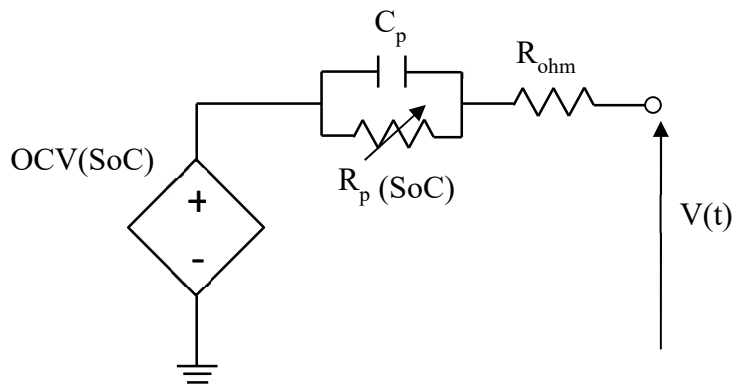


Figure 2.11 - Weilin Luo's equivalent circuit model

Solving the circuit with Kirchhoff's law, and considering a constant current flowing in the circuit (capacitance in open circuit condition), the terminal voltage  $V(t)$  can be expressed

as:

$$V(t) = OCV(SoC) - I(R_p(SoC) + R_{ohm}) \quad (2.1)$$

The voltage law just defined makes possible to compute the value of the internal resistance of the cell starting from the measured terminal voltage  $V(t)$  if the value of current and OCV is well known at any SoC. Generally, during charging and discharging process the electric current involved assumes constant values, so, the only quantity to be defined is the OCV.

### 2.5.1 Lumped parameters evaluation

The values of lumped parameters were obtained starting from data coming from charging/discharging curves at different C-rates. The first measure necessary to deduce the values of internal resistance is the OCV(SoC) curve. The curve in Figure (2.12) was obtained discharging a full charged cell from 100% to 0% SoC, with a very low value of current, about C/40 (1A). The following curve relates the open circuit voltage to the discharged capacity. This quantity represents the portion of capacity consumed at a certain instant, and it is related to SoC through the following equation:

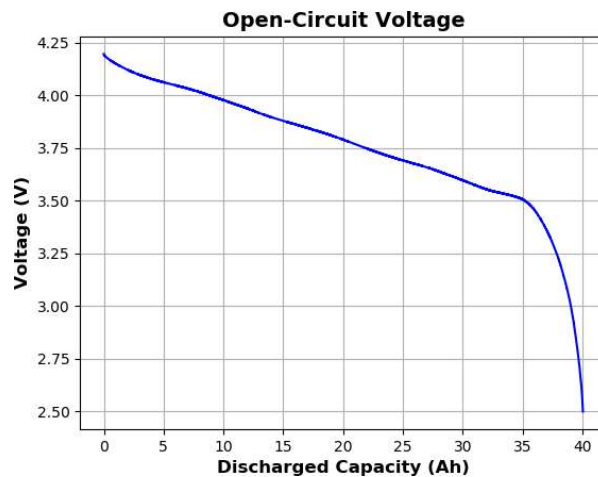


Figure 2.12 - OCV curve with respect to discharged capacity

$$SoC = 1 - \frac{\text{Discharged capacity}}{\text{Rated capacity}} \quad (2.2)$$

Once obtained this curve the internal resistance can finally be evaluated. The two contributions defining the total resistance refer to two different resistive aspects of the cells. The Ohmic contribution is associated to the pure resistance of the current collectors. Its value can be considered independent on the state of charge, since it is mainly related to the physical properties of the constituent materials, as the electrical conductivity, and to the geometry. The presence of an Ohmic resistance causes an immediate voltage drop when a

current pulse is applied (Figure (2.13)).

The value of this part of the resistance can be calculated applying a certain known current and measuring voltage difference between the OCV value at full charge and the terminal voltage at the immediate time instant after the current application.

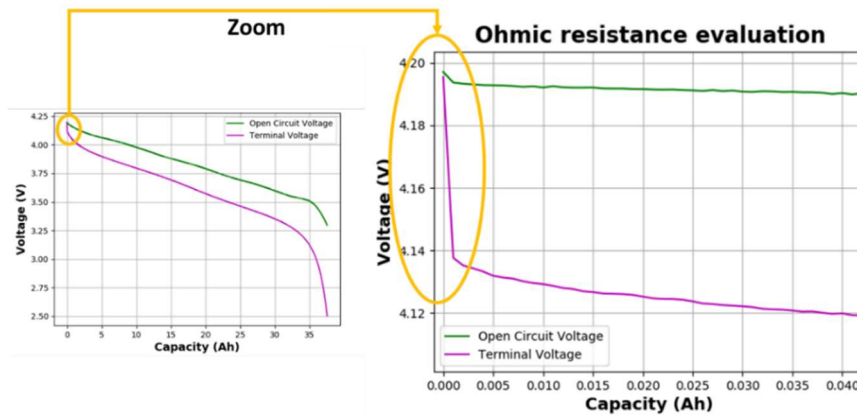


Figure 2.13 - Ohmic resistance evaluation

The measure of the resistance resulted about  $0.7\text{m}\Omega$ . The polarization contribution, instead, represents the dynamics of the charge transfer process, describes the status of the polarization. In the initial and middle stage of the discharge cycle, the cell reactants are enough and the electrochemical reactions take place easily, this contribution maintains a small value. In the late stage of the discharge cycle, the reactions cause the cell reactants to be used up rapidly near the end of the discharge resulting in a sharp increase. Analytically the polarization resistance curve can be obtained as:

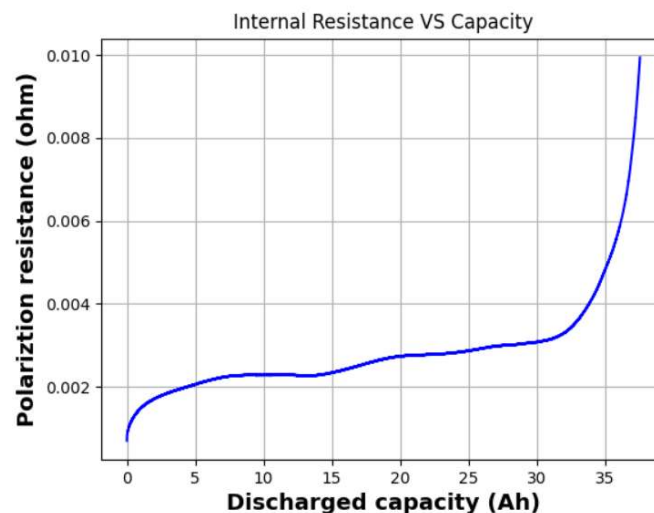


Figure 2.14 - Interval resistance VS discharged capacity curve

$$R_p = \frac{OCV(SoC) - V(t)}{I} - R_{ohm} \quad (2.3)$$

This curve was fitted with an exponential behaviour in order to obtain a function dependent on few parameters, instead of a full experimental set of points (Figure (2.14)).

Polarization resistance is not only a SoC dependent quantity, but also a current dependent. For higher C-rates the polarization resistance increases earlier in terms of discharged capacity. In order to obtain a function able to describe the correct value of resistance for any SoC, a new quantity is introduced, the relative state of charge ( $SoC_r$ ).

$$SoC_r = 1 - (1 - SoC) \frac{Q}{Discharged\ capacity(I)} \quad (2.4)$$

In this equation, the value of state of charge is reduced of a factor  $\eta$  defined as the ratio between the rated capacity and the discharged capacity as a function of the applied current. Entering the polarization resistance curve with relative state of charge instead of state of charge allows to obtain the real value of the polarization contribution also related to the applied current.

A further improvement of the resistance estimation was obtained through an Electrochemical Impedance Spectroscopy (EIS) analysis conducted on the cell that revealed the necessity to modify the pure resistive equivalent circuit into a RC-R model.

In particular, the impedance behaviour was fitted with a 5<sup>th</sup> order RC parallel circuit, but considering the very low contributions in terms of time constant of four of these RC parallels, their impedance was reduced to a pure resistive contribution. The remaining RC couple had a not negligible time constant, in order of thousands of seconds. For this reason, the polarization resistance was divided in two parts, a constant one, included in the constant value  $R_{ohm}$ , representing the four RC parallels with low time constant, and the effective polarization resistance contribution that is in parallel with a capacitor, with a time constant of 60s.

## 2.5.2 1D simulation of 20-30% SoC electrical cycling

Once defined the lumped parameters of the circuit, a set of differential equations must be defined in order to obtain as output of the system the terminal voltage trend in time. The equations can be written in continuous or discrete time; in this analysis the discrete-time approach is used.

$$V[k + 1] = V[k] - (R_{ohm} + R_p)I[k] \quad (2.4)$$

$$R_p[k + 1] = R_p[k]e^{-\frac{\Delta t}{\tau}} + (1 - R_{psteady})[k]e^{-\frac{\Delta t}{\tau}} \quad (2.5)$$

$$SoC[k + 1] = SoC[k] - \frac{\Delta t}{Q}I[k] \quad (2.6)$$

$$SoC_r[k + 1] = SoC_r[k] - \frac{\Delta t}{Q}\eta[k]I[k] \quad (2.7)$$

Where  $\Delta t$  is a chosen time step, that distances time instant  $k$  from time instant  $k+1$ .

Providing to the equation solver these equation, and a proper set of data defining OCV curve and the polarization resistance values, the value of the terminal voltage  $V[k]$  can be calculated. The equivalent circuit was solved writing a Python script, where experimental data are loaded and employed to solve equations in discrete time.

As an example, the electrical cycling between 20-30% SoC at 1C rate is reported.

In order to simulate an electrical cycling, the value of current must vary at defined time instants, when the process switches from charging to discharging and vice versa. For this reason, the value of current is defined for time ranges, depending on the state of charge to be achieved. This is possible defining an if cycle inside the iterating cycle for the solution of the equations (Figure (2.15)).

```
#Electrical cycling
for i in range (len(time)):
    if time[i]<=3555:
        I = 40
    elif time[i]>3555 and time[i]<=4275:
        I= -40
    elif time[i]>4275 and time[i]<=4305:
        I= 0
    elif time[i]>4305 and time[i]<=4665:
        I= -40
    elif time[i]>4665 and time[i]<=5025:
        I= 40
    elif time[i]>5025 and time[i]<=5385:
        I= -40
    elif time[i]>5385 and time[i]<=5745:
        I= 40
    elif time[i]>5745 and time[i]<=6105:
        I= -40
    elif time[i]>6105 and time[i]<=6465:
        I= 40
```

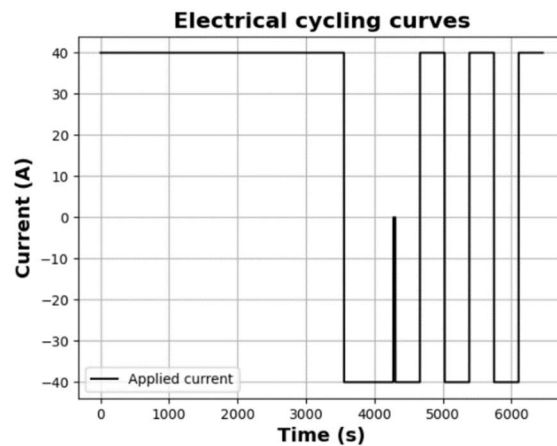
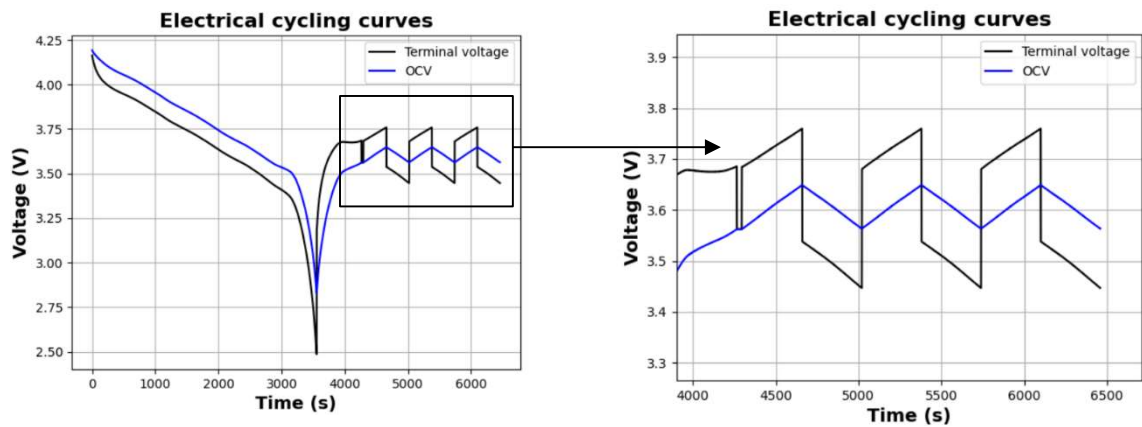


Figure 2.15 - Python cycle defining current profile for electrical cycling

The cycle defines a positive current when discharging and a negative current when charging. When the value is null, the battery is resting, before starting the effective electrical cycling. In Figure (2.16) terminal voltage is plotted along with OCV. An interesting aspect to be observed is how the terminal voltage curve stays under OCV curve when discharging and over OCV curve when charging. Each time the current value changes in sign, an immediate voltage drop is present, and its effort is equal to the double of the difference of voltage between the two curves.



*Figure 2.16 - Electrical cycling curves and relationship with OCV curve*

Results coming from this simple simulation resulted coherent with the measured values acquired during experimental investigation, with correspondent peak to peak values of terminal voltage during electrical cycle, in a tolerance of about  $\pm 0.02V$ .

Once obtained a correspondence in 1D equivalent circuit, the next step of modelling process is the creation of a 3D FEM model, where the concept of this simple circuit will be extended to the finite elements of the discretized continuum.

## ***CHAPTER 3***

### ***3. Model set-up with deformed geometry***

#### ***3.1 STAR CCM+ environment for Finite Element Method analysis***

The realization of the multiphysics model was carried out in Siemens STARCCM+, a Computational Aided Engineering software that provides tools for modelling and simulation of any kind of problems in both fluid and solid continuum mechanics, within a single integrated user interface. Once obtained a complete model, the simulation process requires the resolution of the equations governing the domain, therefore, a proper solving strategy is needed. FEM is a particular numerical method for solving partial differential equations in two or three space variables. To solve a problem, the FEM subdivides a large system into smaller, simpler parts that are called finite elements. This is achieved by a particular space discretization in the space dimensions, which is implemented by the construction of a mesh of the object: the numerical domain for the solution, which has a finite number of points [20]. The finite element method formulation of a boundary value problem finally results in a system of algebraic equations. The method approximates the unknown function over the domain. The simple equations that model these finite elements are then assembled into a larger system of equations that models the entire problem. The FEM then uses variation methods from the calculus of variations to approximate a solution by minimizing an associated error function [20].

#### ***3.2 Workflow of model realization***

Setting up the model requires a standard procedure, that starts from the geometric definition of the pouch cell and ends with the simulation operations. The steps followed are:

1. Import the deformed mesh geometry
2. Definition of regions and assign part to regions
3. Definition of interfaces between regions
4. Definition of physics continua
5. Definition of field functions for the internal equivalent circuit modelling
6. Simulation for model validation

All these steps will be explained in the following paragraphs

### 3.3 Deformed geometry realization and import

The deformed mesh was obtained starting from non-deformed one generated in ABAQUS CAE, through a mathematical manipulation of the nodes positions. Once generated, mesh data are stored in a .inp file. Each node is associated to a node number and three spatial coordinates in separated lines (Figure (3.1)).

8	*Part, name=Anode_CC			
9	*Node			
10	1,	0.699999988,	50.,	-185.
11	2,	0.699999988,	50.,	-115.
12	3,	0.699999988,	70.,	-115.
13	4,	0.699999988,	70.,	-185.
14	5,	0.709999979,	50.,	-115.

Figure 3.1 - Example of .inp file

Practically, the deformation was carried out employing an impactor whose geometry was derived from a hemisphere of radius 15 mm, so, it was necessary to obtain the same deformation profile in the mesh. The depth to be reached by the tip of the impactor into the pouch cell was 3 mm. A sketch view of impactor designed is reported in Figure (3.2).

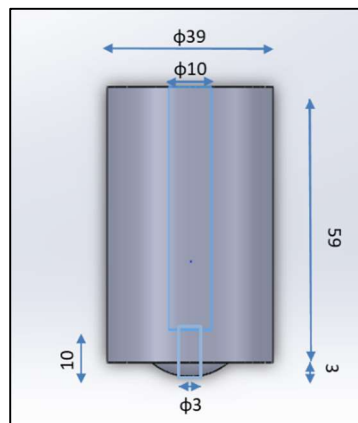


Figure 3.2 - Impactor technical representation

The displacement of the nodes was assumed to take place only on the X-axis, so, a proper mathematical function able to change the X-coordinate of a node for a certain (Y, Z) couple was developed. The choice of the mathematical function was based on the analysis of the expected shape of deformation. Although the regularity of the impactor (a trunk of hemisphere), a semi-circular path would not have been able to reproduce the attenuation of the deformation in the nearby of the deformed area as showed in Figure (3.3).

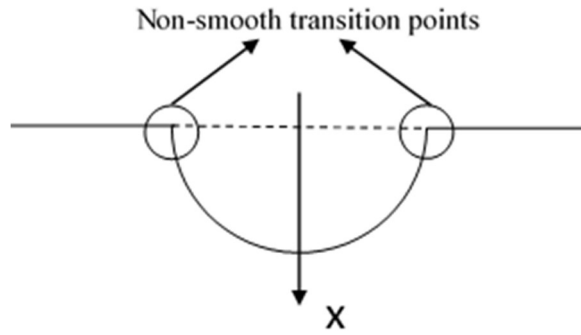


Figure 3.3 - Non-smooth transition profile

For this reason, the probability density function from Gaussian distribution was chosen as a starting point, in order to exploit the shape of the side tails as attenuation of deformation profile.

$$f(x) = \frac{1}{\sigma\sqrt{2\pi}} e^{-\frac{1}{2}\left(\frac{x-\mu}{\sigma}\right)^2} \quad (3.1)$$

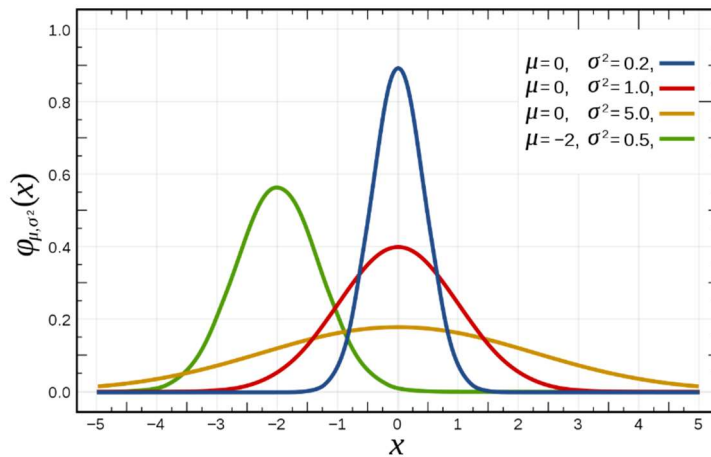
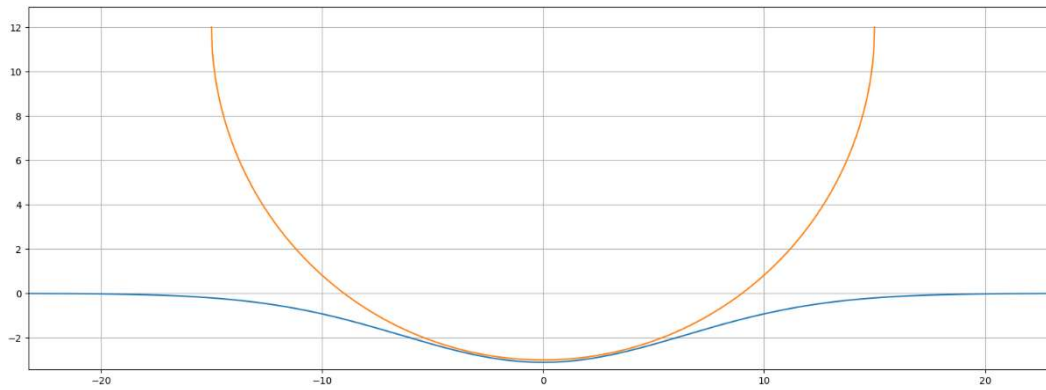


Figure 3.4 - Gaussian function

As observable, the shape and shifting of the curve depend on two parameters, the mean  $\mu$  and the standard deviation  $\sigma$ . The value of the mean was set to zero, because no shifting is needed, while the value of  $\sigma$  represents the tuning parameter for the amplitude of the curve. At a first attempt, it was possible to set the value of  $\sigma$  to a constant value in order to obtain a match at the maximum displacement point of the deformation path.



*Figure 3.5 - Mismatch between semicircular profile and Gaussian profile*

The tuning allows to obtain a curve that matches the desired profile only in the deepest part (2-3 mm), but an evident mismatch between impactor profile and mathematical function is observable in the rest of the curve (Figure (3.5)).

A perfectly matching curve requires a variation of  $\sigma$  along with the distance from the center of the curve, so, it is necessary to define a proper function  $\sigma=f(x)$ .

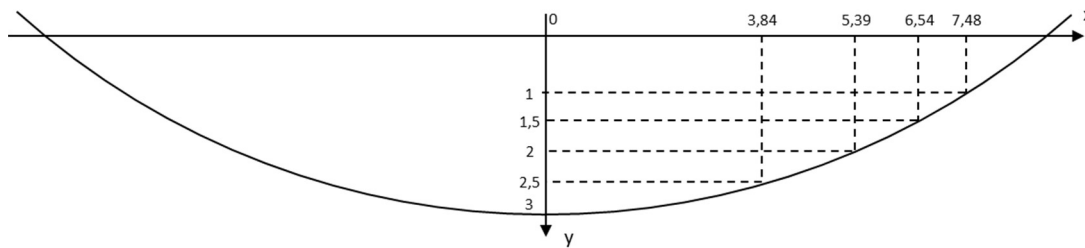


*Figure 3.6 - Definition of a set of points on circular profile*

Starting from a set of points belonging to the desired deformation circumference, showed in Figure (3.6), the correspondent values of  $\sigma$ , needed to model the distribution function shape, were calculated.

These values were used to derive a 6th grade polynomial function, able to describe the variation of  $\sigma$  and granting a precise reproduction of the deformation profile. All the described steps and the polynomial formulation were performed using `numpy.polyfit` function in Python as showed in Figure (3.7).

```

#Ideal sigma calculation for points (X_deep,Y_deep)

sigma_array=[]
sGuess=8

for i in range (len(X_deep)):
    def sigma_fun(s):
        Eq=-Y_bot[i]+(50/math.sqrt(2*math.pi*s**2))*math.exp(-1/2*(X_deep[i]/s)**2)
        return Eq
    sigma_array.append(fsolve(sigma_fun,sGuess))

#Polynomial function definition using polyfit, 6th rank
par = np.polyfit(X_deep, sigma_array, 6)

```

Figure 3.7 - Code for definition of sigma variation law

The obtained polynomial curve resulted a monotonous growing function of  $\sigma$  with respect to the distance from the central point. The function plot is showed in Figure (3.8).

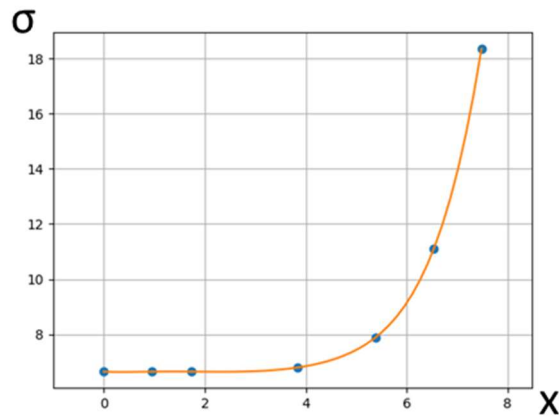


Figure 3.8 - Polynomial sigma function plot

The new deformation function is, so, a Gaussian distribution function with a variable  $\sigma$ . The result of the function implementation is shown in Figure (3.9).

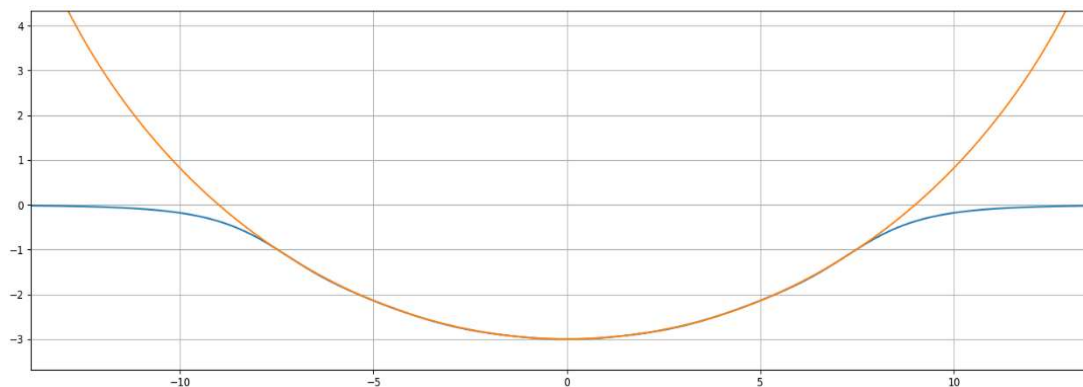


Figure 3.9 - Fitting between obtained profile and impactor profile

Once obtained the deformation profile, it was necessary to define a proper method to apply a progressive displacement through the successive layers. In order to allocate completely the 3 mm deformation in the layer structure, a qualitative stress-strain analysis was conducted over the whole cell and reported in Table (3.1).

Layer	Number of layers	Thickness [ $\mu\text{m}$ ]	Total thickness [ $\mu\text{m}$ ]	$\epsilon$	Final thickness [ $\mu\text{m}$ ]	Regrouped layers [ $\mu\text{m}$ ]
Cathode CC	21	20	420	0.257132	14.857	312.004
Anode CC	21	10	210	0.153839	8.4616	177.693
Anode AM	41	70	2870	0.599975	28.001	1148.07
Cathode AM	42	70	2940	0.129863	60.909	2558.2
Separator	42	20	840	0.899963	2.0007	84.031
Total			7280			4280

*Table 3 - Stress-strain evaluation for layer thicknesses*

The deformation coefficient  $\epsilon$  was used to define the thickness reduction of each layer due to compression. Strain allocation is assumed to be the same for all the layers of the same material.

Starting from a mapping vector of the X coordinates of the central points of the deformation, it was possible to write another vector reporting the coordinate after the application of the displacement (Figure (3.10)).

7.28	SEPARATOR	4.2800
7.26	SEPARATOR	4.2780
7.260	CATHODE_AM_NEG	4.2780
7.190	CATHODE_AM_NEG	4.2171
7.190	CATHODE_CC	4.2171
7.170	CATHODE_CC	4.2022
7.170	CATHODE_AM_POS	4.2022
7.100	CATHODE_AM_POS	4.1413
7.10	SEPARATOR	4.1413
7.080	SEPARATOR	4.1393
7.080	ANODE_AM_NEG	4.1393
7.010	ANODE_AM_NEG	4.1113
7.010	ANODE_CC	4.1113
7.000	ANODE_CC	4.1029
7.00	ANODE_AM_POS	4.1029
6.93	ANODE_AM_POS	4.0749
6.93	SEPARATOR	4.0749
6.910	SEPARATOR	4.0729
6.910	CATHODE_AM_NEG	4.0729
6.840	CATHODE_AM_NEG	4.0119
6.840	CATHODE_CC	4.0119
6.820	CATHODE_CC	3.9971

*Figure 3.10 - Vector mapping for deformed and pristine nodes positions*

Each layer is identified by two surfaces, each of which is represented by a X coordinate. The portion of layer thickness loss because of the deformation was kept in account by the following equation.

$$X_{def} = X_{orig} - (1 - \varepsilon) * th \quad (3.2)$$

Where

$X_{def}$ : new coordinate of the central point of the deformation

$X_{orig}$ : coordinate of the central point of the deformation before displacement

$\varepsilon$ : deformation coefficient obtained by the stress-strain analysis

$th$ : layer thickness

In order to grant a precise coincidence in terms of displacement among the layer succession, the lower coordinate of the upper layer is always equal to the upper coordinate of the lower layer.

Once calculated the new coordinate for all the layers, starting from the lowest one, the relative distance between two layers of the same material is derived, obtaining a value that will tune the amplitude of the deformation function.

The regular succession of the layers determined a uniform constant increase of the deformation amplitude, that was modelled with an equally spaced vector generated using the function `np.arange`. Two different successions are needed for the upper and lower surfaces (A, B), as reported in the following piece of code (Figure (3.11)).

```
A=np.arange(0.00153839800590551,3,0.144857060735766)
B=np.arange(-3.49467284971317E-10,3,0.144857060735766)

for i in range(len(Matrix)):
    if(math.sqrt((Matrix[i][2]-Y_c)**2+(Matrix[i][3]-X_c)**2)<=r**2):
        for j in range(len(Vector_up)):
            if Vector_up[j]== Matrix[i][1]:
                x=math.sqrt((Matrix[i][2]-Y_c)**2+(Matrix[i][3]-X_c)**2)
                Matrix[i][1]= Matrix[i][1]+func_Gauss_mod(x, 0, A[j],1)

for i in range(len(Matrix)):
    if(math.sqrt((Matrix[i][2]-Y_c)**2+(Matrix[i][3]-X_c)**2)<=r**2):
        for j in range(len(Vector_down)):
            if Vector_down[j]== Matrix[i][1]:
                x=math.sqrt((Matrix[i][2]-Y_c)**2+(Matrix[i][3]-X_c)**2)
                Matrix[i][1]= Matrix[i][1]+func_Gauss_mod(x, 0,1,B[j])
```

*Figure 3.11 - Python code for nodes displacement application*

Once stored the original coordinates data in a matrix, a for cycle was realized to check and find the nodes interested by the deformation. In particular, the position of each the node was controlled evaluating the linear distance from a previously defined center of the deformation ( $Y_c$ ,  $Z_c$ ) and comparing it to the desired radius of deformation ( $r$ ) as described by the sketch in Figure (3.12).

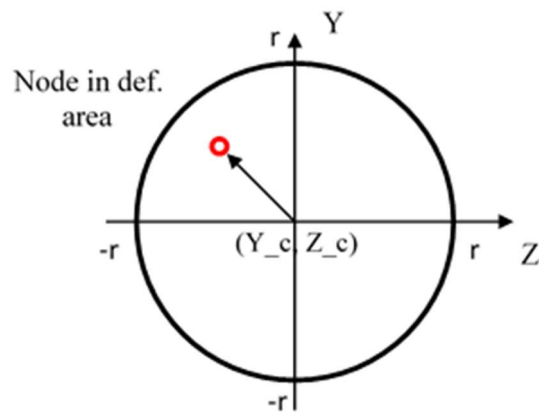


*Figure 3.12 - Identification criterion for nodes in deformed area*

In the selected area, a for cycle looks for the undeformed values of X coordinates stored in the Vector\_up and Vector\_down vectors and acts a replacement with the proper value coming from the deformation function. This procedure allowed to translate the 2D deformation profile in a 3D volume deformation.

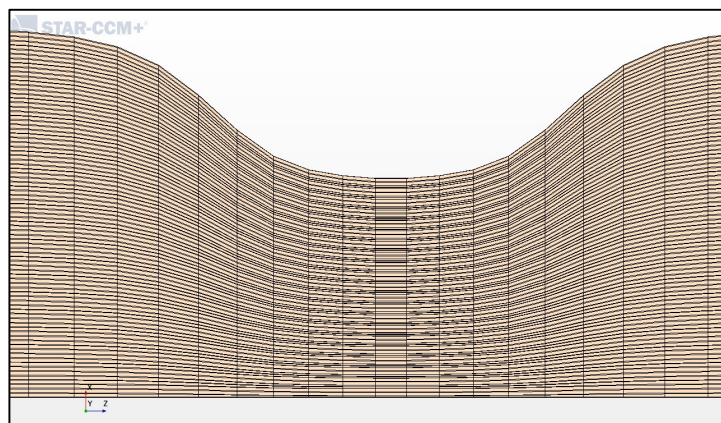


*Figure 3.13 - Section view of the obtained deformation*

Figure (3.13) represents the section view of the obtained deformed geometry. As observable, the layer thickness reduction gradually increases moving towards the center of deformation, as required from modelling pupropses.

The new coordinate matrix is then written into a new .inp file and ready to be loaded into the simulation software. The procedure was repeated for each region constituting the model geometry.

### 3.4 Regions and interface definition

When the mesh file is loaded, the software allows the automatic generation of a region. Regions are volume domains in space that are completely surrounded by boundaries. They are not necessarily contiguous, and are discretized by a conformal mesh consisting of connected faces, cells and vertices. The generation of different region for each group of layer will allow the proper physical characterization of each one.

The successive step consists in the definition of the contact areas between regions.

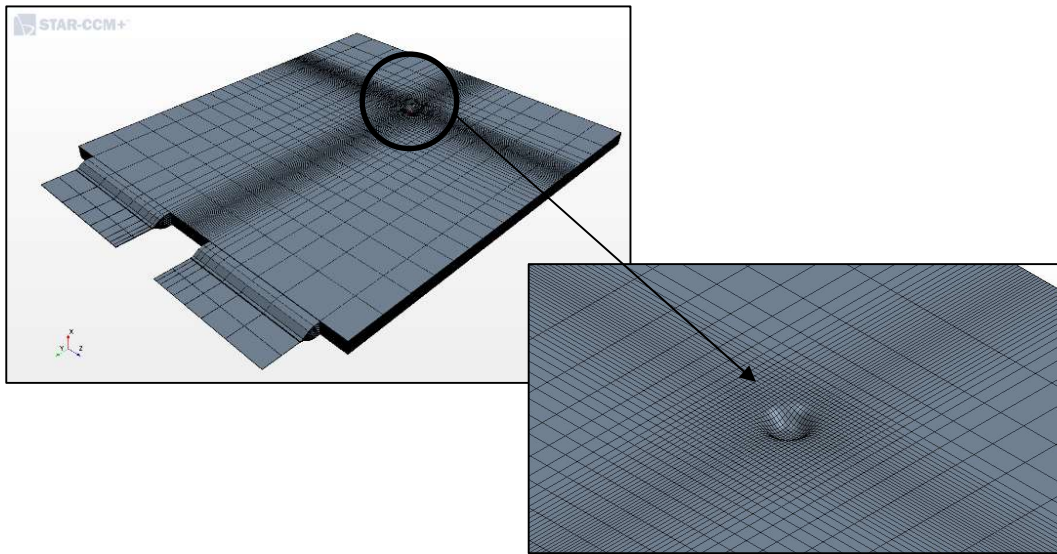


*Figure 3.14 - Deformed geometry and deformation area detailed view*

Interfaces provide a connection between boundaries during the simulation meshing setup and/or analysis process. They are always composed of boundary pairs, either in the same region or in different regions.

A total of 48 interfaces were created in the model, 8 for the internal coupling between layer groups, and the remaining ones for the tab extremities of the current collectors.

The contact-type interfaces realized for the layer contacts can be summed up as:

- Separator/Anode Active Material Interface
- Separator/Cathode Active Material Interface
- Anode Current Collector/Anode Active Material Interface
- Cathode Current Collector/Cathode Active Material Interface

Each of these sets requires two different interfaces, one for the upper and one for the lower surface of each layer.

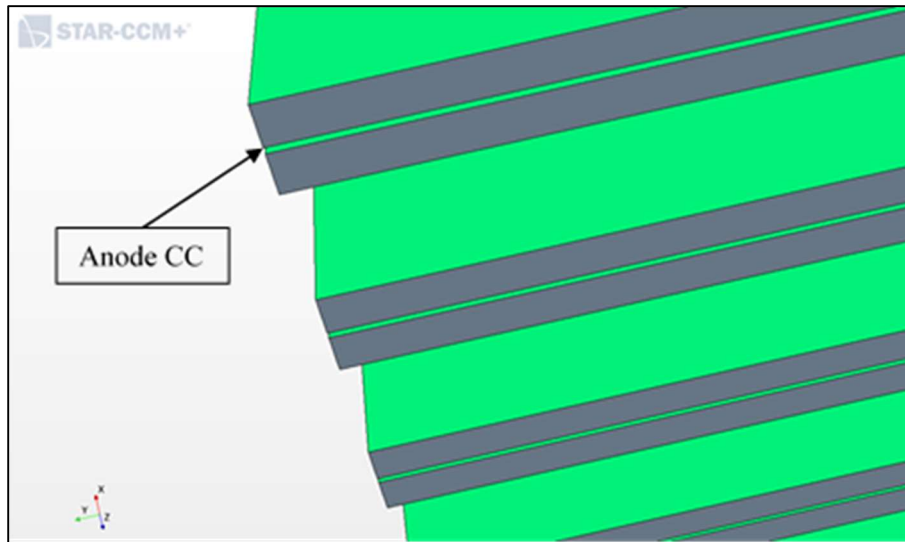


*Figure 3.15 - Interfaces between regions detail*

Figure (3.15) shows the interfaces for the Anode active material, the current collector is not highlighted in order to keep the visibility of the contact with the collector itself.

For geometric construction, the parts of the layers of the current collector constituting the tabs are separated by an empty space. The realization of internal interfaces is necessary to grant a proper modelling of the current transfer among layers. For each layer, the tab original geometry was divided in elementary parts until obtaining the flat extremity, the effective interfacing area (Figure (3.16)).

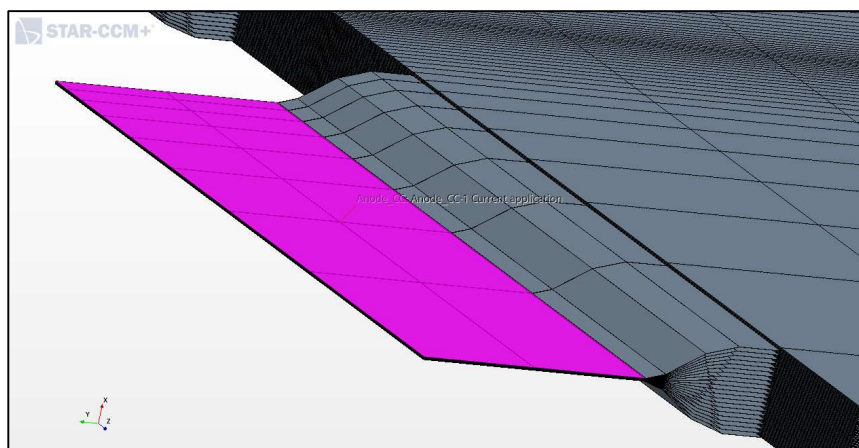


*Figure 3.16 - Interfaces between tabs layers*

### 3.5 Physics continua definition

The definition of interfaces represents the last step in the geometric set up of the model, while the introduction of the physical properties requires the choice of proper models able to describe and reproduce the thermal and electric phenomena inside the battery. The system under analysis is composed by different materials, with different characteristics; for this reason, it is necessary to define a specific physics continuum for each region. Although these differences, all the regions, except for the separator, share a common selection of models.

The software interface showed in Figure (3.17) allows to choose among different sets of models. Each of these unlocks sub-models on the basis of dependances criterions (e.g. electromagnetism unlocks ohmic heating model) and suggests automatic side-models that can be not compulsorily activated.

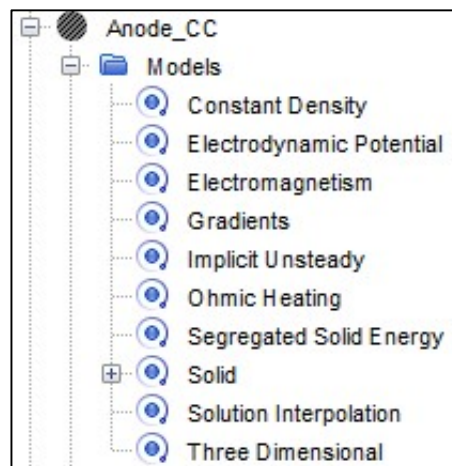


Figure 3.17 - StarCCM+ interface panel for models selection

- **Constant Density:** based on the assumption that density of the solid material is invariant in time in the continuum [20].

- **Electromagnetism:** introduces equations for analysing the behaviour of continua in response to electromagnetic fields. The main equations are the Maxwell's equations and conservation of electric charge equations.

Indicating with  $\rho$  the electric charge density,  $J$  the electric current density,  $E$  the electric field,  $D$  the electric flux density,  $H$  the magnetic field, and  $B$  the magnetic flux density, the Maxwell's equations result [20]:

$$\frac{\partial B}{\partial t} + \nabla \times E = 0 \quad (3.3)$$

$$\frac{\partial D}{\partial t} - \nabla \times H = -J \quad (3.4)$$

$$\nabla \cdot D = \rho \quad (3.5)$$

$$\nabla \cdot B = 0 \quad (3.6)$$

The relationship between the electric current density  $J$  and the electric field  $E$  is described by the generalized Ohm's law:

$$J = \sigma E \quad (3.7)$$

The coefficient  $\sigma$  represents the conductivity of the material, its behaviour in response to electric currents. Mathematically it represents the inverse of the resistivity, resulting:

$$\sigma = \frac{1}{\rho} = \frac{l}{R \cdot A} \quad (3.8)$$

Where

$l$ : layer thickness,

$R$ : internal resistance,

$A$ : layer surface interested in conductive phenomena.

The conservation of electric charge is expressed like:

$$\frac{\partial \rho}{\partial t} + \nabla \cdot J = 0 \quad (3.8)$$

- **Electrodynamic potential**: provides equations for the computation of the electric potential. This model defines the discretized equation that the solver calculates in the finite volumes defined [20].

$$\oint_A \sigma \nabla \phi \cdot da - \oint_A \sigma \frac{\partial A}{\partial t} \cdot da = - \oint_A \sigma \rho \cdot da \quad (3.9)$$

- **Joule heating**: this model allows to describe the relationship between electric currents and temperature changes in conducting materials. The heat generation due to the flow of current inside a resistive material is ruled by the Joule's law:

$$Q = JE \quad (3.10)$$

considering the electric current density  $J$  and the electric field  $E$  for a unitary volume [20].

- **Segregated solid energy**: defines the energy transport law within a solid as

$$\frac{d}{dt} \oint_V \rho C_p T dV + \oint_A \rho C_p T V_S \cdot da = - \oint_A q'' \cdot da + \oint_V S_u dV \quad (3.11)$$

where:

-  $\rho$ : solid density,

- $C_p$ : specific heat,
  - $T$ : temperature,
  - $q''$ : heat flux vector,
  - $V_s$ : solid convective velocity,
  - $S_u$ : user-defined volumetric heat source within the solid [20].
  - **Solid**: regarding the phase of the materials involved, the choice is surely the solid option.
- On the basis of the selected models, different physical properties are required for each continuum. Values employed were chosen on the basis of the previously realized models and are summed up in Table (4).

Region	Material	Density [Kg/m <sup>3</sup> ]	Electrical Conductivity [S/m]	Thermal Conductivity [W/(m*K)]	Specific heat [J/(Kg*K)]
Anode CC	Cu	8940	1.49E7	398	386
Cathode CC	Al	2702	9.45E6	237	903
Anode AM	Graphite	2100	Field function	1.2	1131
Cathode AM	NMC	2100	Field function	1.2	1131
Separator	PP/PE	2100	-	1.2	1131

*Table 4 - Materials physical properties*

Except for the electrical conductivity of the active materials of the electrodes, all the material properties are assumed to be constant in time. The need of a field function definition for the active materials is necessary in terms of modelling of the variable internal resistance of these material with respect to state of charge.

- **Implicit unsteady**: physics modelling requires a time specification for simulation. This choice will define how the solver computes the solution during the simulation process. There are essentially two different time analysis: implicit and explicit. Implicit time analysis grants the global equilibrium of the system at each time increment; this means that the solution must converge at each time interval before moving to the next step. Once equilibrium is reached, the solver is able to compute the desired variables for the finite elements. When dealing with this time approach it is possible to set and modify the time step for the simulation and the number of maximum iterations for each step.

$$G(Y(t), Y(t + \Delta t)) = 0 \quad (3.12)$$

This equation shows how the implicit method employs both the current state  $Y(t)$ , and the

state at the next time step  $Y(t + \Delta t)$ , to find  $Y(t + \Delta t)$  exploiting the equilibrium condition. Explicit time analysis, instead doesn't require the reach of an equilibrium during the step, but the time increment is chosen and ruled by the solver, usually as a really small value. The main factor that determines the choice between the two criteria is the time scale of the observed phenomenon. In the case of study, the implicit analysis is chosen because the simulated phenomenon takes place in hundreds of seconds, and the possibility to select an optimal time step makes the effective simulation time comparable to the real timescale of the phenomenon. Moreover, the implicit approach results a better choice for phenomena in which the dynamics is really slow, so, the perturbations that occur at each time step are minimal.

$$Y(t + \Delta t) = F(Y(t)) \quad (3.13)$$

As well as for the equation for the implicit time approach, it is possible to define an equation for the explicit time approach, where the state after the time step  $Y(t + \Delta t)$  is only function of the current state  $Y(t)$ .

### 3.6 User field function definition for equivalent circuit modelling

As explained in chapter 2, the equivalent circuit that models the electrical behavior of the cell must be replicated in the FEM model.

In StarCCM+ it is possible to define user field functions. These allow to access fields (scalar or vector data that are evaluated at cells, vertices, or boundary faces) or to specify boundary and region values as well as defining initial conditions.

In particular, the equivalent circuit replication requires the definition of field functions for:

- open circuit voltage (OCV) as a function of state of charge (SoC),
- internal polarization resistance of electrodes active materials as a function of SoC.

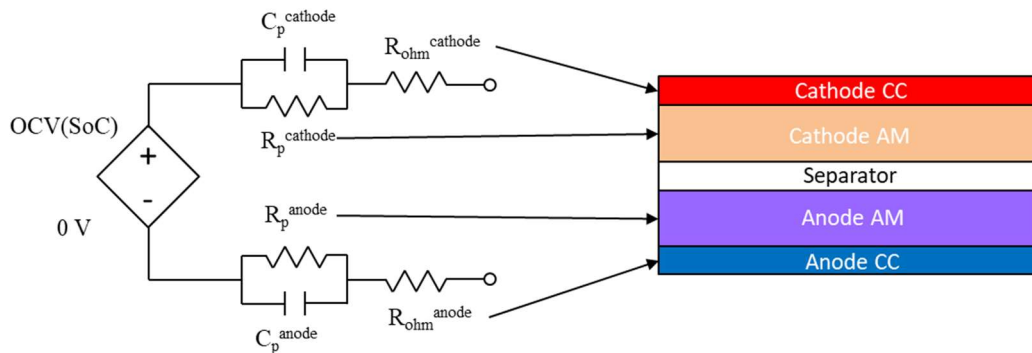


Figure 3.18 - Correspondence between layer arrangement and equivalent circuit

Figure (3.18) shows how a correspondence was created between the equivalent circuit and the layer arrangements.

The OCV profile has not constant value in time, so, it must be properly set on the basis of the current SoC. Reminding SoC definition as Equation (2.6), the same equation must be defined in a field function able to update the value of SoC at each time step, acting the time discretization. This function requires to access the value of SoC at the previous time instant to calculate the next one. In StarCCM+ it is possible to define a monitor tool, that is able to store the value of a function at a certain time-step. In particular, the monitor samples the value with the frequency of a time-step and then, enabling the option of a sliding window, the tool automatically overwrites the new value of the function to the old one.

Values of electric current are expressed in STAR-CCM+ in terms of electric current density vector field,  $J$  [ $A/m^2$ ], so the equation for the state of charge must be built considering a component or the magnitude of this quantity.

$$SoC[k + 1] = SoC[k] - \frac{\Delta t}{Q} J_x[k] A_{AM} \quad (3.14)$$

The geometry of the system makes the electric current across the active materials flowing mainly along the x direction (perpendicular to main surfaces), with strongly negligible values for the planar components. For this reason, the value of current employed in the calculus is selected as the x component of electric current density vector, that, must be multiplied for the planar surface of the active material  $A_{AM}$ .

In a similar way the relative state of charge equation is implemented in another field function

$$SoC_{rel}[k + 1] = SoC[k] - \eta \frac{\Delta t}{Q} J_x[k] A_{AM} \quad (3.15)$$

The SoC value calculated at each time step interacts with another field function that reproduces the OCV-SoC curve, so, for a certain value of SoC, defines a precise value of OCV that is set on the interfacing surface between the Cathode AM and the separator layer.

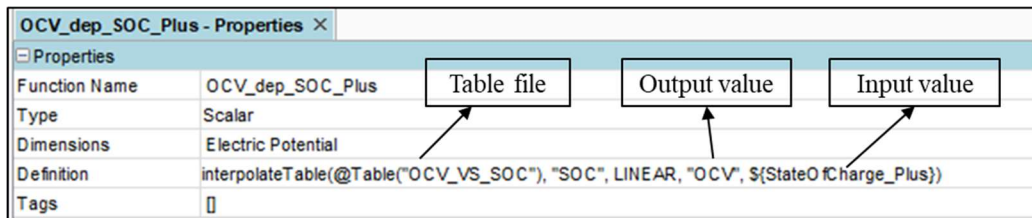


Figure 3.19 - OCV-VS-SoC interpolation function in StarCCM+

The OCV curve is loaded in the model as a table file, and, through a linear interpolation, the set of points is translated into a continuous function (Figure (3.19)).

In this way the SoC controlled generator in figure is reproduced in the layer arrangements, with OCV value between Cathode AM and separator and a constant 0V profile at the interface between Anode AM and separator.

In a similar way, a function defining the polarization resistance in the active materials as a function of SoC is implemented. Reminding Equation (3.8), the electrical conductivity of a material is a physical quantity that contains information about the resistivity of the material itself. Exploiting this principle, the resistance is modelled with a variable electrical conductivity of the active materials directly in the continuum properties of the model. The following field function is, so, set as value of  $\sigma$  in the material properties:

$$\begin{aligned} \text{Sigma\_AM} &= \frac{\text{layer thickness}}{\text{Internal resistance} \cdot \text{layer surface}} \\ &= \frac{1.59E - 3}{\text{Internal\_resistance}} \end{aligned} \quad (3.16)$$

Knowing the geometrical properties of the layer of interest, the electrical conductivity is only function of the internal resistance.

This modelling strategy allows the definition of a simple resistive contribution in order to compute the conductivity, so, the RC parallel defining the impedance in the equivalent circuit cannot be exactly replicated in the FEM model, because of the impossibility of distinguishing capacitive contributions.

For this reason, a mathematical manipulation of the resistance function is necessary to reproduce the capacitive effect.

The presence of a capacitance is necessary to reproduce the gradual increase of the resistance in the first stages of a discharge. This assumption makes the value start from a null contribution and reaching a steady state value after a certain transient. The length, in terms of time, of this transient is ruled by the time constant  $\tau$ .

As observable in Figure (3.20-a), the steady value of  $2\text{m}\Omega$  is reached after a certain amount of time that is about  $5\tau$ , with a time constant of 60s, so in 300s (Figure (3.20-b)). After this point of the simulation, the resistance depends only on its steady value.

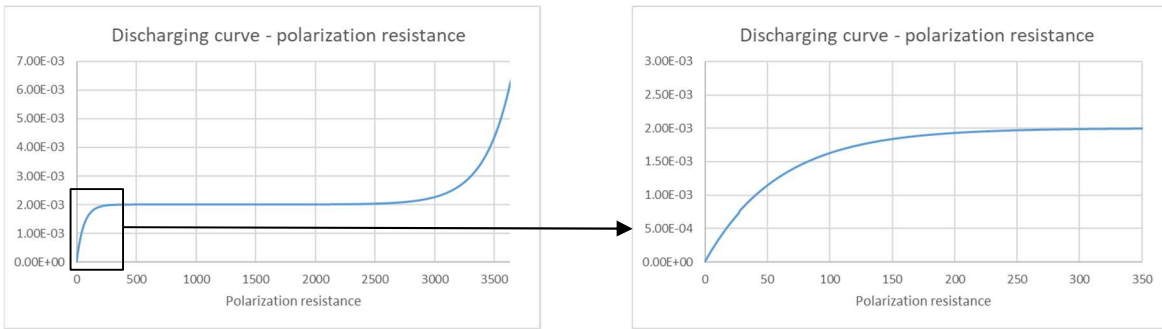


Figure 3.20 - Polarization resistance curve during discharge (a) with transient detail (b)

The following equation is so defined in a proper user field function that updates the value at each time-step in the same mode explained for the SoC function.

$$R_p[k + 1] = R_p[k]e^{-\frac{\Delta t}{\tau}} + (1 - R_{p_{steady}}[k])e^{-\frac{\Delta t}{\tau}} \quad (3.17)$$

The value of  $R_{p_{steady}}$  is read by the function entering another field function where the resistance curve is loaded through a table file.

This time, the input value for the definition of the output of the interpolating function is the relative SoC, reminding the dependence of internal resistance on the applied current explained in chapter 2.

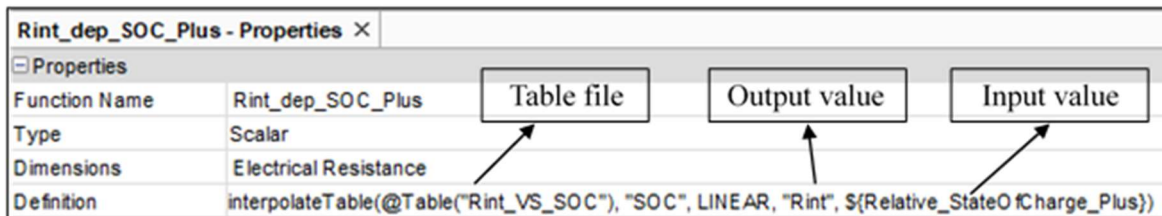


Figure 3.21 -  $R_{int}$ -VS-SoC interpolation function in StarCCM+

### 3.7 Encountered divergence problem during simulation

Once completed the model set-up with the deformed mesh geometry, preliminary simulations were launched in order to verify a coherent behavior of the simulation process. A reference simulation was previously conducted building another model with pristine mesh geometry, set up following the same explained procedure in order to check the eventual occurrence of defects due to the new refinement of the mesh.

Imposing constant current values to the current application surfaces defined on the cell tabs, it is possible to simulate a discharging process of the battery starting from 100% state of charge. Current values were set at 160A for the anode tab and -160A for cathode tab, so, a 4C discharge is simulated (Figure (3.22)).

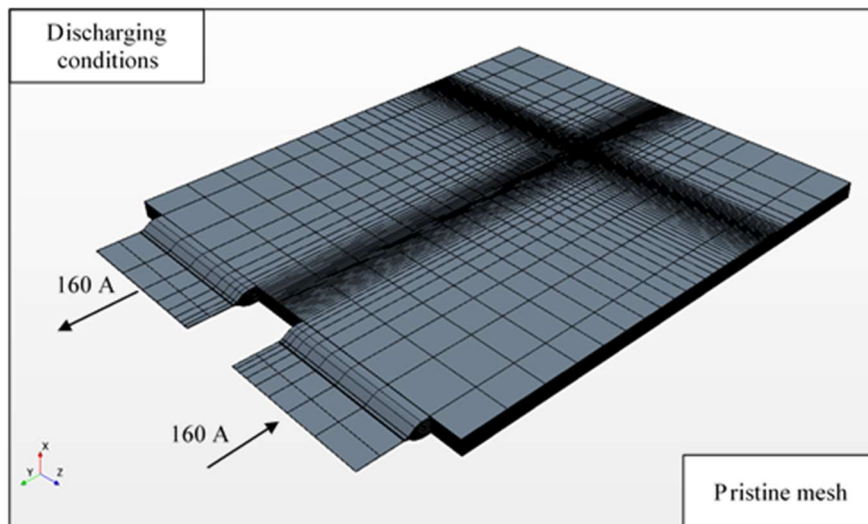
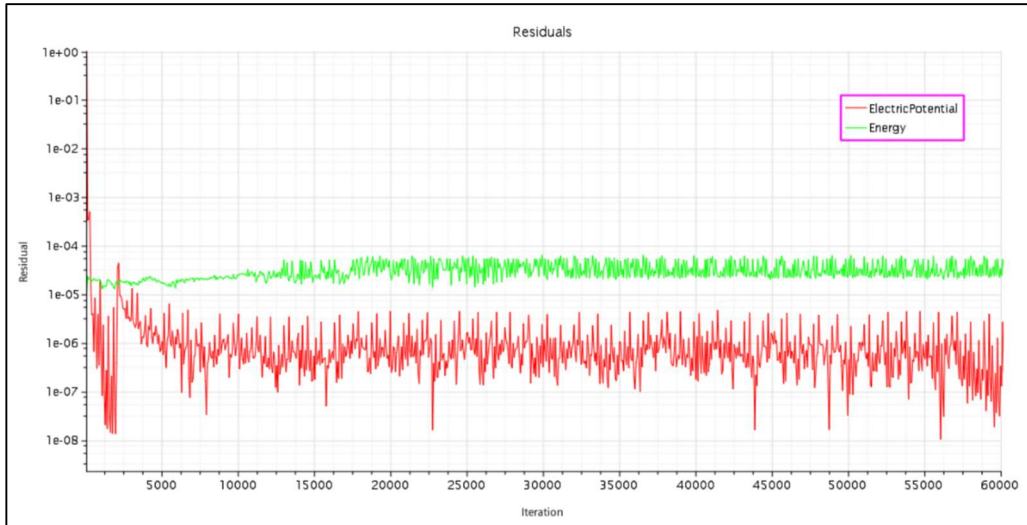


Figure 3.22 - Pristine mesh initial conditions for discharge process

The results of simulation were coherent with respect to simulation conducted on meshes with different refinement, and it was possible to understand a suitable range for time step to be employed in simulation. In particular, a time step of 0.1s was necessary at least for the first 2000 iterations (20s of physical time), due to a small voltage transient due to current application, while from this point on, a step of 0.5s determined a nice convergence behavior, with the possibility of rising the time step up to 1s (Figure (3.23)).



*Figure 3.23 - Residual plot in convergence conditions*

Once obtained a reference result, the same simulation conditions in terms of applied current and solver settings were employed in a simulation with deformed mesh geometry (Figure (3.24)).

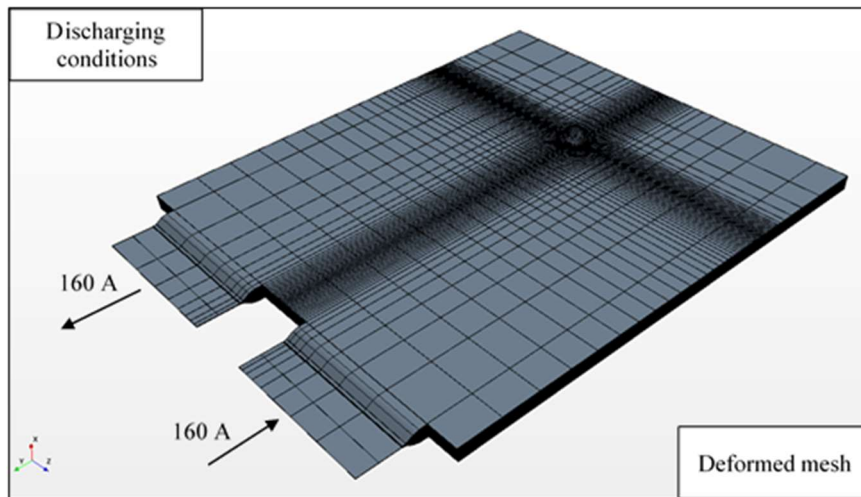


*Figure 3.24 - Deformed mesh initial conditions for discharge process*

The simulation stopped at a physical time of 21 seconds due to a floating point exception error, displayed in a warning window. Observing the behaviour of residuals it is possible to highlight how a good convergence trend was reached at about 1400 iterations, whit residuals values oscillating between  $10E-5$  -  $10E-7$ .

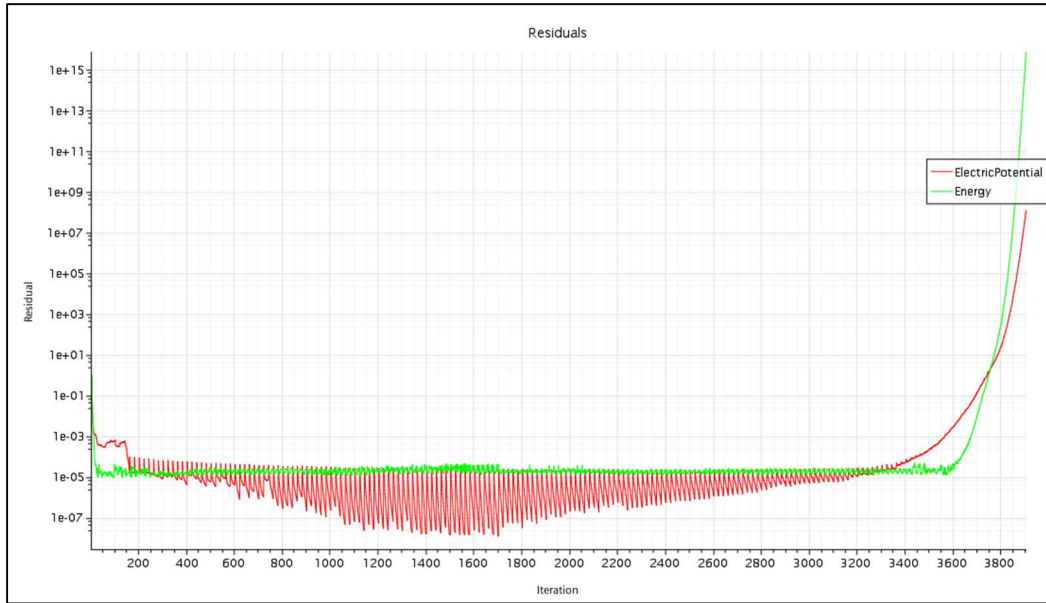


*Figure 3.25 - Residuals plots in divergence conditions*

After this apparent convergence interval, the curves start to diverge reaching values that obviously lead to a simulation interruption as showed in Figure (3.25). The different results of the two simulations means that the cause of the divergence is surely related to the induced deformation. In the following paragraph the strategy employed to identify the cause of the divergence will be explained.

### 3.7.1 Strategy for the identification of the cause of the divergence

Due to the complexity of the system under analysis, the cause of the divergence must be researched in many possible features of the model. For this reason, a strategy for the investigation was defined, in order to exclude, gradually, part of the possible causes at each step. The main areas of investigation are summed up in the following map (Figure (3.26)), and will be explained in their order of execution.

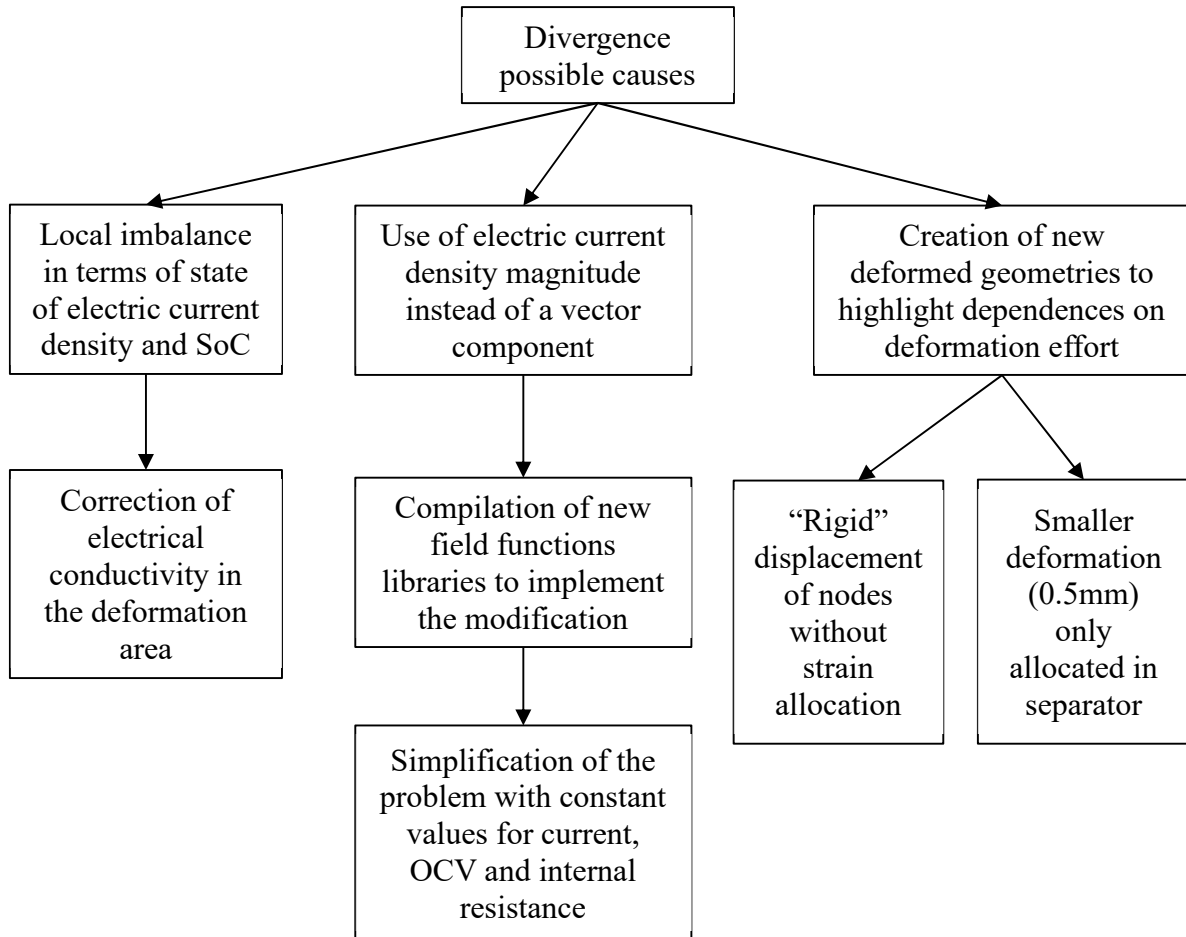


Figure 3.26 - Strategy for the identification of divergence cause

### 3.7.2 Local imbalance of model variables at divergence and corrections

The starting point for the analysis of the simulation anomaly is the observation of the most important variables computed by the solver in order to look for eventual unwanted trends in proximity or inside the area where the deformation is applied in a time instant close to the divergence. The main values to be checked are the electric current density vector field, the absolute and relative state of charge and the electric potential in all the regions of the model. A surely incoherent behavior to be fixed is observable in the relative SoC at the divergence instant.

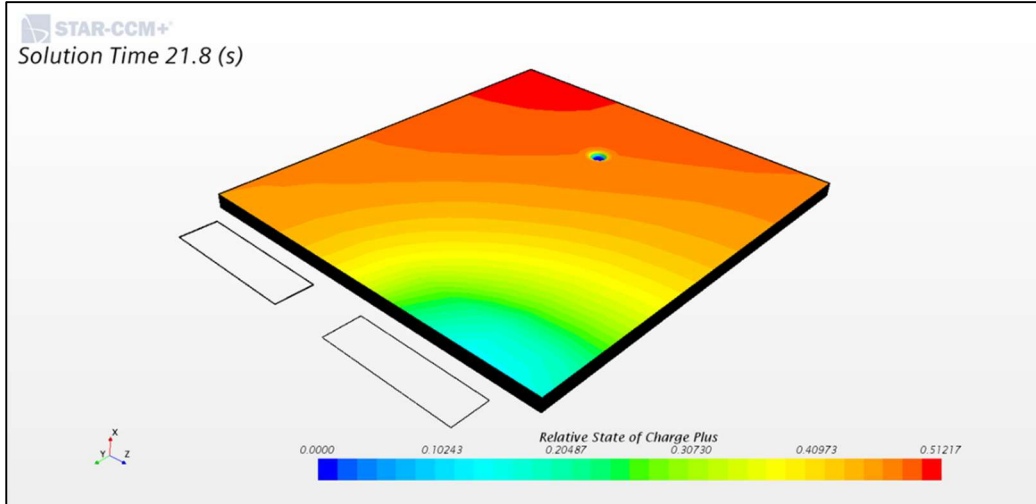


Figure 3.27 - SoC local imbalance in deformed area

Reminding the equation for the relative state of charge in discrete time:

$$SoC_{rel}[k + 1] = SoC_{rel}[k] - \frac{\Delta t}{Q} \eta[k] I[k] \quad (3.18)$$

the presence of an area with relative SoC equal to 0 (Figure (3.27)) is to account to a non-uniform distribution in terms of current. Looking at the vector scene for the electric current density, in fact, peak values are identified in the area of deformation.

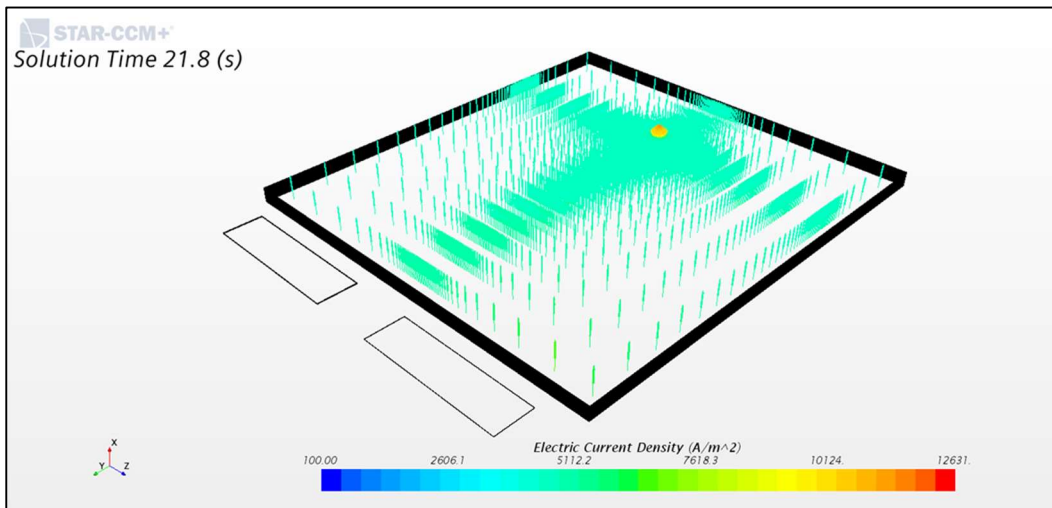


Figure 3.28 - ECD local imbalance in deformed area

This peak current spot is caused by a wrong definition of the electrical conductivity in the deformed area (Figure (3.28)). The simulation was run considering a uniform distribution of the parameter in the active material regions, but, the deformation of the mesh and the consequent layer thickness reduction makes this assumption incompatible with the current model configurations. Reminding eq. (3.16), conductivity ( $\sigma$ ) depends on the layer

thickness, so, the function definition must be corrected in the area interested by the deformation.

Reminding the deformation coefficients reported in Table (2), the final thicknesses of active materials in the central point of the deformation can be summed up as:

$$\begin{aligned} th_{AnodeAMdef} &= 0.4 * th_{AnodeAMnom}, th_{CathodeAMdef} \\ &= 0.87 * th_{CathodeAMnom} \end{aligned} \quad (3.19)$$

Knowing these maximum value of thickness reduction it was possible to obtain a qualitative law for the definition of  $\sigma$  in the deformed area, in order to obtain a coherent value of electrical conductivity dependent on the local thickness.

Assuming a linear increment of layer thickness moving from the center of deformation to the border radius, the following definition was obtained (the graph for anode  $\sigma$  is showed in Figure (3.29)).

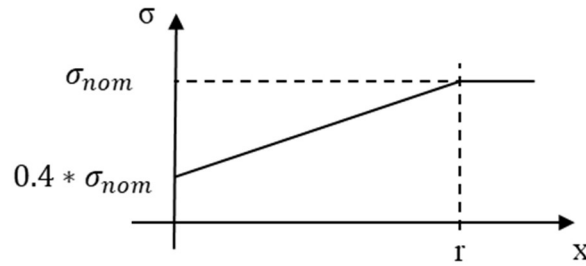


*Figure 3.29 - Sigma function correction graph*

Where  $\sigma_{nom}$  represents the value of the standard electrical conductivity and  $r$  the radius of deformation. In this way, the correction is made only inside the deformation circle, granting, instead, the nominal value of conductivity in the rest of the cell.

Applying this modification, the values of electric current density and SoC assumed a coherent behavior also in proximity of the divergence instant, but the correction did not solve the divergence problem.

### 3.7.2 Simplification of solving conditions

Due to the complexity of the system in terms of variable of interest and definition of starting condition, as well as physical properties of the material, a trial and error strategy to find the divergence cause was not suitable. For this reason, different simulations were conducted excluding partially and gradually some of the variables calculated by the solver and reporting the effect of the problem relaxation in a table, in order to isolate the variable affecting the solution inconsistency.

As a first step, new functions for the definition of relative and absolute state of charge were created, substituting the vectorial x-component of the electric current density with the magnitude value of the vector itself. This was possible writing and compiling a new user library to be loaded in the software environment and provide the correspondent field function. This custom function allows to define constant values for the current employed in the calculation of state of charge; these values are properly chosen on the basis of the simplification of the problem to be achieved.

The following Table (5), sums up simulation attempts conducted with the exclusion of some initial conditions. In particular, the main input data for the model can be identified as:

- current applied on tabs (loading condition);
- voltage profile at separator/active material interfaces (OCV values);
- electrical conductivity law for active materials;
- value of electric current density employed for SoC calculation.

Input parameters	Attempt 1	Attempt 2	Attempt 3	Attempt 4
Current on tabs	0 A	0 A	160 A	160 A
OCV profile	OCV_VS_SOC	4,2	OCV_VS_SOC	OCV_VS_SOC
Electrical conductivity AM	Field function	Field function	Field function	Field function
ECD value	ECD_MAGN	ECD_MAGN	ECD_MAGN	0
Simulation output	CONVERGENCE	CONVERGENCE	DIVERGENCE	DIVERGENCE

*Table 5 - Model simplification simulation part 1*

Attempt 1 and 2 were conducted removing the loading current on the cell, so, for a null value of current on anode and cathode tabs. The difference between the two cases consisted in the application of two different values of voltage at the interfaces between separator and active materials; both simulations led to a non-divergent behaviour of the model, highlighting how, the cause of the divergence itself derived from a flow of current into the

deformed area of the cell. The third column of the table represents the nominal desired working conditions of the model, and, as explained in section 3.7, these input conditions led to the divergence problem under investigation.

The successive two attempts aimed to exclude computational errors of the solver regarding the calculus of SoC and  $SoC_{rel}$ . Reminding Equation (3.14), electric current density rules the evolution of SoC in time, so, posing a null value of ECD would determine a constant value of SoC during simulation, as well as, in attempt 5, a constant value of ECD would determine a linear reduction of SoC.

Input parameters	Attempt 5	Attempt 6	Attempt 7	Attempt 8
Current on tabs	160 A	160 A	160 A	160 A
OCV profile	OCV_VS_SOC	OCV_VS_SOC	OCV_VS_SOC	OCV_VS_SOC
Electrical conductivity AM	Field function	Constant	0 in deformed area	Constant in deformed area
ECD value	160	ECD_MAGN	ECD_MAGN	0
Simulation output	DIVERGENCE	CONVERGENCE	DIVERGENCE	DIVERGENCE

*Table 6 - Model simplification simulation part 2*

Observing divergence also in the just explained attempts led to the assumption of the independence of this unwanted behaviour on SoC calculus, so, the successive parameter to be evaluated was electrical conductivity of active materials.

Attempt 6 was conducted imposing a constant value of electrical conductivity in all active material elements of the cell. From a modelling point of view, this assumption is not true, because polarization resistance curve explained in section 3.6 is just modelled implementing a SoC variable value of electrical conductivity. In terms of debugging of the system, this simulation revealed an interesting result, in fact, a convergence trend of simulation was reached. This result led to a further evaluation conducted in attempts 7 and 8. In the first one, electrical conductivity was set to 0 in the deformed area, so, making AM acting like an insulator in a desired area; in this way ECD is absent due to a null value of  $\sigma$ . Although this simplification, the divergence of simulation was still present.

Two more attempts were conducted in the same condition of case 3, but applying separately the current load just on one of the two tabs. Applying current only on cathode tab, it was possible to complete the simulation, while the application on the anode tab led to divergence. This observation, together with results coming from lastly explained attempts

highlighted the possibility of an imbalance in terms of current in the deformed area, due to a non-uniform layer thickness reduction between anode and cathode. Although this aspect was corrected as explained in section 3.7.2, the only solution to exclude completely this possibility was to realize different deformed mesh geometries.

### 3.7.3 Realization of alternative deformed geometries

Reminding that, the only difference between the correctly working model with non-deformed mesh and the model built-up with the deformed mesh, is represented by the nodes shifting in the deformation area, a further evaluation of the eventual effects of this mathematical manipulation of the mesh geometry was considered necessary.

The first alternative geometry realized, aimed to exclude the effects of thickness reduction in simulation, so, the displacement was applied to nodes of deformed area, considering all deformation coefficients  $\epsilon$  equal to 0. In this way, the thickness of layers is not modified at all and the resulting geometry is obtained with a rigid displacement of nodes, with no strain allocation.

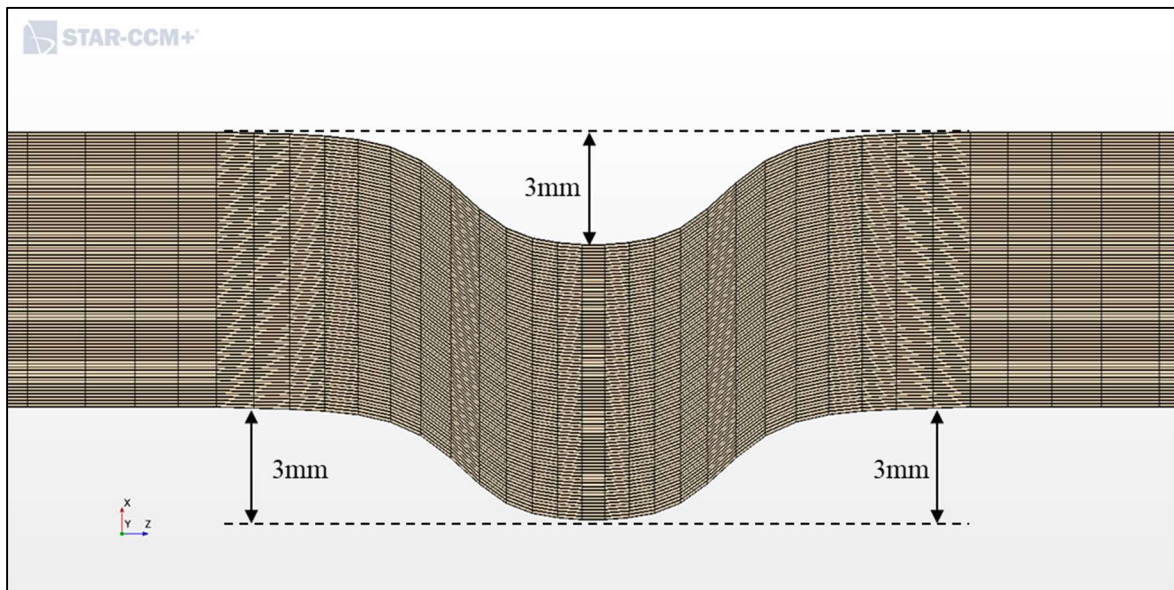


*Figure 3.30 - Section view of deformed geometry with rigid nodes displacement*

As observable in Figure (3.30), the absence of thickness reduction induces a rigid shifting of nodes position, so, the deformed volume is just moved to the bottom part of the cell.

Running the simulation of a model set-up with this deformed geometry and considering the input conditions of attempt 3 (Table (5)), the same divergence problem was encountered exactly at the same time instant. This result excluded also the influence of an eventual imbalance of currents due to deformation, so, the only remaining possible cause of

divergence could be related to geometrical conditions of the obtained deformed cells of the mesh.

The displacement of nodes employed to realize the deformation induces the creation of some angles between cells with respect to a flat geometry. In StarCCM+, a proper parameter for the identification of these inclinations is the skewness angle.

This skewness measure is designed to reflect whether the cells on either side of a face are formed in such a way as to permit diffusion of quantities without these quantities becoming unbounded [20]. To understand this measure, consider the following two-dimensional diagram, in Figure (3.31), of a face and the cell centroids on either side of the face:

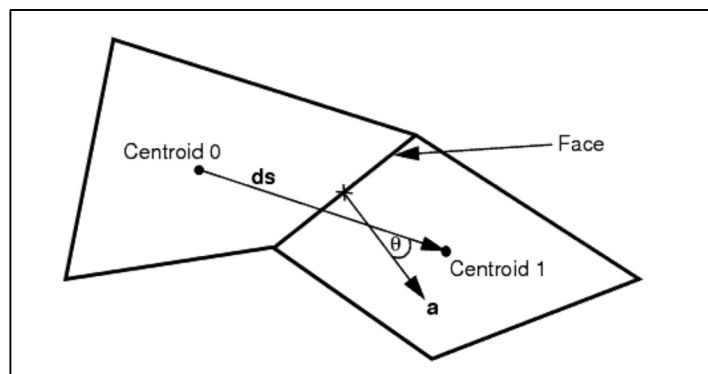


*Figure 3.31 - Skewness angle representation [20]*

The skewness angle  $\theta$  is the angle between the face area vector  $a$  (face normal) and the vector connecting the two cell centroids,  $ds$ . An angle of zero indicates a perfectly orthogonal mesh.

Referring to the software user guide, a certain effort of skewness angle could determine convergence issue during simulation, so, in order to reduce the skewness factor of the interested cells, another deformed geometry was realized.

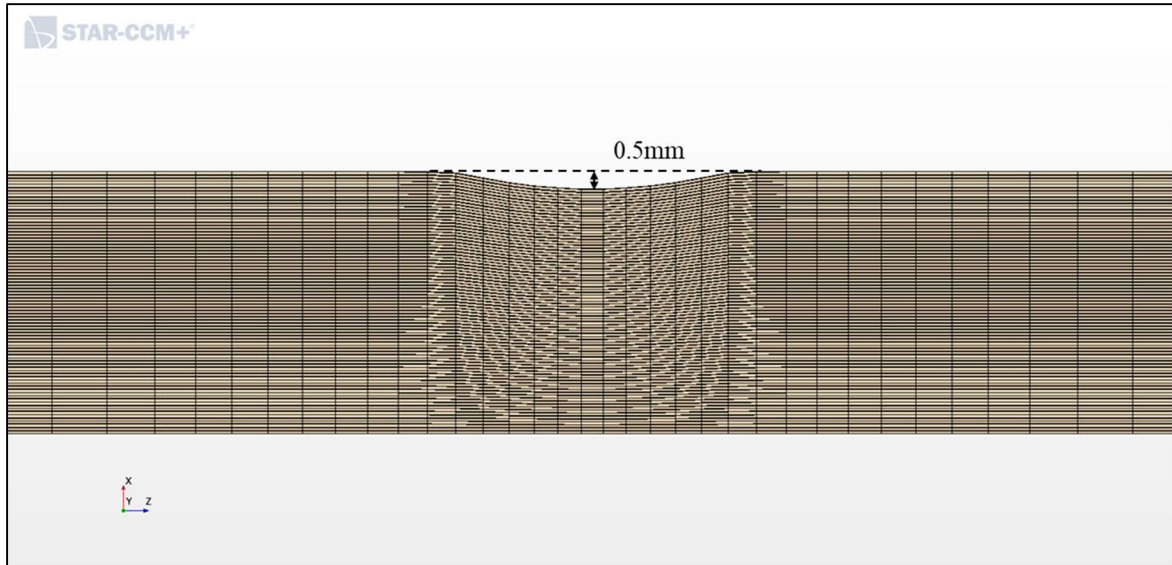


*Figure 3.32 - Section view of deformed geometry with 0.5mm strain allocation*

Looking at the cross section of the new geometry in Figure (3.32), the displacement allocated into the cell was reduced to 0.5mm from the original 3mm depth. Moreover, all the strain allocation was inducted in separator layers, keeping all other materials in a non-deformed condition. This modification effectively reduced the effort of skewness angle in the deformation area, but, running a new simulation even with this simplified geometry, led to the same divergence problem. For this reason, simulations of cell in deformed condition were conducted on a pristine geometry with a local modification of internal parameters, in order to reproduce the wanted behaviours, as explained in the following chapter.

# CHAPTER 4

## 4. Analysis of test data and simulation

In this chapter, results coming from the experimental investigation, already shown in section 2.3 will be analyzed, with a particular focus on the causes of voltage curve variations between pristine and deformed cell measurements. The identification of an internal resistance reduction is then reported in the FEM model for simulations. A comparison between measured and simulated curve is presented.

### 4.1 Analysis of results from experimental investigation

As anticipated in section 2.3, tests conducted on deformed and pristine cells for electrical cycling between 20 and 30% SoC, revealed differences in terms of voltage curves. In Figure (4.1) a cycle of charge and discharge for 1C rate is showed.

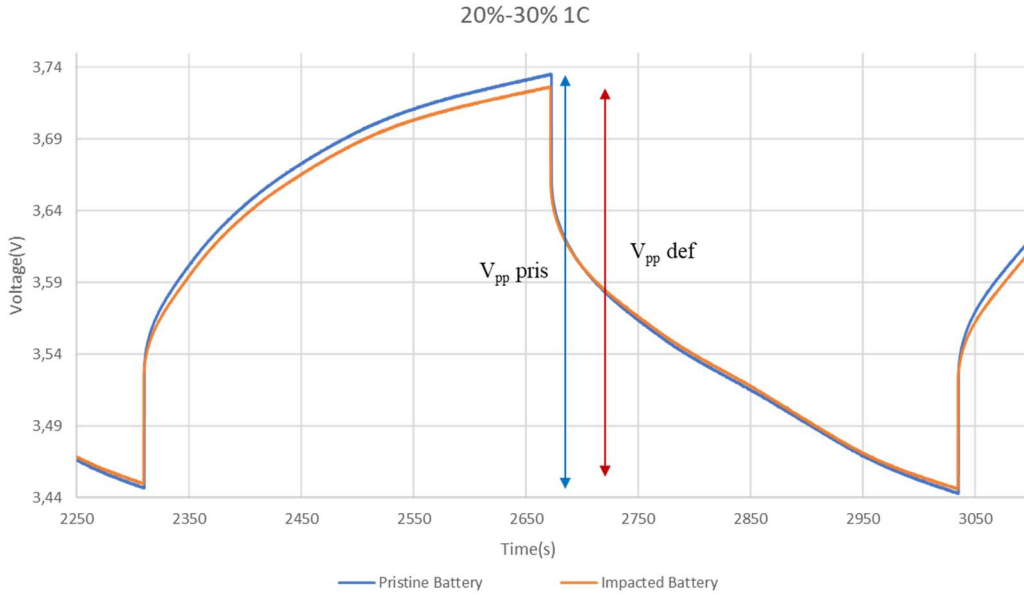


Figure 4.1 - Detail of 1C cycling 20-30% for  $V_{pp}$  evaluation

Naming respectively  $V_{pp}$  pris and  $V_{pp}$  def, the voltage value measured between the peak value at 30%SoC and the bottom value at 20% SoC for the compared curves, it can be noticed that  $V_{pp}$  def <  $V_{pp}$  pris. The difference between these two values results 0.02V.

Reminding 1D circuit model equation, terminal voltage measurable at the tabs of the cell in charging phase can be calculated as:

$$V(t) = OCV(SoC) - I(R_p(SoC) + R_{ohm}) = OCV(SoC) + I(R_{tot}) \quad (4.1)$$

As a simplification, the value of resistance is considered a unique contribution in this analysis and denoted as  $R_{tot}$ . Considering that the two curves share the same SoC at the same time instant, their OCV value can be assumed equal; this means that the differences in terms of  $V(t)$  between the curves depend only on the contribution of the voltage drop caused by the current flow. The peak voltage difference can be expressed as:

$$\begin{aligned}
V_{p_{pris}} - V_{p_{def}} &= \Delta V_{cycling} \\
&= OCV_{pris} + I(R_{tot_{pris}}) - OCV_{def} - I(R_{tot_{def}}) \\
V_{p_{pris}} - V_{p_{def}} &= \Delta V_{cycling} = I(R_{tot_{pris}}) - I(R_{tot_{def}}) \\
&= I(R_{tot_{pris}} - R_{tot_{def}})
\end{aligned} \tag{4.2}$$

Defining this equation, considering the known value of current equal to 40A, and the  $\Delta V_{cycling}$  equal to half of the  $V_{pp}$  variation, the total internal resistance variation can be calculated as:

$$\begin{aligned}
(R_{tot_{pris}} - R_{tot_{def}}) &= \frac{\Delta V_{cycling}}{I} = \frac{\Delta V_{pp}}{2I} = \frac{0.02}{2 * 40} = 0.00025\Omega \\
&= 0.25m\Omega
\end{aligned} \tag{4.3}$$

This result highlights a total internal resistance reduction due to the deformation, and, considering the SoC range under analysis, this variation represents about the 10% of the value of resistance for the studied part of the charge/discharge curve.

Knowing the effort of resistance reduction, a further validation of the obtained result can be found in the evaluation of voltage curve differences at higher C-rates. In particular, the voltage variation is expected to grow proportionally to the applied current.

$$\Delta V_p = I_{app} * \Delta R_{tot} \tag{4.4}$$

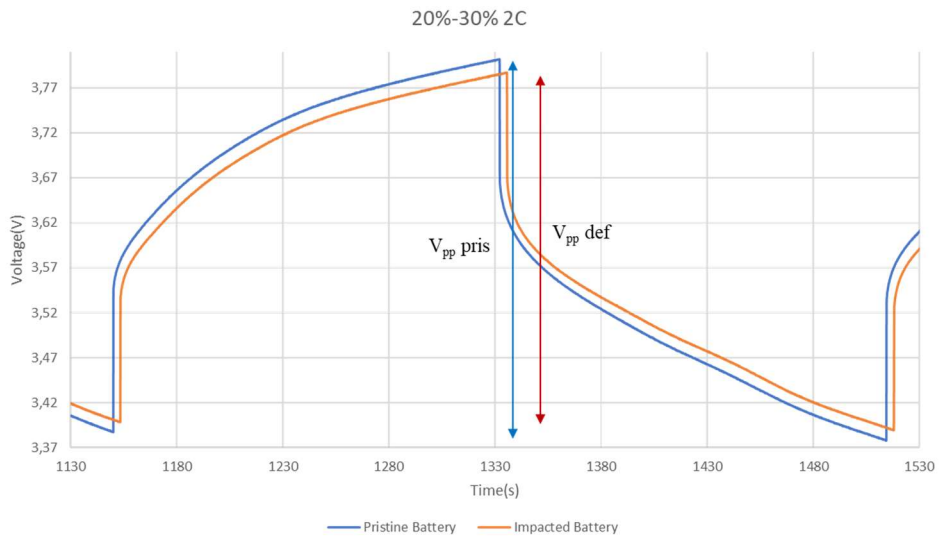


*Figure 4.2 - Detail of 2C cycling 20-30% for  $V_{pp}$  evaluation*

As expected measurement data for 2 and 3 C-rate confirmed the obtained result, with a double variation of voltage for the first case and a triple variation for the second one. An overview of the results is showed in Figures (4.2-4.3).

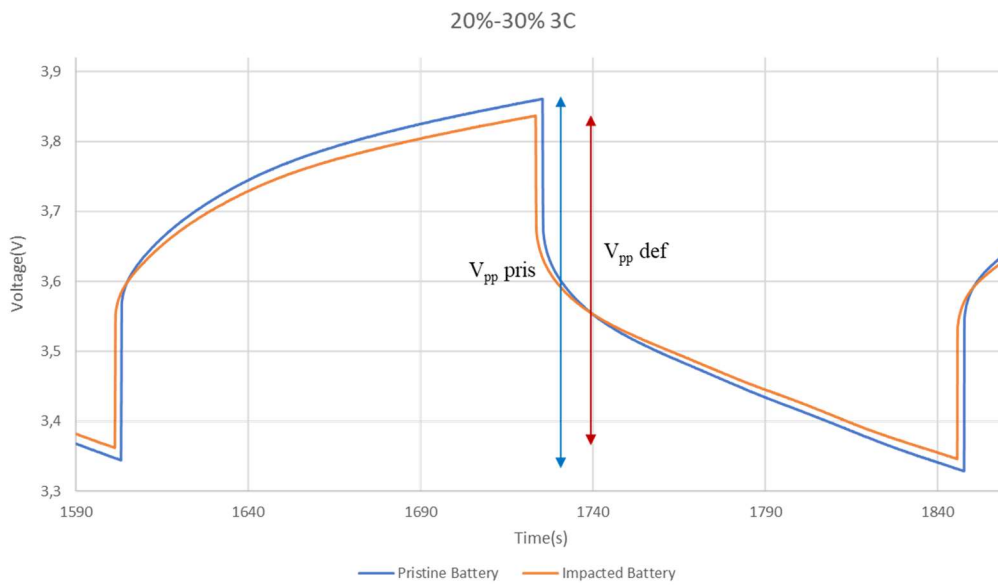


*Figure 4.3 - Detail of 3C cycling 20-30% for  $V_{pp}$  evaluation*

The coherence in the results among different loading condition strongly confirms the variation of resistance, and grants a reliable precision in the determination of the effort of the variation itself.

Voltage results can be summed up in the following table:

C-rate	Charge/discharge time[s]	$\Delta V_{pp}$ [V]	$\Delta V_p$ [V]
1C – 40A	360	0.02	0.01
2C – 80A	180	0.04	0.02
3C – 120A	120	0.06	0.03

*Table 7 - Experimental data voltage variation*

## 4.2 Simulation of electrical cycling

The target of simulation is to reproduce electrical cycling curves establishing a direct correlation between an internal resistance variation and peak to peak voltage ranges reduction. As a first step, simulations were conducted in order to reproduce the electrical behavior of the cell in pristine conditions, so, with no modifications acted on parameters that tune the internal resistance in the model. The following chart (Figure (4.4)) sums up the steps that will be explained in the next sections, in order to achieve a simulation in which a local variation of internal resistance is implemented.

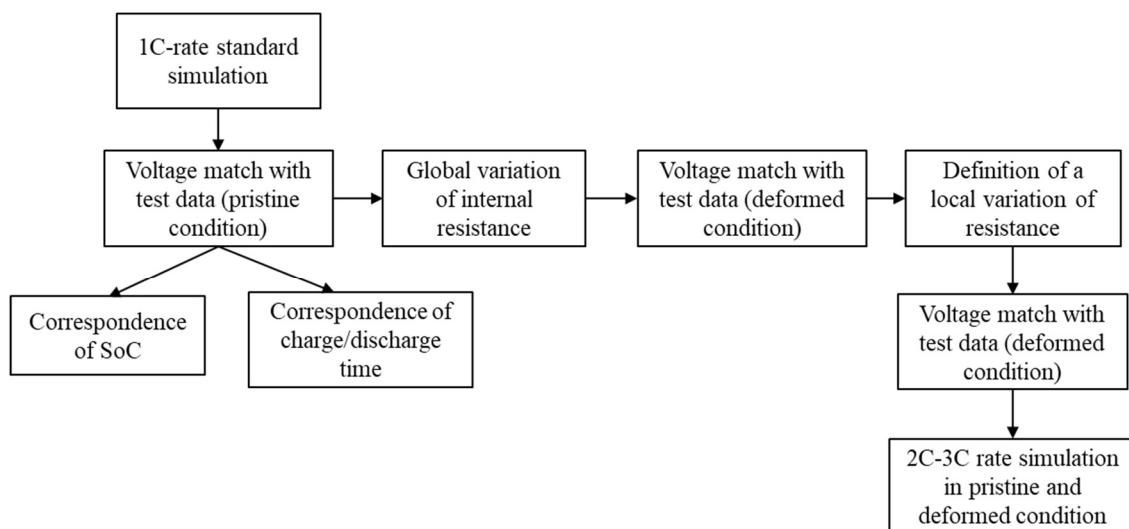


*Figure 4.4 - Electrical cycling simulation strategy*

### 4.2.1 1C rate simulation matching experimental data

The necessary conditions to reproduce experimental investigation curves are essentially related to the criterion employed to define the time ranges of charge/discharge during cycling. During tests, the quantity of charge that enters/exits the cell is ruled by a controller that calculates exactly the amount of Coulombs involved in the process. In simulation, a time-controlled criterion is used to set the time ranges for any phase. As an example, if in simulation the cell discharges from 100% SoC to 0% SoC at 1C rate, in 3600 seconds, the time required to charge/discharge 10% SoC is assumed to be 360s.

Basing on this assumption, it is possible to define a field function in StarCCM+ in order to control the values of applied current at cathode/anode tabs with time dependence.

For a better observability of the results, a portion of the result curve is showed in Figure (4.5), and compared with the real experimental curve. The range of time spaces a charge and discharge process: 20→30→20% SoC.

The simulated curve respects almost perfectly the real one in terms of voltage peak values, with a tolerance of about 0.01V for the highest and lowest values of the cycle.

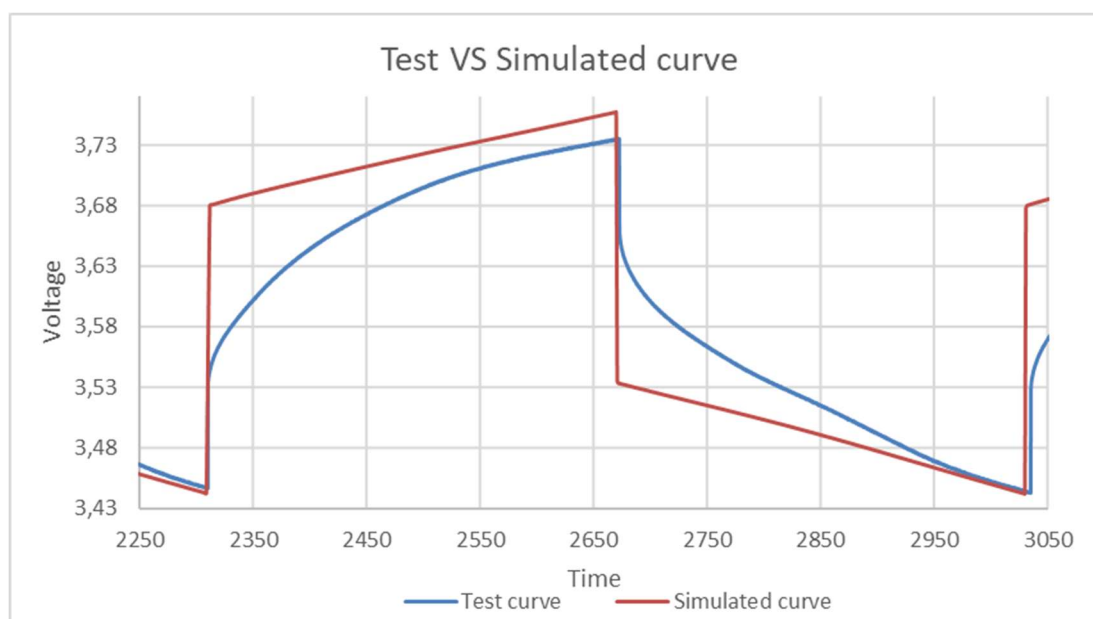


Figure 4.5 - Comparison between 1C pristine simulated and real measurement voltage curves

Regarding, instead, the SoC of the simulation, it can be observed that despite of ranging from 20% to 30%, the cycling spaces from 24% to 34%. This difference could be related to a difference between the rated capacity declared in the model and the real capacity of the

cell. This range of SoC will be considered a reference for all successive simulations. Once obtained an acceptable result in terms of matching between real and simulated voltage curve, the successive step requires to implement an internal resistance variation that has to determine a peak-to-peak voltage variation of 0.02V for this 1C-rate analysis.

#### 4.2.2 Global internal resistance variation

As a preliminary step before the implementation of a local resistance variation, a global variation of the parameter was implemented. This test is important for two main reasons: it provides an evidence of peak to peak voltage reduction during cycling, and validates the effort of resistance reduction, in terms of numeric value, obtained from the observation of the real experimental curves.

The modification is applied introducing an offset value in the internal resistance curve that lowers the values of exactly 0.25mΩ.

For a better understanding of this modification, in Figure (4.6) the comparison between the nominal curve and the curve with the applied offset value is shown.

Curves were extracted from the 1C- rate simulation conducted with and without the modification, in particular, the graph is focused on the 20-30% SoC cycling phase. Referring to the time axis, the phases can be identified as:

- Time: 4410-4770: charging 20→30%, resistance decreases
- Time: 4770-5130: discharging 30→20%, resistance increases
- Time: 5130-5490: charging 20→30%, resistance decreases
- Time: 5490-5850: discharging 30→20%, resistance increases

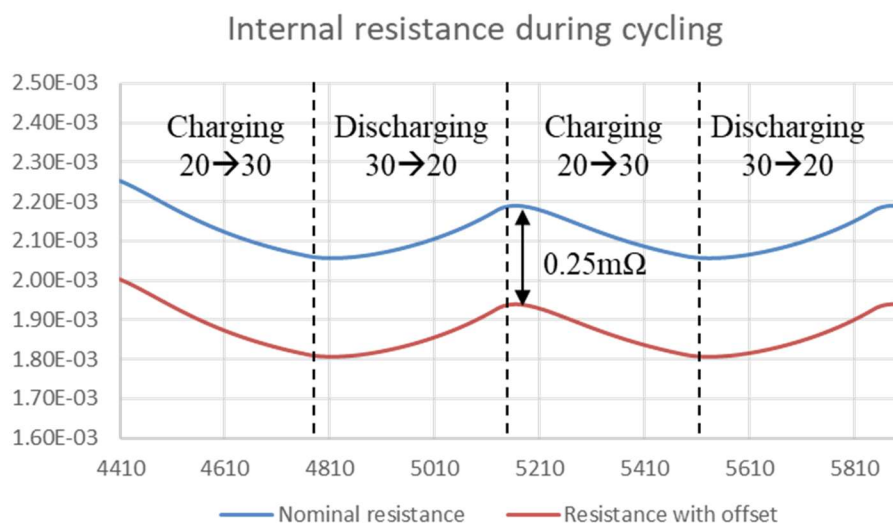
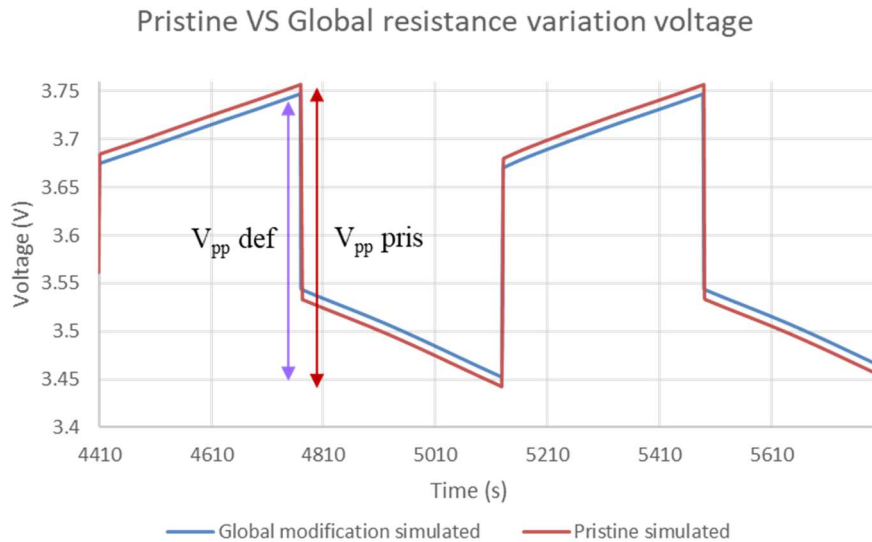


Figure 4.6 - Internal resistance curve with offset application during cycling

The comparison between the voltage curves obtained as a result of the offset application are showed in Figure (4.7).



*Figure 4.7 - Comparison between IC simulated cycling in pristine and global resistance modification condition*

Measuring the difference between the two peak to peak voltages values, the result is 0.02V, corresponding to the variation measured in the experimental curves and reported in Table (7). The achievement of a coherent voltage difference between the two simulated curves, makes possible the passage to the next step: the translation of the global variation into a local one.

### **4.2.3 Local internal resistance variation**

In order to obtain a global resistance variation, reducing the effective resistance modification to a localized area, representing the portion of the cell interested by the deformation, it is necessary to describe how the elements constituting the FEM model interact each other.

As explained in section 3.6, the correspondence created between the equivalent circuit and the mesh domain makes possible to define a stack of layers, as a discretized representation of the circuit itself. Each stack of single elements of the mesh, is, so, a circuit connected in parallel with all other cells, because they share the same voltage value measured at the terminals of the circuit (Figure (4.8)).

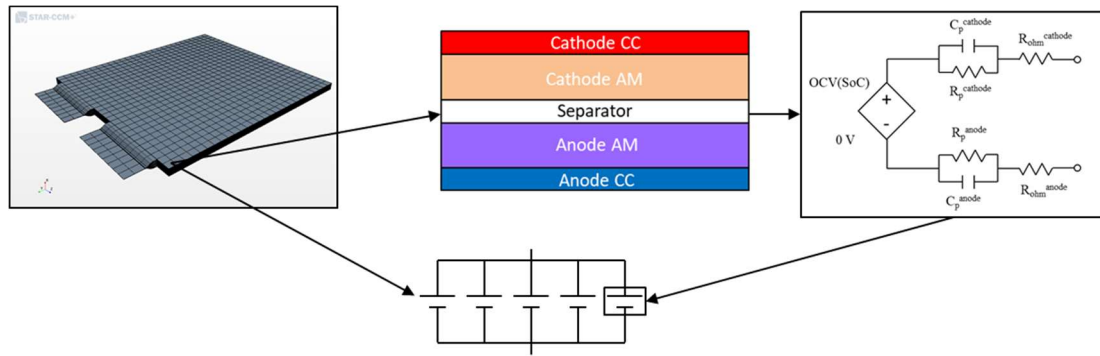


Figure 4.8 - Correspondence between single element and equivalent circuit

On the basis of this assumption, it is now possible to evaluate a portion of the domain as an equivalent circuit with properly scaled parameters.

The area interested by the deformation represents around 1% of the total cell surface. For this reason, the cell has been divided in two parts.

- Part 1: 99% of the cell surface with no resistance modification
- Part 2: 1% of the cell surface with resistance modification.

In StarCCM model, the identification of these two portions of the cell is carried out with the creation of a field function. The equation that rules the function is based on the positions of the nodes of the mesh, and, setting a proper radial distance from a designed center of the deformed area, it is possible to assign a numeric value for the function. In particular, in Figure (4.9) it can be observed how a unitary value was assigned to part 2 and a null value to part 1.

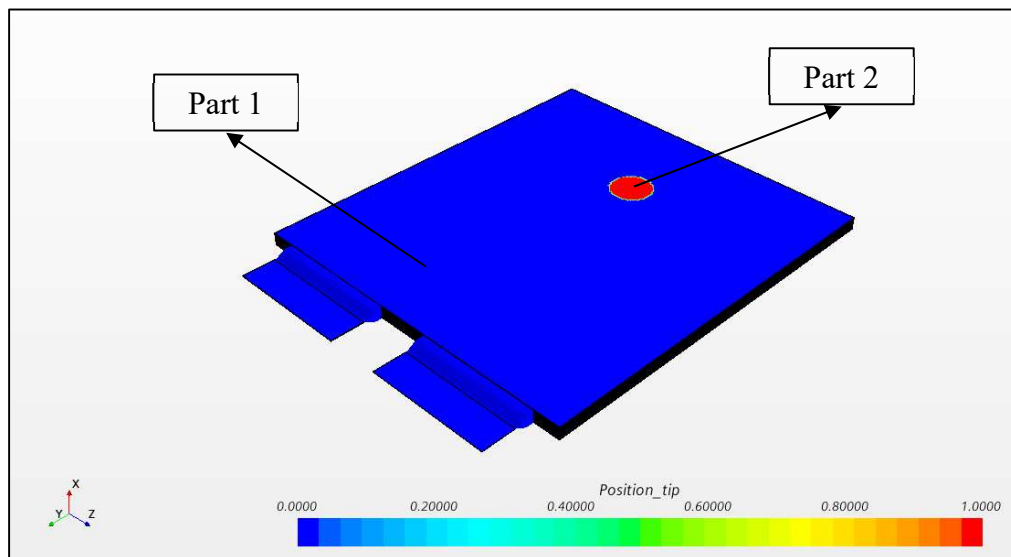


Figure 4.9 - Cell subdivision between deformed and pristine areas

Once defined the cell subdivision, it is necessary to calculate the new value of resistance to be assigned to part 2, in order to obtain a global resistance reduction of 0.25mΩ.

Considering this partition of the cell in 100 equal parts, the equivalent resistance, derived from the parallel of these single resistances must correspond to the global nominal resistance.

$$R_{nom} = \frac{R_{single}}{100} \quad (4.5)$$

Where  $R_{nom}$  is the equivalent global resistance of the cell and  $R_{single}$  is the resistance of the single portion of the cell.

Excluding the resistance related to part 2, the equivalent resistance for the 99% of the cell  $R_{99\%}$  results:

$$R_{99\%} = \frac{R_{single}}{100 - 1} = \frac{R_{nom} * 100}{99} \quad (4.6)$$

This value, must be related in parallel to the equivalent resistance of part 2:  $R_{1\%}$ , in order to obtain a new value of the global resistance  $R_{mod}$  that is simply the value of  $R_{nom}$  reduced of 0.25mΩ.

$$R_{mod} = R_{nom} - 0.25 = \frac{R_{99\%} * R_{1\%}}{R_{99\%} + R_{1\%}} \quad (4.7)$$

From this equation it is possible to derive the law for the definition of  $R_{1\%}$  that results as:

$$R_{1\%} = \frac{R_{mod} * R_{99\%}}{R_{99\%} - R_{mod}} = \frac{(R_{nom} - 0.25) * \frac{R_{nom} * 100}{99}}{\frac{R_{nom} * 100}{99} - (R_{nom} - 0.25)} \quad (4.8)$$

Obtaining this equation, explicitly dependant only on the value of  $R_{nom}$ , the value of the resistance in part 2 can be compared to the nominal resistance in order to obtain a scaling factor ( $R_{var}$ ), to be used in the real numerical implementation in the model.

$$R_{var} = \frac{R_{nom}}{R_{1\%}} = \frac{R_{nom} * (R_{99\%} - R_{mod})}{R_{mod} * R_{99\%}} \quad (4.9)$$

This law for the resistance variation allows to reproduce coherently the offset resistance reduction depicted in section 4.2.2. The model implementation of this result is achieved acting a local modification of the electrical conductivity  $\sigma$  of the active materials.

Reminding Equation (3.16), the new form of the expression for the deformed area results:

$$\sigma_{AM} = \frac{\text{layer thickness} * R_{var}}{R_{nom} \cdot \text{layer surface}} = \frac{(1.59E - 3) * R_{var}}{R_{nom}} \quad (4.10)$$

Exploiting the previously showed positional identification field function, the modification of the electrical conductivity is implemented only in the supposed area of deformation obtaining the result showed in Figure (4.10).

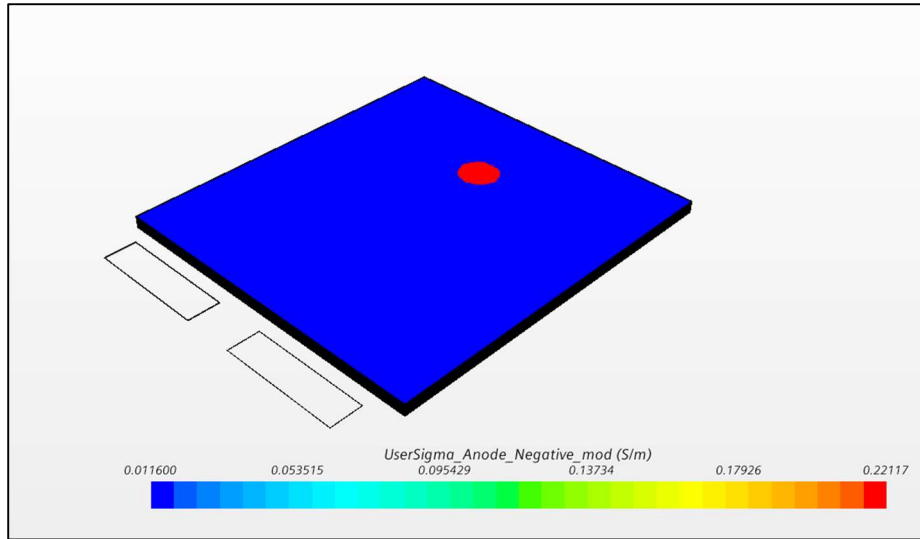


Figure 4.10 - Electrical conductivity local definition scene

The parameter  $R_{var}$  is strictly dependant on the value of internal resistance  $R_{nom}$ . In the following graph in Figure (4.11), the behavior in time of this function is showed, highlighting how, during charging phase the multiplicative factor has to increase, due to the internal resistance value decrease, while during discharging the factor is lowerd due to the resistance value increase.

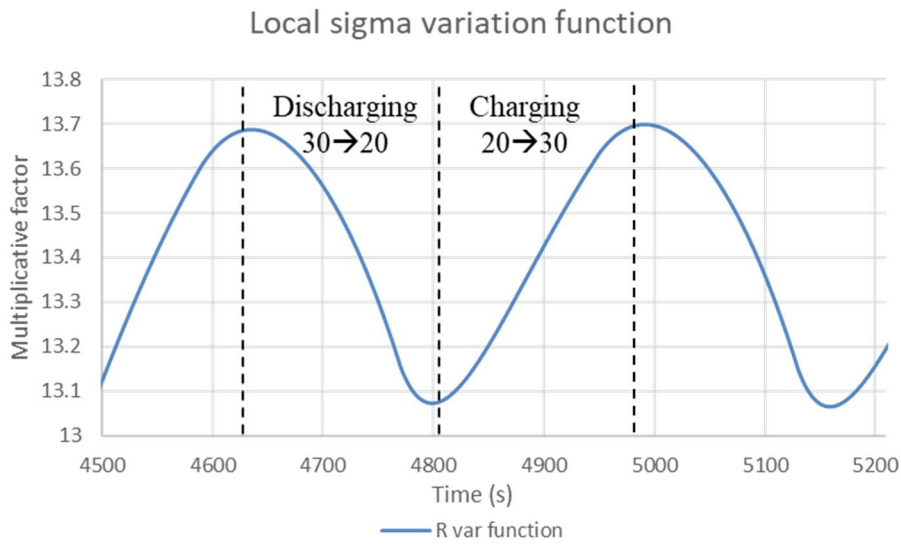


Figure 4.11 - Electrical conductivity function plot during cycling

This function grants the effective application of an offset contribution of  $0.25\text{m}\Omega$  to the internal resistance of the cell for any range of SoC. Practically, the electrical conductivity is incremented of a factor that ranges between 13.1 and 13.7, with a correspondent local reduction of the same efforts. In order to validate the correctness of the developed function, a simulation was conducted setting the just defined local modification of  $\sigma$ . Results are showed in Figure (4.12), where a comparison between the simulated pristine voltage cycling curve is compared to the simulated curve with the local modification, both for a loading condition of 1C-rate.

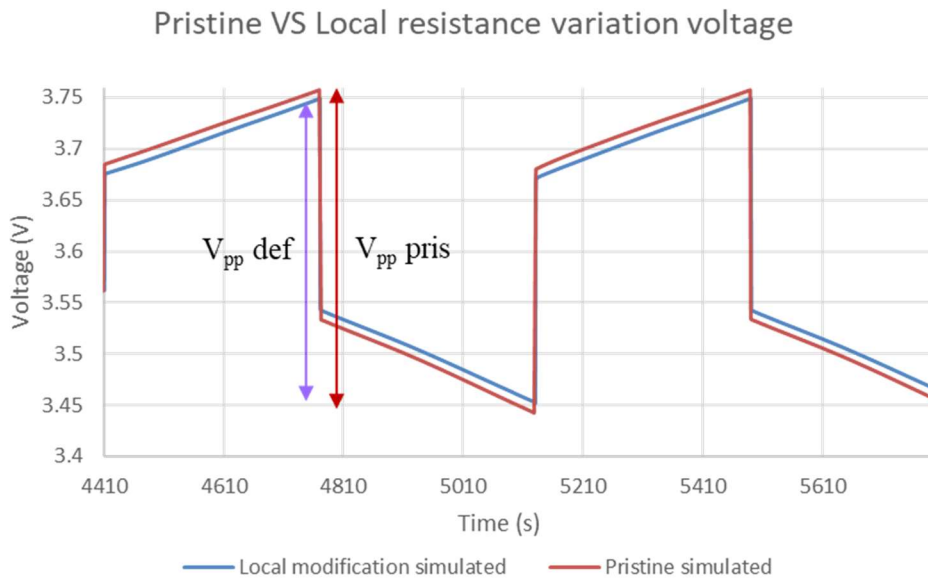


Figure 4.12 - Comparison between 1C simulated cycling in pristine and local resistance modification condition

Measuring the difference between  $V_{pp}$  pris and  $V_{pp}$  def, the resulting  $\Delta V$  is 0.02V, matching both, the results coming from the global resistance modification and the measured value from tests.

#### 4.2.4 Simulation results for different C-rates

Once obtained a coherent result for the simulations performed at 1C-rate, it was possible to evaluate the voltage behavior of the modelled cell at higher C-rates. Reminding Table (7) higher differences in terms of voltage are expected rising the value of applied current.

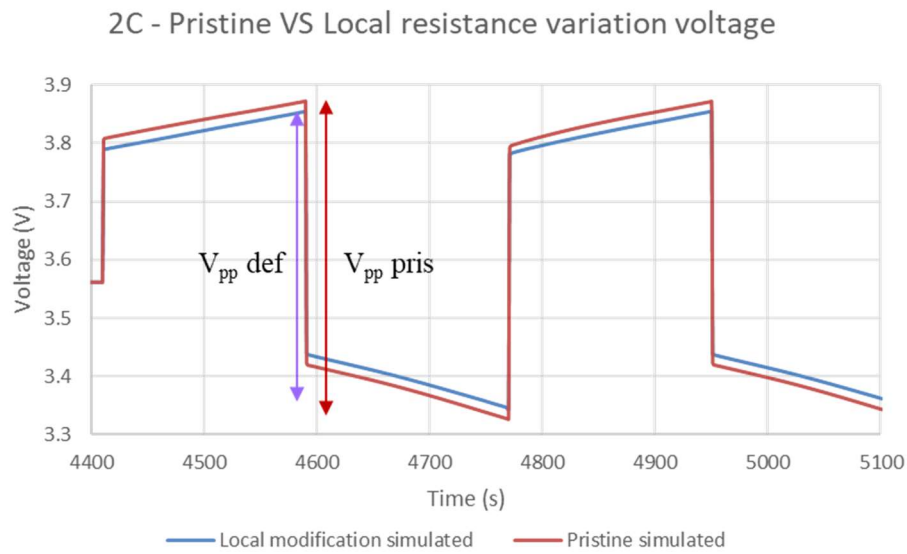


Figure 4.13 - Comparison between 2C simulated cycling in pristine and local resistance modification condition

For simulations conducted with a loading condition of 2C, the  $V_{pp}$  variation resulted 0.04V, coherently with test results (Figure (4.13)). As well as for a loading condition of 3C, the  $V_{pp}$  variation results proportional to the applied current with a reduction of 0.06V (Figure (4.14)).

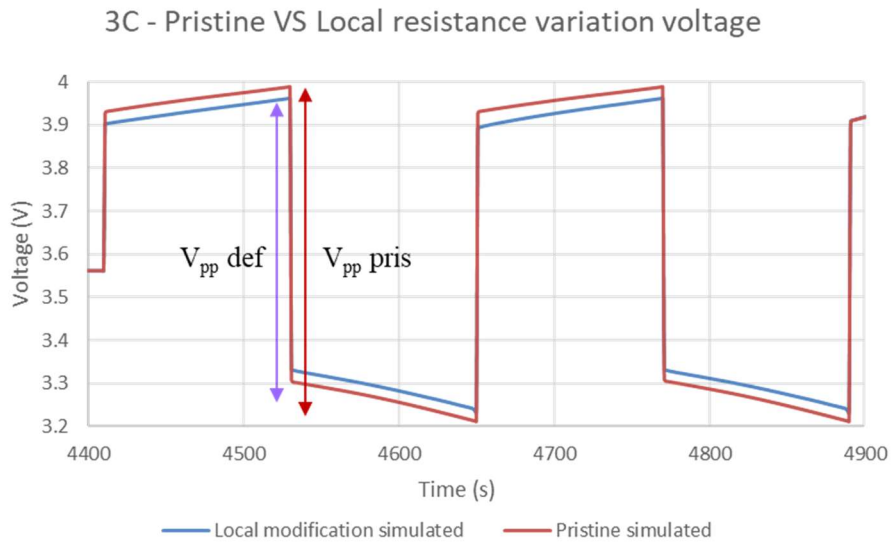


Figure 4.14 - Comparison between 3C simulated cycling in pristine and local resistance modification condition

#### 4.2.5 Effects of local resistance variation

ECD - Reducing the effort of internal resistance in part 2 as described in section 4.2.3 an electric current density distribution variation is induced in the cell.

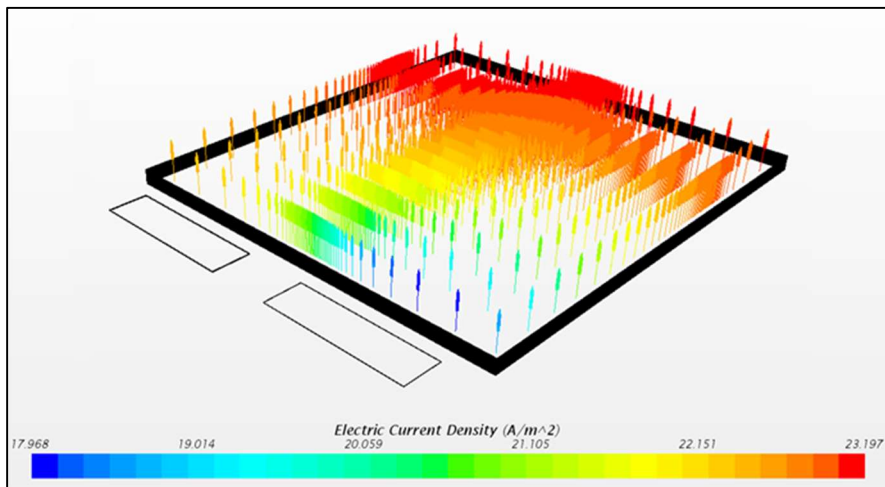


Figure 4.15 - ECD distribution for pristine condition simulation

In Figure (4.15) the ECD distribution for a simulation conducted at 1C-rate depicting the pristine condition is showed. The overall distribution of current appears uniform, as expected, while, in Figure (4.16) the introduced resistance reduction to reproduce the effects of deformation, determines a local ECD increase.

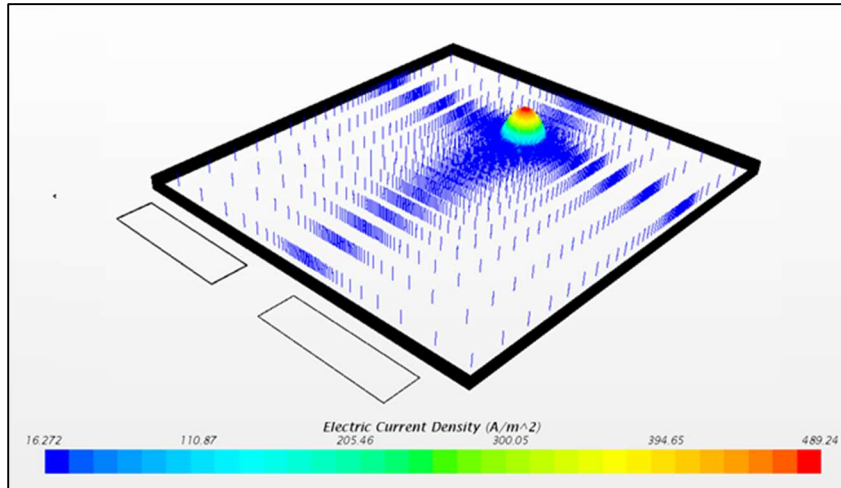


Figure 4.16 - ECD distribution for impacted condition simulation

Considering two simulations, conducted with same loading conditions with and without the impedance modification, it is possible to evaluate the surface integral of electric current density at the interfacing surfaces between separator and electrode layers. This measure provides a value that must be equivalent to the load current employed for the charge/discharge phase.

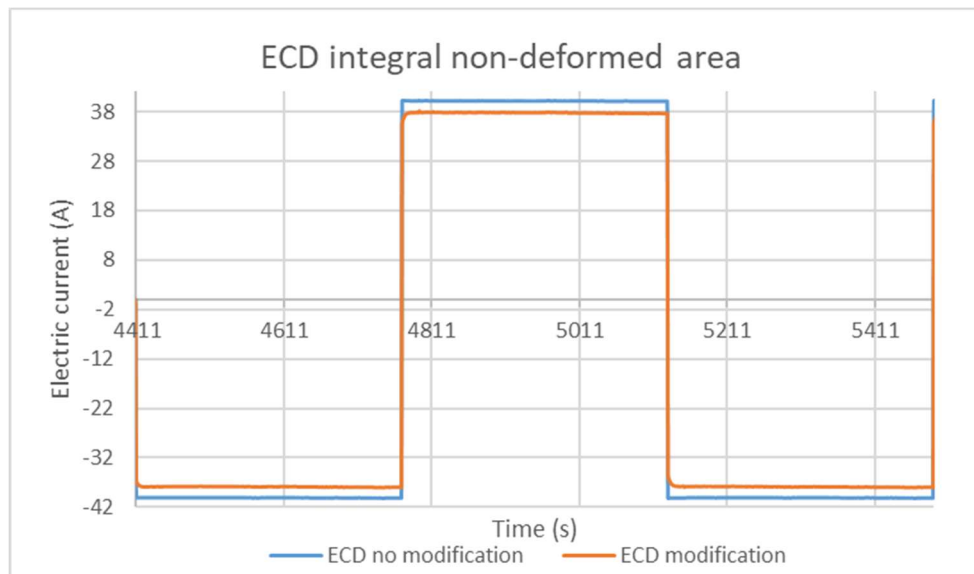


Figure 4.17 - ECD integral comparison non-deformed area (1C-rate)

In particular, graph in Figure (4.17) was obtained through a proper monitor tool used to measure the integral of ECD only in part 1, so, in the 99% of the cell constituting the area excluded by the resistance modification. The output value of the integration is of course an electric current value, measured in Ampere, and, as observable, in both cases close to the value of loading current of 1C-rate (40A). The alternance between positive and negative

values of current is caused by the electrical cycling process going on during simulation. Focusing on the amplitude of the curves in both conditions, it is possible to observe how, in the simulation with local resistance reduction, the integral value results lowered, with respect to the unmodified case. The effort of this reduction can be quantified as 5,8% of ECD integral. Physically, this result means that the local resistance reduction induces a strong increase of current in the “deformation area” (part 2), that must be compensated by a reduction of about 6% in the rest of the cell (part 1).

**SoC** – The just described ECD distribution has a direct influence on SoC variation over the cell. Reminding Equation (3.14), SoC is defined at each time instant on the basis of the local ECD value. In particular, the higher the value of ECD, the higher the SoC variation in time. Practically, this means that, in part 2, where resistance is reduced, and consequently, ECD increased, SoC variation is faster than variation in part 1.

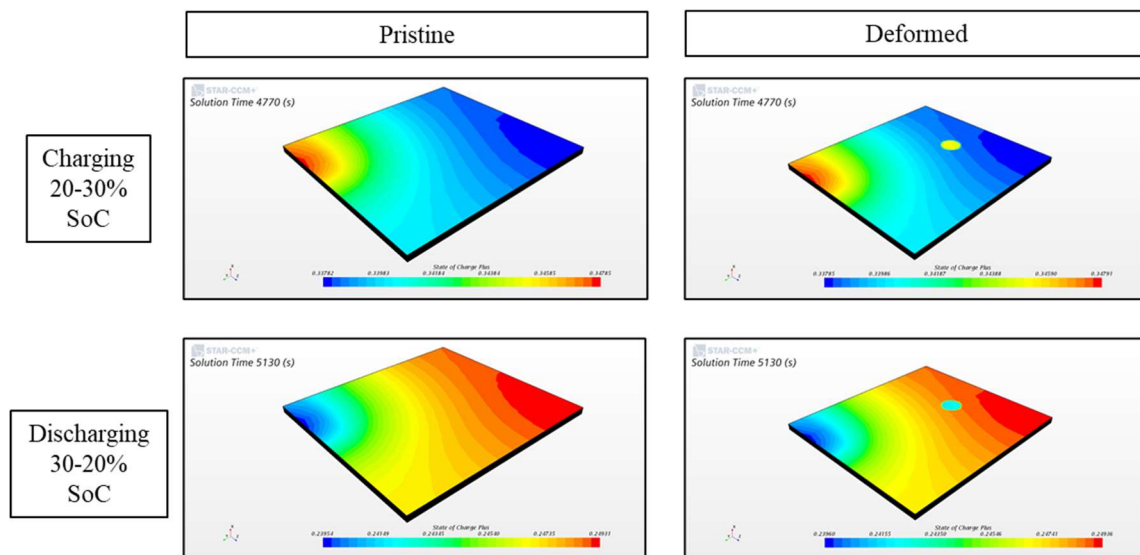


Figure 4.18 - SoC scene during electrical cycling (IC)

Figure (4.18) shows SoC distribution during electrical cycling simulation between 20-30% SoC. At simulation time 4770s, charging phase is concluded, and, as observable, in the deformation area, SoC results higher compared with result coming from pristine case simulation. In a similar way, at simulation time 5130s, when discharging phase is concluded, local SoC measured in deformed case simulation is lower than the pristine case. In both cases, state of charge value measured in part 2 does not result the peak value for the cell at a define time instant.

The local resistance modification induced a “faster” SoC dynamics, in the area interested

by deformation. Although no evidence of this behavior could be obtained from experimental investigation, the obtained result is coherent with the law ruling SoC definition in the cell.

### 4.3 Temperature results

Although no significant differences in terms of temperature were observed during tests comparing pristine and deformed cells, this measurement was also conducted during simulations. The following figure, shows a temperature comparison for the same time instants for both simulations just mentioned in the previous section (1C-rate).

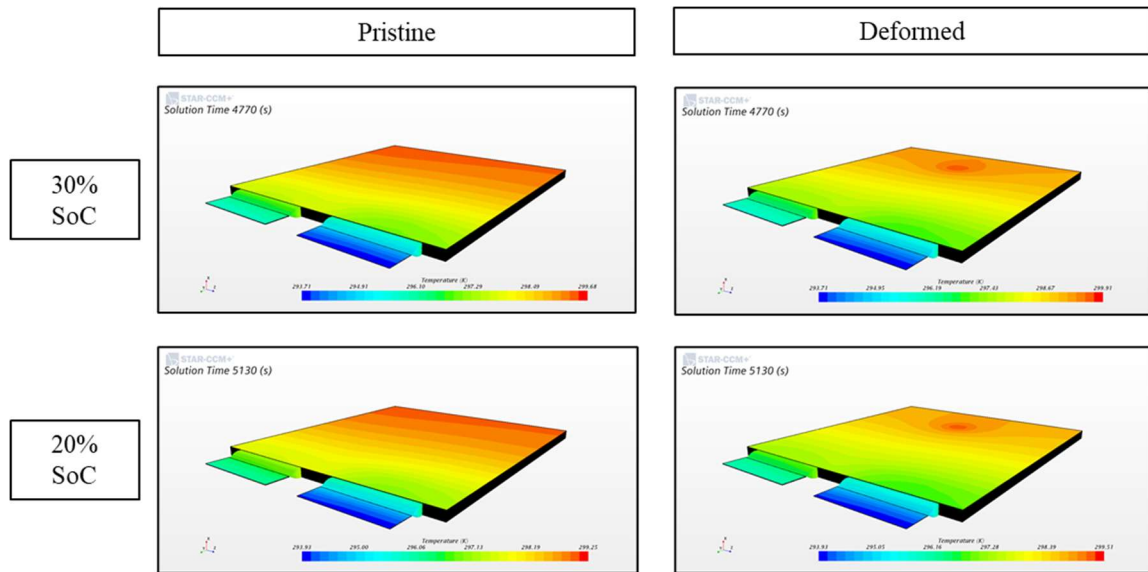


Figure 4.19 - Temperature scene during electrical cycling (1C)

The reported scenes (Figure (4.19)) show temperature evolution during cycling between 20 and 30% Soc. Data from simulation with the implementation of local resistance reduction show a small local temperature increase in the proximity of the area interested by the modification. This difference results really small, in the order of 1°, with maximum and minimum temperature of the cell remaining essentially unchanged between the two simulations. A temperature comparison was not conducted between real measurement and simulation data, because of the unmodelled heat dissipation through the sheets of insulating material and metal plates constituting the test set. Anyway a coherence in the results was found comparing two simulated conditions.

# ***CHAPTER 5***

## ***5. Conclusions***

In this work of thesis, a strategy for the evaluation, in simulation, of the effects of a non-disruptive mechanical load on a pouch cell has been developed.

As a first step, a literature research was conducted in order to understand the physiochemical effects of a compressive-like load on pouch cell; the research revealed a great quantity of conducted studies observing the effects of a global compression of the cell between constraining elements, but really few researches were found about the evaluation of the effect of a local non-severe mechanical load application. Moreover, main part of these studies focused on the understanding of the structural effects of inducted deformations/ruptures, not considering the effect of an electrical load on the damaged cells. A common aspect, strongly underlined by different studies, consisted in the observation of the separator layer modifications inducted by compressive loads. Considering the pouch cell composition, this layer represents surely the most suitable strain allocator during mechanical loading. The porous nature of the PE/PP sheet allows a strong thickness reduction at the cost of a pore closure phenomenon. This inducted effect could strongly affect the charge transfer dynamics in the deformed area, determining a major resistance to charge movement across the layer itself. For this reason, some researches associate compressive loads to a overall increase of the internal impedance of the cell.

The conducted experimental investigation aimed to identify electro-thermal effects of the application of an impacting element on the cell, comparing voltage and temperature results coming from the same tests conducted on the pristine and deformed cells.

While on the thermal point of view, no significant variations were observed, the comparison between charging/discharging curves obtained from the 20-30% SoC electrical cycling revealed an internal resistance reduction of 0.25m $\Omega$  in the impacted cell. This result was strongly validated by the C-rate independence of the result and the repeatability of the obtained voltage values on three different cells.

On these basis, the modelling and simulation strategy was developed, with the target of the achievement of comparable results with respect to the experimental investigation.

A 1D equivalent circuit model was developed and employed to obtain a preliminary simulation of charging/discharging curves during electrical cycling and compare results

with test data; the equivalent circuit model, was then extended to a 3D FEM model realized in STARCCM+ simulation environment. In this phase, the test output results in terms of internal impedance variations were used as an input for the FEM model to reproduce the effect of the application of an impactor modifying locally the cell impedance. The equivalent “concentrated” resistance reduction for the deformed area resulted to be 1/13 times the resistance value in the remaining part of the cell. This assumption determines a strong local variables imbalance in simulation, in particular in terms of ECD distribution. Trying to associate this quantity to the charge transfer taking place in the cell, the deformation area would represent a higher charge density area, a concept that apparently contrasts the evaluations reported in literature. An hypothesis that could justify the resistance reduction, despite of an expected increase, could be a severe reduction of the distance between the electrodes combined with other effects that facilitate the charge transfer, like the improved permeation of the electrolyte in the electrode (wettability), able to overcome the effect of pore closure phenomenon, leading to a global effect of resistance reduction.

These conclusions are based on the assumption of a concentrated resistance reduction in the deformation area, but, another possible interpretation of the obtained resistance variation result could be associated to an unwanted stress condition induced on the cell during tests. In particular, the application of a localized impacting element could have determined a decompression of the area not interested by the deformation, causing an overall effect on the cell, exactly opposite to the previously analyzed one.

Clarifications about the internal modification of the cell structure could be obtained performing a dissection of the impacted cell, in proximity to the application point of the impactor, in order to understand the effective layer thickness reduction.

Further investigation could also be conducted exploring different mechanical loading conditions, varying for example, the displacement of the impactor inside the cell in order to understand in a clearer way the dependance of the resistance reduction on the created deformation.

## 6. References

- [1] Mehmet Efe Biresselioglu, Melike Demirbag, Kaplan Barbara, Katharina Yilmaz, “Electric mobility in Europe: A comprehensive review of motivators and barriers in decision making processes”, *Science Direct*, 2018.
- [2] Jaume Duch Guillot, “Emissioni di CO2 delle auto: i numeri e i dati. Infografica”, *European Parliament*, 2019.
- [3] Bruno Scrosati, Jürgen Garche, Werner Tillmetz, “Advances in Battery Technologies for Electric Vehicles”, 2015.
- [4] Venkatasailanathan Ramadesigan, Paul W. C. Northrop, Sumitava De, Shriram Santhanagopalan, Richard D. Braatz, Venkat R. Subramanian, “Modeling and Simulation of Lithium-Ion Batteries from a Systems Engineering Perspective” *Journal of The Electrochemical Society*, 2011.
- [5] G. L. Plett, *Battery Management Systems*, Norwood: Artech House, 2015.
- [6] Ashok K. Singal, “The Internal Resistance of a Battery - A Physical Perspective”, *Cornell University*, 2013.
- [7] W. Luo, C. Lv, L. Wang and C. Liu, “Study on Impedance Model of Li-ion Battery,” in 6th IEEE Conference on Industrial Electronics and Applications, 2011
- [8] B. V.S., *Fundamentals of Electrochemistry*, Inc., Hoboken, New Jersey: John Wiley & Sons, 2006.
- [9] Christina Peabody, Craig B. Arnold, “The role of mechanically induced separator creep in lithium-ion battery capacity fade”, *Journal of Power Sources*, 2011.
- [10] Anup Baraia, Ravichandra Tangirala, Kotub Uddina, Julie Chevalier, Yue Guo, Andrew McGordona, Paul Jennings, “The effect of external compressive loads on the cycle lifetime of lithium-ion pouch cells”, *Journal of energy storage*, 2017.
- [11] Petr Vyroubal, Tomáš Kazda, “Equivalent circuit model parameters extraction for lithium ion batteries using electrochemical impedance spectroscopy”, *Journal of Energy Storage*, 2017.
- [12] John Cannarella, Craig B. Arnold “Ion transport restriction in mechanically strained separator membranes” *Journal of Power Sources*, 2012.
- [13] Xiaowei Zhang, Elham Sahraei, & Kai Wang, “Li-ion Battery Separators, Mechanical Integrity and Failure Mechanisms Leading to Soft and Hard Internal Shorts”, *Scientific reports*, 2016.

- [14] Ali Jokar, Barzin Rajabloo, Martin Desilets, Marcel Lacroix “Review of simplified Pseudo-two-Dimensional models of lithium-ion batteries”, *Journal of Power Sources*, 2016.
- [15] Xiaoqiang Zhang, Weiping Zhang, Geyang Lei, “A Review of Li-ion Battery Equivalent Circuit Models”, *Transactions on electrical and electronic materials*, 2016.
- [16] Zhenpo wang, Jun ma, Lei Zhang, “Finite Element Thermal Model and Simulation for a Cylindrical Li-Ion Battery”, *IEEE Access - special section on battery energy storage and management systems*, 2017.
- [17] Chao Zhang, Shriram Santhanagopalan, Michael A. Sprague, Ahmad A. Pesaran, “Coupled mechanical-electrical-thermal modelling for short-circuit prediction in a lithium-ion cell under mechanical abuse”, *Journal of Power Sources*, 2015.
- [19] Ruifeng Zhang, Bizhong Xia, Baohua Li, Libo Cao, Yongzhi Lai, Weiwei Zheng, Huawen Wang, Wei Wang, Mingwang Wang, “A Study on the Open Circuit Voltage and State of Charge Characterization of High Capacity Lithium-Ion Battery Under Different Temperature”, *Energies*, 2018.
- [19] G. Kovachev, H. Schrottner, G. Gstrein, L. Aiello, I. Hanzu, H. M. R. Wilkening, A. Foitzik, M. Wellm, W. Sinz and C. Ellersdorfer, “Analytical Dissection of an Automotive Li-Ion Pouch Cell”, *Batteries*, 2019.
- [20] Siemens STAR-CCM+, “User Guide”.